SKI Report 2004:57

Research

Research and Development Program in Reactor Diagnostics and Monitoring with Neutron Noise Methods

Stage 10. Final Report

C. Demazière
I. Pázsit
C. Sunde
J. Wright

December 2004

ISSN 1104–1374
ISRN SKI-R-04/57-SE

SKI

SKI Perspective

Background

This report constitutes Stage 10 of a long-term research and development program concerning the development of diagnostics and monitoring methods for nuclear reactors.

Such a program consists of two main parts. First, the space- and frequency dependent neutron noise, induced by a specific perturbation (anomaly) is calculated, via an integral over the transfer function of the system and the noise source, i.e. the perturbation. The latter consists of the fluctuations of the macroscopic cross sections that correspond to the perturbation. Each perturbation needs to be represented through a suitable model. The transfer function is calculated from the dynamical transport equations. Finally, one has to invert the above mentioned integral (unfolding) in order to achieve the purpose of the diagnostics, i.e. to determine the parameters of the perturbation from the measured neutron noise and the known transfer function.

Results up to Stage 9 were reported in SKI reports, see the list below. The results have also been published in international journals and have been included in both licentiate- and doctor's degrees.

Purpose

The purpose of the research program is to contribute to the strategical research goal of competence and research capacity by building up competence within the Department of Reactor Physics at Chalmers University of Technology regarding reactor physics, reactor dynamics and noise diagnostics. The purpose is also to contribute to the research goal of giving a basis for SKI's supervision by developing methods for identification and localization of perturbations in reactor cores.

Results

The program executed in Stage 10 consists of three parts. The first part deals with identification and localization of absorbers of variable strength in nuclear reactors. The second part deals with development of the Feynman-alpha method for pulsed sources. The third part deals with the classification of two-phase flow regimes via image analysis and a neuro-wavelet approach.

Project information

Responsible at SKI has been Ninos Garis.
SKI reference: 14.5-030917-200305001.
Previous SKI reports: 95:14 (1995), 96:50 (1996), 97:31 (1997), 98:25 (1998), 99:33 (1999), 00:28 (2000), 01:27 (2001), 2003:08 (2003), 2003:30 (2003).

SKI Report 2004:57

Research

Research and Development Program in Reactor Diagnostics and Monitoring with Neutron Noise Methods

Stage 10. Final Report

C. Demazière
I. Pázsit
C. Sunde
J. Wright

Department of Reactor Physics
Chalmers University of Technology
SE-412 96 Göteborg
Sweden

December 2004

Research and Development Program in Reactor Diagnostics and Monitoring with Neutron Noise Methods: Stage 10

This report gives an account of the work performed by the Department of Reactor Physics, Chalmers University of Technology, in the frame of a research contract with the Swedish Nuclear Power Inspectorate (SKI), contract No. 14.5-030917-200305001. The present report is based on work performed by Christophe Demazière, Carl Sunde, Johanna Wright and Imre Pázsit, with the latter being the project leader.

This report constitutes Stage 10 of a long-term research and development program concerning the development of diagnostics and monitoring methods for nuclear reactors. The long-term goals are elaborated in more detail in e.g. the Final Reports of stage 1 and 2 (SKI Report 95:14 and 96:50, Refs. [1] and [2]). Results up to stage 9 were reported in [1] - [9]. A brief proposal for the continuation of this program in Stage 11 is also given at the end of the report.

The program executed in Stage 10 consists of three parts and the work performed in each part is summarized below.

Identification and localization of absorbers of variable strength in nuclear reactors

A so-called 2-D 2-group neutron noise simulator was previously developed at the Department of Reactor Physics. This simulator is able to calculate the space-dependence of the neutron noise induced by localised or spatially-distributed absorbers of variable strength or by vibrating absorbers. These calculations are performed in the 2-group diffusion approximation and can treat an arbitrary heterogeneous 2-D system. The goal of the present investigation is to use the simulator for unfolding purposes, i.e. to reconstruct the noise source from the detector readings. This task is particularly challenging since the number of detectors available in a commercial PWR can be very low. In this study, five detectors are assumed to be present and evenly distributed in the core. Furthermore, only localised absorbers of variable strength are considered as perturbations.

Numerical simulations were first carried out to verify that the space-dependent local and global components of the neutron noise were overwhelmingly large compared to the point-kinetic term of the neutron noise whose spatial structure does not depend on the position of the perturbation. The significance of the space-dependent global component is that its relaxation length is large enough, so that several neutron detectors can monitor it. Therefore, the neutron noise induced at the position of the detectors is itself a function of the position of the perturbation. Unfolding procedures could thus be considered.

Prior to performing any unfolding, the type of the noise source has to be determined, since the algorithms developed in this report are based on the assumption of an absorber of variable strength. Such a noise source can also be used to model a local thermohydraulic instability. Identification of the type of the noise source is based on the in-phase behaviour of the neutron noise for an absorber of variable strength (as opposed to an out-of-phase behaviour for a vibrating absorber). Several unfolding techniques were then investigated. It was demonstrated that the exact position of the noise source could be determined for some of these techniques.

Development of the Feynman-alpha method for pulsed sources

The purpose of this section is to give a detailed description of the calculation of the Feynman-alpha formula with deterministically pulsed sources. In contrast to previous calculations [35], Laplace transform and complex function methods are used to arrive at a compact solution in form of a Fourier series-like expansion. The advantage of this method is that it is capable to treat various pulse shapes. In particular, in addition to square- and Dirac-delta pulses, a more realistic Gauss-shaped pulse is also considered here. The final solution of the modified variance-to-mean, that is the Feynman $Y(t)$-function, can be quantitatively evaluated fast and with little computational effort.

The analytical solutions obtained are then analysed quantitatively. The behaviour of the number of neutrons in the system is investigated in detail, together with the transient that follows the switching on of the source. An analysis of the behaviour of the Feynman $Y(t)$-function was made with respect to the pulse width and repetition frequency. Lastly, the possibility of using the formulae for the extraction of the parameter alpha from a simulated measurement is also investigated.

Classification of two-phase flow regimes via image analysis and a neuro-wavelet approach

Algorithmic methods for non-intrusive identification of two-phase flow have been searched for during a long time. One relatively new, not yet fully explored possibility is to use images of the flow, and use intelligent image processing of the data for identification of the flow regime. Such an attempt is reported in this report. Classification of the flow regime types is performed by an artificial neural network (ANN) algorithm. The input data to the ANN are some statistical functions (mean and variance) of the wavelet transform coefficients of the pixel intensity data. The training is achieved by using a number of frames for the basic flow regimes. The trained network is then tested on other frames, corresponding to the different flow regimes.

The images originally considered were obtained from dynamic neutron radiography recordings, obtained from the Kyoto University Research Reactor Institute. These were made on a real two-phase flow of water and steam in a heated aluminium pipe. Although these measurements contain all four basic flow regimes in a real setting (pressure and temperature), the image quality turned out to be very poor, and only a very basic study could be performed for the flow regime identification. In order to obtain better quality images, experiments were set up with an air-water two component loop, using visible light and coloured water. In these experiments only bubbly and slug flow regimes could be created.

The investigations show that in the water-air loop, the flow regimes can be identified with a close to 100% efficiency. The advantage of the wavelet pre-processing was that the number of training cycles, in order to attain a certain classification error limit, was much smaller than in the case of using raw pixel input data without pre-processing.

Forskningsprogram angående härddiagnostik och härdövervakning med neutronbrusmetoder: Etapp 10

Denna rapport redovisar det arbete som utförts inom ramen för ett forskningskontrakt mellan Avdelningen för Reaktorfysik, Chalmers tekniska högskola, och Statens Kärnkraftinspektion (SKI), kontrakt Nr. 14.5-030917-200305001. Rapporten är baserad på arbetsinsatser av Christophe Demazière, Carl Sunde, Johanna Wright och Imre Pázsit, med sistnämnde som projektledare.

Rapporten omfattar etapp 10 i ett långsiktigt forsknings- och utvecklingsprogram angående utveckling av diagnostik och övervakningsmetoder för kärnkraftreaktorer. De långsiktiga målen med programmet har utarbetats i slutrapporterna för etapp 1 och 2 (SKI Rapport 95:14 och 96:50, Ref. [1] och [2]). Uppnådda resultat fram till etapp 9 har redovisats i referenserna [1] - [9]. Ett förslag till fortsättning av programmet i etapp 11 redovisas i slutet av rapporten.

Det utförda forskningsarbetet i etapp 10 består av tre olika delar och arbetet i varje del sammanfattas nedan.

Identifiering och lokalisering av absorbatorer med varierad styrka i reaktorer

Tidigare har det utvecklats en 2-D 2-grupps neutronbrussimulator hos Avdelningen för Reaktorfysik. Simulatorn kan beräkna det rumsberoende bruset från en punktkälla eller en rumsberoende källa. Källan kan vara en absorbator av varierad styrka eller en vibrerande absorbator. Beräkningarna utförs med 2-grupps diffusionsapproximation och ett godtyckligt 2-D heterogent system kan användas. Syftet med projektet är att kunna använda simulatorn för inversa beräkningar, som kan rekonstruera bruskällan med hjälp av detektorsignaler. Eftersom det bara finns ett fåtal detektorer i en kommersiell reaktor är det en ganska svår uppgift att rekonstruera bruskällan. I detta projekt antas att det bara finns fem detektorer jämt fördelade i härden. Dessutom används bara en absorbator av varierad styrka som bruskälla.

Först gjordes numeriska beräkningar för att verifiera att de lokala och globala rumsberoende komponenterna av bruset är betydligt större än den punktkinetiska termen. Rumsberoendet hos den punktkinetiska termen beror inte på läget hos störningen. Relaxationslängden hos den globala rumskomponenten av bruset måste vara tillräckligt stor för att den skall kunna mätas av flera detektorer. Detta medför att bruset vid en detektor är beroende av läget hos störningen, vilket i sin tur medför att det går att använda inversa metoder för att lösa problemet.

Det första som måste göras är att bestämma vilken typ av bruskälla som finns i systemet eftersom algoritmen som utecklats i denna rapport antar att det är en absorbator av varierad styrka. Det går även att modellera en lokal termohydraulisk instabilitet som en absorbator av varierad styrka. Identifieringen bygger på det faktum att bruset från en absorbator med varierad styrka är i fas jämfört med bruset från en vibrerande absorbator som är ur fas. Flera olika inversa metoder undersöktes. Den exakta positionen av bruskällan kunde bestämmas med några av dessa metoder.

Utveckling av en Feynman-alfa-metod för pulsade källor

Detta kapitel ger en detaljerad beskrivning av hur Feynman-alfa-formeln för deterministiskt pulsade källor beräknas. Till skillnad från tidigare beräkningar [35], används Laplacetransformer och komplexa funktioner för att få en kompakt lösning i form av Fourierserieliknande utvecklingar. Fördelen med detta är att det är enkelt att variera pulsformen. Framför allt går det att använda en mer realistisk Gauss-formad puls förutom fyrkants- och Dirac-deltapulser. Det går snabbt och enkelt att kvantitativt utvärdera slutresultatet av den modifierade "variance-to-mean" eller Feynman *Y(t)*-funktionen.

De analytiska lösningarna kan sedan analyseras kvantitativt. Antalet neutroner och transienten som följer efter att källan aktiverats kan studeras i detalj. En analys av Feynman *Y(t)*-funktionen med avseende på pulsbredd och repetitionsfrekvens har utförts. Till sist undersöktes möjligheten att använda formeln för att bestämma α från simulerade mätningar.

Identifiering av tvåfasflöden genom bildanalys med hjälp av neurala nätverk och wavelets

Under en längre tid har algoritmiska metoder för beröringsfri identifiering av tvåfasflöden eftersökts. En relativt ny metod, som ännu inte är helt undersökt, är att använda intelligent bildbehandling på flödesbilder. Detta kapitel beskriver ett försök att använda en sådan metod. Klassificeringen av flödetyperna utförs av ett artificiellt neuralt nätverk (ANN). Som indata till ANN används statistiska data, till exempel medelvärde och varians, av koefficienterna från en wavelettransform av punktintensiteten i bilderna. Nätverket tränas med ett antal bilder från de olika flödestyperna och därefter testas det med liknande bilder som inte användes under träningsprocessen.

De första bilderna som analyserades kommer från experiment inom dynamisk neutronradiografi utförda av Kyoto University Research Reactor Institute. Bilderna är tagna på riktigt tvåfasflöde av vatten och ånga i ett aluminiumrör. Även om bilderna innehåller alla fyra grundtyperna av flöde i en realistisk miljö (tryck och temperatur) var bildkvaliten för dålig för att göra annat än en enkelt bildanalys. För att få bättre bildkvalitet gjordes ett experiment med vanligt ljus, färgat vatten och luft istället. Dock gick det bara att skapa bubbel- och slugflöde.

Med de senare bilderna ger identifieringsalgoritmen en nästan 100-procentig korrekt klassificering av flödestyperna. Detta gäller dock både waveletbehandlad och orginalbilds-indata. Den stora fördelen med waveletbehandling av bilderna är den reducering av antalet träningscykler som behövs för att nätverket skall uppnå sitt klassificeringsmål. Antalet träningscykler är ungefär 100 gånger fler om orginalbildens data används som indata till nätverket jämfört med waveletbehandlad data.

Section 1

Identification and localization of absorbers of variable strength in nuclear reactors

1.1 Introduction

It is now well recognized that the analysis of the neutron noise, i.e. the difference between the time-dependent neutron flux and its time-averaged value, assuming that all the processes are stationary and ergodic in time, can be used for many diagnostic purposes in nuclear reactors. Many examples can be found in the literature [10]-[13]. Usually, one distinguishes two main categories within noise analysis: identification of anomalies, and estimation of dynamical core parameters while the reactor is at steady-state conditions. This Section will focus on one specific aspect of the former category, namely the identification and localization of absorbers of variable strength. This type of noise source is for instance typical of a channel instability or Density Wave Oscillation (DWO) in Boiling Water Reactors (BWRs) [14], [15]. Another possible type of noise source would be a so-called vibrating absorber, such as vibrating control rods in Pressurized Water Reactors (PWRs). Such noise sources are not considered in this paper.

Localising an absorber of variable strength is actually very challenging since western-type commercial nuclear reactors usually do not have many in-core detectors present in the core. This is particularly true for Westinghouse-type PWRs where at the most five in-core neutron detectors can be simultaneously inserted in different instrumentation thimbles of the core [16]. The task of localising a noise source from the detector readings is usually referred to as an unfolding procedure, since the unknown noise source, which has to be characterised, induce a measurable neutron noise. The complexity of the unfolding comes from the fact that several noise sources might exist in the core and from the large number of fuel assemblies in a reactor, i.e. the large number of possible locations for the noise source, compared to the number of available detectors. PWRs typically contain less than 200 fuel assemblies, whereas BWRs typically contain more than 800 fuel assemblies. Even if there is only one noise source present in the core, the unfolding is still very difficult to carry out. An equivalent mathematical formulation of this problem would be the inversion of a matrix where each column would represent the measured neutron noise for one possible location of the noise source. The number of columns would then be the number of possible locations of the actual noise source. Obviously, such an inversion is only possible if the matrix is square, i.e. if the number of available detectors equates the number of fuel assemblies.

Such a problem has already been investigated in the past by Glöckler and Pázsit [17], although the objectives of this study were slightly different as explained in the following. In this earlier work, a 2-D homogeneous rectangular reactor was considered with equally-spaced detectors. An analytical expression for reconstructing any noise source could then be derived in one-group theory and in the frequency domain. This expression was later approximated since the full space-dependence of the induced neutron noise was not known. This technique had the advantage of determining the noise source type (either an absorber of variable strength or a vibrating absorber), and therefore did not require any previous expert knowledge of it. The drawback was that the spatial resolution of the reconstructed noise source was rather poor, i.e. the algorithm could only point out a region of the core where the noise source was likely to be located. Furthermore, such an algorithm could only be used when an analytical expression of the reactor transfer function could be derived, i.e.

when the reactor was homogeneous and rectangular. Such approximations are usually very rough and do not hold in practice. Finally, the detectors needed to be equally-spaced throughout the core and many detectors were required for the algorithm to work properly. As pointed out previously, at the most five in-core neutron detectors are typically available simultaneously in a PWR and are not regularly distributed over the core. The applicability of the method developed by Glöckler and Pázsit was thus limited.

The goal of this Section is to derive new algorithms for identifying and localising absorbers of variable strength for 2-D heterogeneous reactors of arbitrary shape, so that the fuel assembly containing the noise source could be pointed out. One thus assumes that only one localised noise source is present in the core. Although absorbers of variable strength are mostly typical of BWRs, which have a number of 30 to 40 in-core neutron detectors positioned on each of several axial planes of the core, a number of five detectors radially and not regularly distributed throughout the core was chosen. This very limited number of detectors usually corresponds to PWR cores. Having very few available detectors (like for PWR cases) and many fuel assemblies (like for BWR cases) are the most penalizing factors for reconstructing the noise source. Therefore, if the algorithms developed in this study are able to successfully locate the noise source in these conditions, they should also work for more realistic but less stringent cases (fewer fuel assemblies in PWR cores with very few detectors, as many fuel assemblies in BWR cores with much more detectors). It has to be emphasized that contrary to Glöckler and Pázsit [17], the localization algorithms are applied after the successful identification of the type of noise source, i.e. of an absorber of variable strength. The identification and localization are thus two separate processes. Finally, the algorithms are derived for the Fourier transform of the neutron detector time-signals.

The algorithms presented in this Section rely on the estimation of the dynamic reactor transfer function. Due to the heterogeneous character of the core, this transfer function can only be determined numerically. In the first part of this Section, the model of the reactor chosen for this investigation and the modelling tools are presented. Emphasis is then put on using these models to study the space-dependence of the neutron noise induced by localised absorbers of variable strength. The objective of this second part is to verify that the spatial structure of the induced neutron noise is a function of the actual location of the noise source and that this spatial pattern can be monitored by very few detectors far apart from each other and far away from the noise source. The relaxation length of the induced neutron noise and the importance of the point-kinetic component of the neutron noise, whose spatial structure is completely independent of the position of the noise source, are looked at carefully and quantified. Finally, the process of identifying an absorber of variable strength is presented. This is followed by the derivation of different algorithms for localising the noise source and some numerical tests of the performance of each of these algorithms.

1.2 Reactor model and modelling tools

In this part, the reactor model chosen for this study is presented. All the calculations are based on a radial 2-D representation of the reactor and on the 2-group diffusion theory. This model will then be used to determine the so-called Green's function or dynamic reactor transfer function, i.e. the function giving the neutron noise induced by any localised absorber of variable strength. The estimation of this transfer function actually requires the previous determination of the static conditions of the reactor. The tools used for determining both these static conditions and the Green's function are briefly presented. Further details related to these modelling codes can be found in [18].

1.2.1 Reactor model

Since cores with many fuel assemblies are a penalizing factor for the successful identification and localization of a point-like noise source from very few detectors, a realistic commercial BWR core is considered throughout this Section. This core corresponds to the Swedish Forsmark-1 BWR (core-averaged burnup of 22.887 GWd/tHM, cycle 16). This model was already used in the past to explain a radially space-dependent Decay Ratio induced by a channel instability [19], [20]. These conditions were encountered at a reduced power level (63.3% of the nominal power level) and a reduced core flow (41% of the nominal core flow).

SIMULATE-3 calculations were then performed at these operating conditions [21]. The goal of these calculations was to use a state-of-the-art advanced nodal diffusion code, which performs coupled neutronic/thermalhydraulic static calculations and is thus able to determine the 3-D spatial distribution of the different parameters of influence on the macroscopic nuclear cross-sections. These cross-sections were then edited in the 2-group diffusion approximation for each node and were homogenised from 3-D to 2-D in order to be used by the 2-D simulators in this study. The homogenization was naturally carried out by using the static fluxes as weighting functions so that the reaction rates were preserved:

$$XS_{G,I,J} = \frac{\sum_K XS_{G,I,J,K}\phi_{G,0,I,J,K}V_{I,J,K}}{\sum_K \phi_{G,0,I,J,K}V_{I,J,K}} \quad (1)$$

and

$$\phi_{G,0,I,J} = \frac{\sum_K \phi_{G,0,I,J,K}V_{I,J,K}}{\sum_K V_{I,J,K}} \quad (2)$$

with XS_G having a broad meaning, i.e. being D_G, $\Sigma_{a,G}$, Σ_{rem}, or $\nu\Sigma_{f,G}$. G is the group index and (I, J) is a 2-D elementary node. All the other symbols have their usual meaning with $V_{I,J,K}$ representing the volume of the 3-D elementary node (I, J, K). As described in [18], the axial leakage rate were accounted for in the 2-D set of cross-sections by modifying the absorption cross-sections as follows:

$$\Sigma^*_{a,G,I,J,K} = \Sigma_{a,G,I,J,K} + L_{G,I,J,K} \quad (3)$$

with

$$L_{G,I,J,K} = \frac{a^z_{G,I,J,K}\phi_{G,I,J,K} + b^z_{G,I,J,K}\phi_{G,I,J,K+1} + c^z_{G,I,J,K}\phi_{G,I,J,K-1}}{\phi_{G,I,J,K}\times\Delta z} \quad (4)$$

The coefficients $a^z_{G,I,J,K}$, $b^z_{G,I,J,K}$, and $c^z_{G,I,J,K}$ corresponds to a spatial discretization performed according to a finite difference "box-scheme" [22] and are given in a generic form in Table I.

A layout of the Forsmark-1 core considered in this study is presented in Fig. 1. Five neutron detectors are subsequently used for unfolding purposes and they are also represented in this Figure. It can be noticed that the location of these detectors was chosen

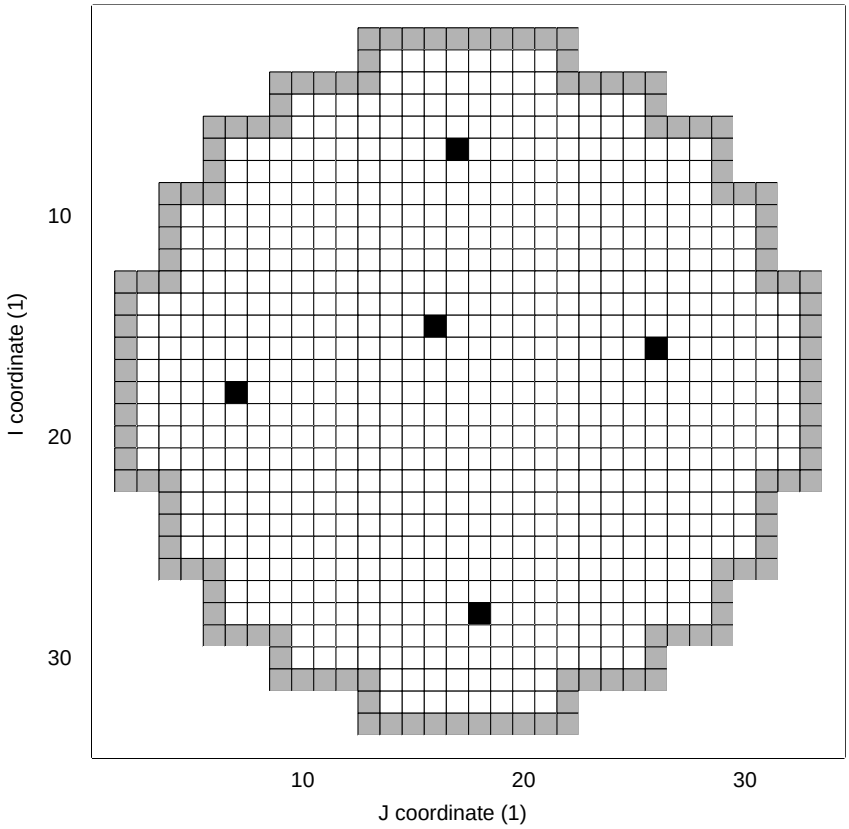

Fig. 1. *Layout of the core used in this investigation (with the reflector nodes in gray, the fuel nodes in white, and the nodes containing detectors in black)*

Table I. Coupling coefficients in the *i*-direction for the finite differences "box-scheme".

	$a^{i}_{G,N}$	$b^{i}_{G,N}$	$c^{i}_{G,N}$
if the node *N-1* does not exist	$\frac{2D_{G,N}D_{G,N+1}}{\Delta i(D_{G,N}+D_{G,N+1})} + \frac{2D_{G,N}}{\Delta i}$	$\frac{2D_{G,N}D_{G,N+1}}{\Delta i(D_{G,N}+D_{G,N+1})}$	0
if the nodes *N-1* and *N+1* both exist	$\frac{2D_{G,N}D_{G,N+1}}{\Delta i(D_{G,N}+D_{G,N+1})} + \frac{2D_{G,N}D_{G,N-1}}{\Delta i(D_{G,N}+D_{G,N-1})}$	$-\frac{2D_{G,N}D_{G,N+1}}{\Delta i(D_{G,N}+D_{G,N+1})}$	$\frac{2D_{G,N}D_{G,N-1}}{\Delta i(D_{G,N}+D_{G,N-1})}$
if the node *N+1* does not exist	$\frac{2D_{G,N}}{\Delta i} + \frac{2D_{G,N}D_{G,N-1}}{\Delta i(D_{G,N}+D_{G,N-1})}$	0	$-\frac{2D_{G,N}D_{G,N-1}}{\Delta i(D_{G,N}+D_{G,N-1})}$

so that they cover the whole core and monitor different regions. It has to be emphasized that the detectors do not need to be regularly spaced. Furthermore, detectors in BWRs are in principle located between four fuel assemblies in the so-called wide water gaps. One detector is thus sensitive to its four neighbouring fuel assemblies, case that can be considered as less stringent for unfolding purposes. Therefore, the detectors were assumed to be located within fuel assemblies, like in PWR cases, since this situation makes the unfolding more difficult.

1.2.2 Static simulators

Although the spatial distribution of the static fluxes in the 2-group diffusion approximation is available from SIMULATE-3, the spatial discretization scheme used in SIMULATE-3 is not compatible with the one used in the dynamic simulator presented in the following [18]. Using the fluxes directly from SIMULATE-3 without any modification would be equivalent to make the reactor non-critical. Therefore, the static fluxes and the corresponding adjoint functions need to be recalculated using the same discretization scheme as the one on which the noise simulator relies. The basic features of these static simulators are briefly recalled here. The reader is referred to [18] for further details.

The static core simulator solves the following matrix equation in the two-group diffusion approximation:

$$[\nabla \cdot \overline{\overline{D}}(\boldsymbol{r})\nabla + \overline{\overline{\Sigma}}_{sta}(\boldsymbol{r})] \times \begin{bmatrix} \phi_{1,0}(\boldsymbol{r}) \\ \phi_{2,0}(\boldsymbol{r}) \end{bmatrix} = 0 \tag{5}$$

where

$$\overline{\overline{D}}(\boldsymbol{r}) = \begin{bmatrix} D_1(\boldsymbol{r}) & 0 \\ 0 & D_2(\boldsymbol{r}) \end{bmatrix} \tag{6}$$

$$\overline{\overline{\Sigma}}_{sta}(\boldsymbol{r}) = \begin{bmatrix} \dfrac{\nu\Sigma_{f,1,0}(\boldsymbol{r})}{k_{eff}} - \Sigma_{a,1,0}(\boldsymbol{r}) - \Sigma_{rem,0}(\boldsymbol{r}) & \dfrac{\nu\Sigma_{f,2,0}(\boldsymbol{r})}{k_{eff}} \\ \Sigma_{rem,0}(\boldsymbol{r}) & -\Sigma_{a,2,0}(\boldsymbol{r}) \end{bmatrix} \tag{7}$$

All the notations have their usual meaning. Finite differences are used to carry out the 2-D spatial discretization of the system according to the so-called “box-scheme” [22]. Eq. (5), which is a homogeneous equation, is solved by using an iterative scheme, more exactly the power iteration method [22], [23]. The results are then scaled since Eq. (5) is a homogeneous equation. The scaling factor is calculated so that the power level corresponds to the one given by SIMULATE-3 in the axially condensed reactor:

$$\sum_{fuel} [\kappa_{1,I,J}\phi_{1,0,I,J} + \kappa_{2,I,J}\phi_{2,0,I,J}]\Big|_{\text{static core simulator}} = \sum_{fuel} [\kappa_{1,I,J}\phi_{1,0,I,J} + \kappa_{2,I,J}\phi_{2,0,I,J}]\Big|_{\text{SIMULATE-3}} \tag{8}$$

where $\kappa_{1,I,J}$ and $\kappa_{2,I,J}$ are the energy release per fast and thermal fission respectively for a given node (*I*, *J*).

As will be seen later in this Section, the adjoint function of the static flux is required if one wants to determine the point-kinetic response of the reactor to perturbations in 2-group diffusion theory. According to the definition of the adjoint given in [18] and [23], the adjoint function of the static flux can be estimated by solving the following matrix equation:

$$[\nabla \cdot \overline{\overline{D}}(\boldsymbol{r})\nabla + \overline{\overline{\Sigma}}^{T}_{sta}(\boldsymbol{r})] \times \begin{bmatrix} \phi^{+}_{1,0}(\boldsymbol{r}) \\ \phi^{+}_{2,0}(\boldsymbol{r}) \end{bmatrix} = 0 \tag{9}$$

where the superscript T denotes the matrix transpose. As before, finite differences are used to carry out the 2-D spatial discretization of the system according to the so-called "box-scheme" [22] and the power method is used to solve Eq. (9) iteratively [22], [23]. The results are then scaled since Eq. (9) is a homogeneous equation. The scaling factor is calculated so that the volume integral of the fast adjoint function is equal to unity:

$$\frac{1}{N_{fuel}} \sum_{fuel} \phi^{+}_{1,0,I,J} = 1 \tag{10}$$

where N_{fuel} is the number of nodes in the fuel region.

Benchmarking of both the static simulator and its adjoint were successfully carried out in [18].

1.2.3 Dynamic simulators

After the use of these static simulators, which determine the static fluxes, the corresponding adjoint functions, and their associated eigenvalues, the estimation of the dynamic reactor transfer function can be performed since the discretised static system is critical.

The neutron noise simulator solves the following matrix equation in the 2-group diffusion approximation at a given frequency ω, for fluctuations of any type of macroscopic cross-section:

$$[\nabla \cdot \overline{\overline{D}}(\boldsymbol{r})\nabla + \overline{\overline{\Sigma}}_{dyn}(\boldsymbol{r}, \omega)] \times \overline{G}_{XS}(\boldsymbol{r}, \boldsymbol{r}_P, \omega) = \bar{\delta}_{XS}(\boldsymbol{r} - \boldsymbol{r}_P) \tag{11}$$

where $\overline{G}_{XS}(\boldsymbol{r}, \boldsymbol{r}_P, \omega)$ is the so-called Green's function, i.e. represents the neutron noise at the position $\boldsymbol{r}$ and frequency ω induced by a point-like noise source located at $\boldsymbol{r}_P$. This Green's function is slightly different from its usual definition (see for instance [24]). For the sake of brevity, the noise source in Eq. (11) is simply written as $\bar{\delta}_{XS}(\boldsymbol{r} - \boldsymbol{r}_P)$, which is a two-component vector. Depending on the nature of the noise source, the exact expression of the noise source $\bar{\delta}_{XS}(\boldsymbol{r} - \boldsymbol{r}_P)$ can be found in [18]. In this study, it was assumed that the thermal macroscopic absorption cross-section was perturbed. In such a case, one gets:

$$\bar{\delta}_{\Sigma_a}(\boldsymbol{r} - \boldsymbol{r}_P) = \begin{bmatrix} 0 \\ \phi_{2,0}(\boldsymbol{r})\delta(\boldsymbol{r} - \boldsymbol{r}_P) \end{bmatrix} \tag{12}$$

It is believed that the results of the unfolding algorithms are independent of the choice of the nature of the noise source (perturbation of the fast or thermal macroscopic cross-section, of the fast or thermal fission cross-section, of the removal cross-section). The matrix $\overline{\overline{\Sigma}}_{dyn}(\boldsymbol{r}, \omega)$ in Eq. (11) is given as:

$$\bar{\bar{\Sigma}}_{dyn}(\boldsymbol{r}, \omega) = \begin{bmatrix} -\Sigma_1(\boldsymbol{r}, \omega) & \dfrac{\nu\Sigma_{f,2,0}(\boldsymbol{r})}{k_{eff}}\left(1 - \dfrac{i\omega\beta_{eff}}{i\omega + \lambda}\right) \\ \Sigma_{rem,0}(\boldsymbol{r}) & -\left(\Sigma_{a,2,0}(\boldsymbol{r}) + \dfrac{i\omega}{v_2}\right) \end{bmatrix} \tag{13}$$

with

$$\Sigma_1(\boldsymbol{r}, \omega) = \Sigma_{a,1,0}(\boldsymbol{r}) + \frac{i\omega}{v_1} + \Sigma_{rem,0}(\boldsymbol{r}) - \frac{\nu\Sigma_{f,1,0}(\boldsymbol{r})}{k_{eff}}\left(1 - \frac{i\omega\beta_{eff}}{i\omega + \lambda}\right) \tag{14}$$

As for the static core simulator, finite differences are used to carry out the 2-D spatial discretization of the system according to the so-called “box-scheme” [22]. Eq. (11), which is an inhomogeneous equation, is then solved by direct matrix inversion. The neutron noise simulator is thus able to calculate the spatial distribution of the neutron noise induced by any localised (or even spatially distributed) noise sources, of the absorber of variable strength type.

If one assumes that the perturbation of the macroscopic cross-section corresponding to a vibrating absorber can be modelled by the Feinberg-Galanin model [13] as:

$$\delta XS(\boldsymbol{r}, t) = \gamma \cdot \{\delta[\boldsymbol{r} - \boldsymbol{r}_P - \bar{\varepsilon}(t)] - \delta(\boldsymbol{r} - \boldsymbol{r}_P)\}, \tag{15}$$

then the induced neutron noise can be approximated as [24]:

$$\begin{bmatrix} \delta\phi_1(\boldsymbol{r}, \omega) \\ \delta\phi_2(\boldsymbol{r}, \omega) \end{bmatrix} = \gamma \cdot \bar{\varepsilon}(\omega) \cdot \nabla_{\boldsymbol{r}_P}[\bar{G}_{\delta XS}(\boldsymbol{r}, \boldsymbol{r}_P, \omega)] \tag{16}$$

where γ is the strength of the perturbation, and $\boldsymbol{r}_P$ its equilibrium position in the Feinberg-Galanin model. The vector $\bar{\varepsilon}(t)$ describes the 2-D vibrations of the noise source around its equilibrium position. It is actually much more practical to estimate the neutron noise induced by a vibrating absorber from the adjoint of the Green’s function, since in such a case the gradient refers to the first variable of the adjoint of the Green’s function [25]. This reads as follows:

$$\begin{bmatrix} \delta\phi_1(\boldsymbol{r}_0, \omega) \\ \delta\phi_2(\boldsymbol{r}_0, \omega) \end{bmatrix} = \gamma \cdot \bar{\varepsilon}(\omega) \cdot \nabla_{\boldsymbol{r}_P}[\bar{G}^{+}_{\delta XS}(\boldsymbol{r}_P, \boldsymbol{r}_0, \omega)] \tag{17}$$

where the adjoint of the Green’s function fulfils the following Equation:

$$[\nabla \cdot \bar{\bar{D}}(\boldsymbol{r})\nabla + \bar{\bar{\Sigma}}^{T}_{dyn}(\boldsymbol{r}, \omega)] \times \bar{G}^{+}_{\delta XS}(\boldsymbol{r}, \boldsymbol{r}_0, \omega) = \begin{bmatrix} \delta(\boldsymbol{r} - \boldsymbol{r}_0) \\ \delta(\boldsymbol{r} - \boldsymbol{r}_0) \end{bmatrix} \tag{18}$$

Although this paper focuses on the identification and localization of absorbers of variable strength, this type of noise source has to be recognized and distinguished from vibrating absorbers. Such an identification is presented later on, where the neutron noise induced by a vibrating absorber is needed for comparison purposes. Therefore, the use of the simulator calculating the adjoint of the Green’s function is required. As before, finite differences are used to carry out the 2-D spatial discretization of the system according to the so-called

"box-scheme" [22]. Eq. (18), which is an inhomogeneous equation, is then solved by direct matrix inversion.

Benchmarking of both the noise simulator and its adjoint were successfully carried out in [18].

1.3 Investigation of the space-dependence of the neutron noise induced by localised absorbers of variable strength

Prior to perform any unfolding from the neutron noise, it is essential to investigate the ability of very few detectors distributed throughout the core to detect any point-like absorber of variable strength. The purpose of this part is thus to look at the space-dependence of the neutron noise and to compare its relaxation length to the radius of the core. This analysis is performed first on a 2-D homogeneous reactor, and is then extended to a 2-D heterogeneous reactor. Since neutron detectors are mostly sensitive to the thermal flux, only the thermal neutron noise is considered in the following.

1.3.1 The different components of the neutron noise

In order to characterize and illustrate the space-dependence of the neutron noise induced by a localised absorber of variable strength and to get some physical insight, a 2-D homogeneous reactor with a central perturbation is first considered. This allows having a relatively simple semi-analytical solution for the neutron noise. The model of the reactor corresponds to the one presented previously after a proper spatial homogenization.

If R denotes the extrapolated reactor radius, solving Eq. (5) for the static flux gives the following solution:

$$\begin{bmatrix} \phi_{1,0}(r) \\ \phi_{2,0}(r) \end{bmatrix} = \begin{bmatrix} 1 \\ \dfrac{\Sigma_{rem,0}}{D_2 B_g^2 + \Sigma_{a,2,0}} \end{bmatrix} \times A \times J_0(B_g r) \tag{19}$$

with

$$B_g^2 = \left(\frac{j_0}{R}\right)^2 \tag{20}$$

being the geometrical buckling and r being the distance from the core centre. In the previous Equations, A is a normalization constant, and j_0 is the first root of the Bessel function of the first kind and zero order J_0. The corresponding eigenvalue is then given by:

$$k_{eff} = \frac{\nu\Sigma_{f,0}^{*} \times \Sigma_{rem,0}}{\Sigma_{a,2,0} \times (\Sigma_{a,1,0} + \Sigma_{rem,0})} \times \frac{1}{1 + L_1^2 B_g^2} \times \frac{1}{1 + L_2^2 B_g^2} \tag{21}$$

with

$$\nu\Sigma_{f,0}^{*} = \nu\Sigma_{f,0,2} + \nu\Sigma_{f,0,1} \times \frac{D_2 B_g^2 + \Sigma_{a,2,0}}{\Sigma_{rem,0}} \tag{22}$$

$$L_1^2 = \frac{D_1}{\Sigma_{a,1,0} + \Sigma_{rem,0}} \tag{23}$$

$$L_2^2 = \frac{D_2}{\Sigma_{a,\,2,\,0}} \tag{24}$$

Likewise, solving Eq. (9) for the adjoint function of the static flux gives the following solution:

$$\begin{bmatrix} \phi_{1,\,0}^{+}(r) \\ \phi_{2,\,0}^{+}(r) \end{bmatrix} = \begin{bmatrix} 1 \\ \dfrac{\nu\Sigma_{f,\,2,\,0}/k_{eff}^{+}}{D_2 B_g^2 + \Sigma_{a,\,2,\,0}} \end{bmatrix} \times B \times J_0(B_g r) \tag{25}$$

where B is a normalization constant and $k_{eff}^{+} = k_{eff}$.

Since the noise source is located in the middle of the core, the results are rotational-invariant around the z-axis crossing the core centre. Therefore only the radial dependence of the neutron noise needs to be accounted for. Solving Eq. (11) for the neutron noise induced by a central noise source given by Eq. (12) gives the following solution:

$$\delta\phi_1(r,\omega) = C \times K_0(\lambda r) + D \times I_0(\lambda r) + E \times Y_0(\mu r) + F \times J_0(\mu r) \tag{26}$$

$$\delta\phi_2(r,\omega) = C \times c_\lambda \times K_0(\lambda r) + D \times c_\lambda \times I_0(\lambda r) + E \times c_\mu \times Y_0(\mu r) + F \times c_\mu \times J_0(\mu r) \tag{27}$$

where $-\lambda^2$ and μ^2 are the two eigenvalues of the following matrix:

$$\begin{bmatrix} -\dfrac{\Sigma_1(\omega)}{D_1} & \dfrac{\nu\Sigma_{f,\,2,\,0}}{k_{eff} D_1}\left(1 - \dfrac{i\omega\beta_{eff}}{i\omega + \lambda}\right) \\ \dfrac{\Sigma_{rem,\,0}}{D_2} & -\dfrac{1}{D_2}\left(\Sigma_{a,\,2,\,0} + \dfrac{i\omega}{v_2}\right) \end{bmatrix} \tag{28}$$

and the coupling coefficient c_λ and c_μ are given as follows:

$$c_\lambda = \frac{\Sigma_{rem,\,0}}{\left(\Sigma_{a,\,2,\,0} + \dfrac{i\omega}{v_2}\right) - D_2\lambda^2} \tag{29}$$

$$c_\mu = \frac{\Sigma_{rem,\,0}}{\left(\Sigma_{a,\,2,\,0} + \dfrac{i\omega}{v_2}\right) + D_2\mu^2} \tag{30}$$

The coefficients C, D, E, and F are solutions of the following equation, which expresses the fact that the neutron noise vanishes at the boundary of the system and that the current of the neutron noise is driven by the central noise source:

$$\begin{bmatrix} K_0(\lambda R) & I_0(\lambda R) & Y_0(\mu R) & J_0(\mu R) \\ c_\lambda \times K_0(\lambda R) & c_\lambda \times I_0(\lambda R) & c_\mu \times Y_0(\mu R) & c_\mu \times J_0(\mu R) \\ -1 & 0 & -[\mu r \times Y_1(\mu r)]_{r \to 0} & 0 \\ -c_\lambda & 0 & -c_\mu \times [\mu r \times Y_1(\mu r)]_{r \to 0} & 0 \end{bmatrix} \times \begin{bmatrix} C \\ D \\ E \\ F \end{bmatrix} = \begin{bmatrix} 0 \\ 0 \\ 0 \\ -\frac{1}{2\pi D_2}\phi_{1,0}(0) \end{bmatrix} \quad (31)$$

In the previous Equations, the functions I_n, J_n, K_n, and Y_n are the modified Bessel function of the first kind, the Bessel function of the first kind, the modified Bessel function of the second kind, and the Bessel function of the second kind, respectively with n being the order of the different functions. Eq. (31) can thus be solved numerically in order to find the coefficients C, D, E, and F. Since the $I_0(r)$ Bessel function diverges for increasing values of r, the constant D is obviously found to be equal to zero. The neutron noise can thus be seen as a superposition of two terms:

$$\begin{bmatrix} \delta\phi_1(r,\omega) \\ \delta\phi_2(r,\omega) \end{bmatrix} = \begin{bmatrix} 1 \\ c_\lambda \end{bmatrix} \times \delta\phi^{local}(r) + \begin{bmatrix} 1 \\ c_\mu \end{bmatrix} \times \delta\phi^{global}(r) \quad (32)$$

where

$$\delta\phi^{local}(r) = C \times K_0(\lambda r) \quad (33)$$

and

$$\delta\phi^{global}(r) = E \times Y_0(\mu r) + F \times J_0(\mu r) \quad (34)$$

Close to the noise source, i.e. close to the core centre, the two terms can be approximated by [26]:

$$\delta\phi^{local}(r)\big|_{r \to 0} = C \times K_0(\lambda r)\big|_{r \to 0} = -C \times \left(\gamma + \ln\frac{\lambda r}{2}\right) \quad (35)$$

and

$$\delta\phi^{global}(r)\big|_{r \to 0} = E \times Y_0(\mu r)\big|_{r \to 0} + F \times J_0(\mu r)\big|_{r \to 0} = \frac{2 \times E}{\pi} \times \left(\gamma + \ln\frac{\mu r}{2}\right) + F \quad (36)$$

where γ is the Euler constant. It can then be seen that the spatial relaxation of these two terms is determined by λ and μ. Usually, $\|\lambda\| \gg \|\mu\|$. Thus, the spatial variation of the neutron noise associated to the eigenvalue λ is large on very short distances, whereas the spatial variation of the neutron noise associated to the eigenvalue μ is moderate on large distances. The first term is therefore referred to as the local component of the neutron noise, while the second term is referred to as the global component [27]-[29].

Another way of representing the time-dependent neutron flux is to factorize it into an amplitude function $P(t)$ and a shape function $\psi_i(\boldsymbol{r}, t)$ (with i being the group index). This reads as [23]:

$$\begin{bmatrix} \phi_1(\boldsymbol{r}, t) \\ \phi_2(\boldsymbol{r}, t) \end{bmatrix} = P(t) \times \begin{bmatrix} \psi_1(\boldsymbol{r}, t) \\ \psi_2(\boldsymbol{r}, t) \end{bmatrix} \tag{37}$$

Although there are several ways of normalizing the shape function, it is usually assumed that [23]:

$$\frac{\partial}{\partial t}\int \left[\frac{1}{v_1}\phi^+_{1,0}(\boldsymbol{r})\psi_1(\boldsymbol{r}, t) + \frac{1}{v_2}\phi^+_{2,0}(\boldsymbol{r})\psi_2(\boldsymbol{r}, t)\right] d\boldsymbol{r} = 0 . \tag{38}$$

Furthermore, one has:

$$\begin{bmatrix} \phi_1(\boldsymbol{r}, 0) \\ \phi_2(\boldsymbol{r}, 0) \end{bmatrix} = \begin{bmatrix} \psi_1(\boldsymbol{r}, t = 0) \\ \psi_2(\boldsymbol{r}, t = 0) \end{bmatrix} \tag{39}$$

which is equivalent to

$$P(0) = 1 . \tag{40}$$

Splitting the time-dependent shape function into a steady-state value and fluctuations as

$$\begin{bmatrix} \psi_1(\boldsymbol{r}, t) \\ \psi_2(\boldsymbol{r}, t) \end{bmatrix} = \begin{bmatrix} \phi_1(\boldsymbol{r}, 0) \\ \phi_2(\boldsymbol{r}, 0) \end{bmatrix} + \begin{bmatrix} \delta\psi_1(\boldsymbol{r}, t) \\ \delta\psi_2(\boldsymbol{r}, t) \end{bmatrix} \tag{41}$$

allows writing Eq. (38) in the following form:

$$\int \left[\frac{1}{v_1}\phi^+_{1,0}(\boldsymbol{r})\phi_1(\boldsymbol{r}, 0) + \frac{1}{v_2}\phi^+_{2,0}(\boldsymbol{r})\phi_2(\boldsymbol{r}, 0)\right] d\boldsymbol{r} \quad , \tag{42}$$

$$= \int \left\{ \frac{1}{v_1}\phi^+_{1,0}(\boldsymbol{r}) \times [\phi_1(\boldsymbol{r}, 0) + \delta\psi_1(\boldsymbol{r}, t)] + \frac{1}{v_2}\phi^+_{2,0}(\boldsymbol{r}) \times [\phi_2(\boldsymbol{r}, 0) + \delta\psi_2(\boldsymbol{r}, t)] \right\} d\boldsymbol{r}$$

from which one deduces that:

$$\int \left[\frac{1}{v_1}\phi^+_{1,0}(\boldsymbol{r}) \times \delta\psi_1(\boldsymbol{r}, t) + \frac{1}{v_2}\phi^+_{2,0}(\boldsymbol{r}) \times \delta\psi_2(\boldsymbol{r}, t)\right] d\boldsymbol{r} = 0 . \tag{43}$$

Similarly, splitting the time-dependent neutron noise into a steady-state value and fluctuations allows rewriting Eq. (37) as:

$$\begin{bmatrix} \delta\phi_1(\boldsymbol{r}, t) \\ \delta\phi_2(\boldsymbol{r}, t) \end{bmatrix} = \delta P(t) \times \begin{bmatrix} \phi_1(\boldsymbol{r}, 0) \\ \phi_2(\boldsymbol{r}, 0) \end{bmatrix} + \begin{bmatrix} \delta\psi_1(\boldsymbol{r}, t) \\ \delta\psi_2(\boldsymbol{r}, t) \end{bmatrix} \tag{44}$$

where second-order terms have been neglected. The first term on the right hand-side of Eq. (44) is the so-called point-kinetic component of the neutron noise, whereas the remaining component corresponds to the fluctuations of the shape function. In the frequency-domain, this reads as:

$$\begin{bmatrix} \delta\phi_1(\boldsymbol{r}, \omega) \\ \delta\phi_2(\boldsymbol{r}, \omega) \end{bmatrix} = \delta P(\omega) \times \begin{bmatrix} \phi_1(\boldsymbol{r}, 0) \\ \phi_2(\boldsymbol{r}, 0) \end{bmatrix} + \begin{bmatrix} \delta\psi_1(\boldsymbol{r}, \omega) \\ \delta\psi_2(\boldsymbol{r}, \omega) \end{bmatrix} \tag{45}$$

1.3.2 Evaluation of the space-dependence of the neutron noise

In order to get some physical insight about the space-dependence of the neutron noise induced by a localised absorber, it is interesting to first consider the homogeneous model and both ways of representing the neutron noise, i.e. either the local/global components of the neutron noise [Eqs. (32)-(34)] or the point-kinetic/remaining components of the neutron noise [Eq. (45)]. The actual corresponding 2-D heterogeneous reactor will then be considered, for which all the calculations will be performed with the simulators presented previously. In this second case, non-central noise sources will also be studied.

It can easily be understood from Eq. (45) that only the fluctuations of the shape function are able to carry information about the location of a noise source, since the point-kinetic component has always the same spatial dependence given by the static fluxes, whatever the location of the noise source is. For localization purposes, it has thus to be verified that the point-kinetic response of the reactor is not overwhelmingly large compared to the space-dependent fluctuations of the shape function. Assuming that the neutron noise is known, the fluctuations of the amplitude function can be estimated from Eqs. (43) and (44), which reads in the frequency domain as:

$$\delta P(\omega) = \frac{\int \left[\frac{1}{v_1} \phi^+_{1,0}(\boldsymbol{r}) \times \delta\phi_1(\boldsymbol{r}, \omega) + \frac{1}{v_2} \phi^+_{2,0}(\boldsymbol{r}) \times \delta\phi_2(\boldsymbol{r}, \omega) \right] d\boldsymbol{r}}{\int \left[\frac{1}{v_1} \phi^+_{1,0}(\boldsymbol{r}) \times \phi_{1,0}(\boldsymbol{r}) + \frac{1}{v_2} \phi^+_{2,0}(\boldsymbol{r}) \times \phi_{2,0}(\boldsymbol{r}) \right] d\boldsymbol{r}} \tag{46}$$

from which the point-kinetic response of the reactor is determined by multiplying $\delta P(\omega)$ with the static flux.

Similarly, it has to be verified that the relaxation length of the global component of the neutron noise in Eqs. (32)-(34) is large enough so that the neutron noise measured by distant neutron detectors still carry information about the location of the noise source. In the case of the homogeneous model with a central noise source, it has to be emphasized that the $J_0(\mu r)$ contribution to the global component differs from the point-kinetic response of the reactor for two main reasons. Although the static flux is also distributed according to the Bessel function of the first kind and zero order J_0, the eigenvalue μ^2 is different from the geometrical buckling B_g^2. Furthermore, the strength F of the $J_0(\mu r)$ contribution to the global component does not coincide with the magnitude of the point-kinetic term, i.e.

$$F \neq \delta P(\omega) \tag{47}$$

The results for the 2-D homogeneous reactor with a central perturbation are presented in Figs. 2 and 3. As can be seen in these Figures, the reactor does not behave in a point-kinetic way. This is in agreement with the conclusions drawn by [28] and [30] for large power reactors. Close to the noise source, the neutron noise is much larger than the point-kinetic component, whereas the actual neutron noise is much smaller than the point-kinetic component further away from the noise source (deviation of up to 40% close to the reactor boundary). Concerning the relaxation lengths of both the local and the global components, one finds that $1/\|\lambda\| \approx 2.5$ cm and $1/\|\mu\| \approx 144.3$ cm, respectively. Compared to the core radius of $R \approx 245.3$ cm, it is obvious that the local component cannot be recorded by

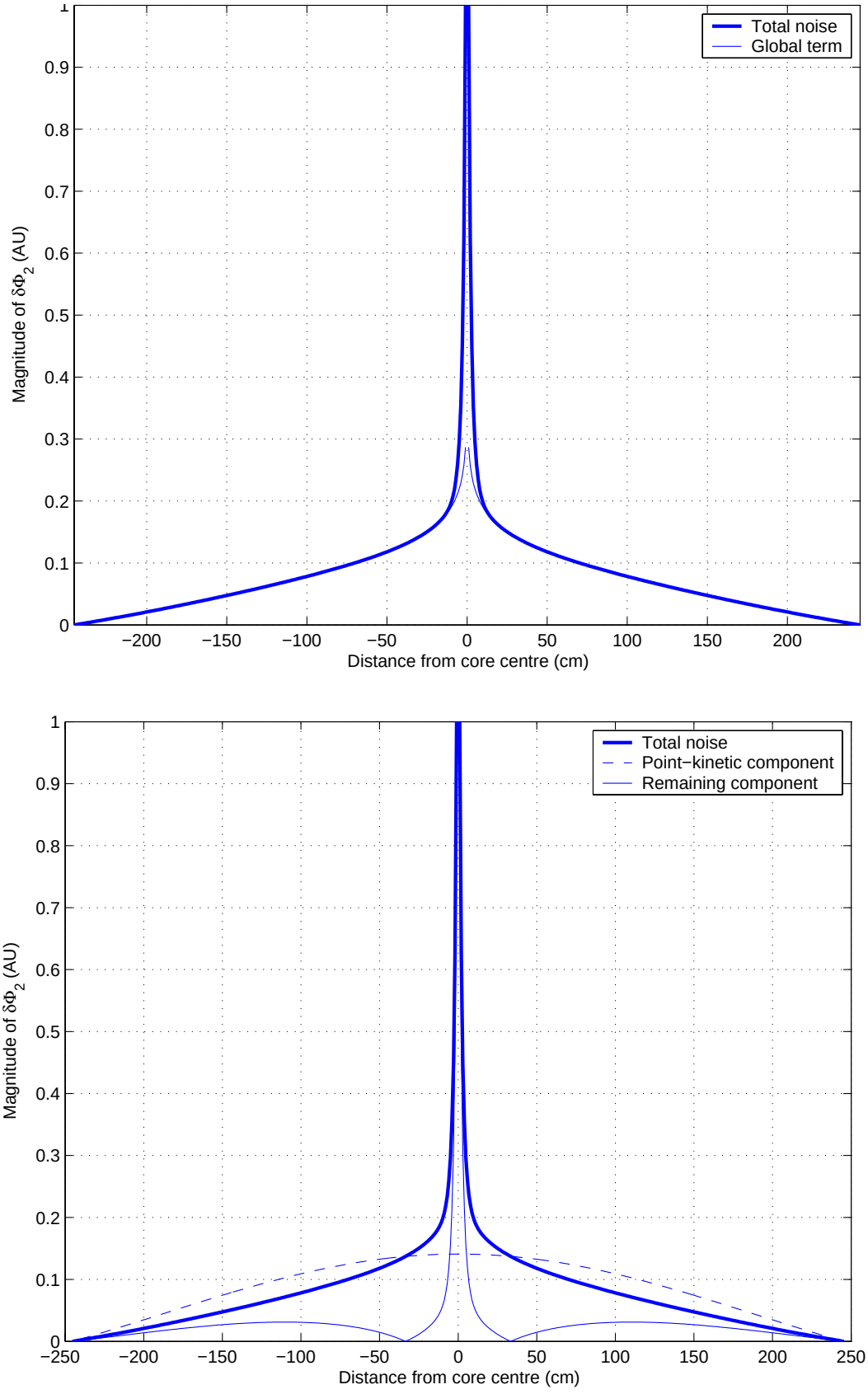

Fig. 2. *The different components of the thermal neutron noise induced by a central noise source in a 2-D homogeneous reactor at a frequency of 1 Hz (all the plots are normalized to the same value)*

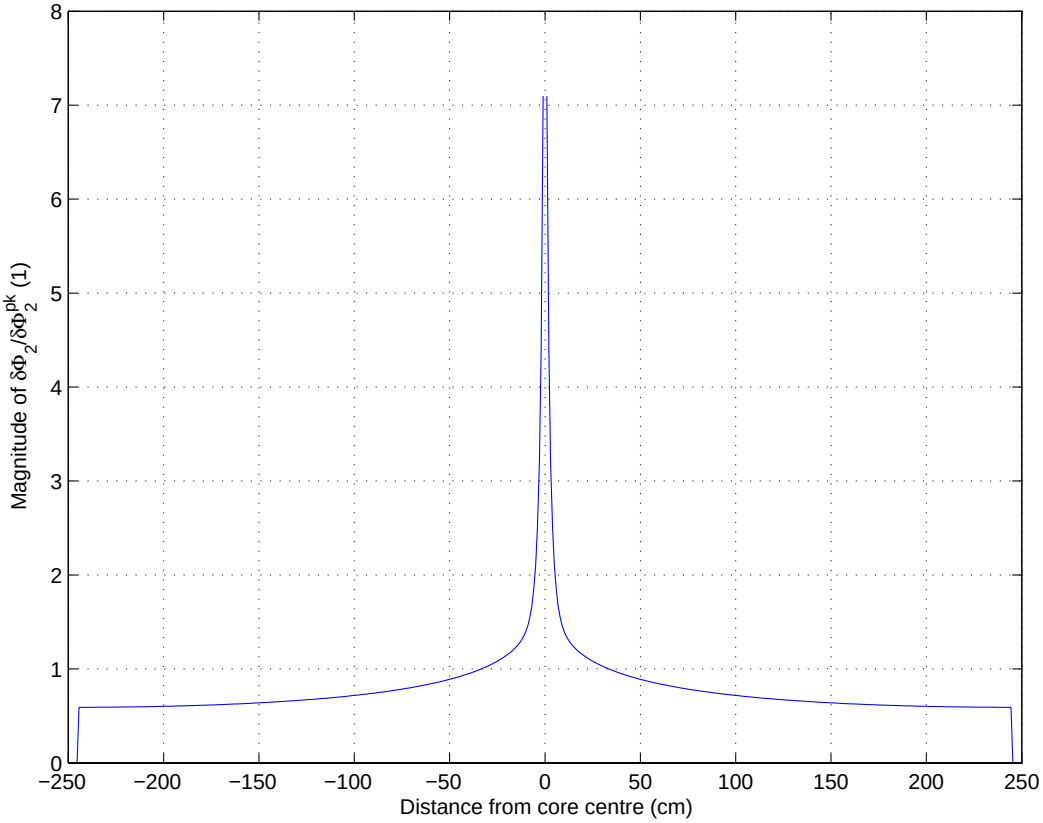

Fig. 3. *Deviation from point-kinetics of the thermal neutron noise induced by a central noise source in a 2-D homogeneous reactor at a frequency of 1 Hz*

neutron detectors located far away from the noise source. Since the reactor does not respond in a point-kinetic manner and since the relaxation length of the global component is large enough, distant neutron detectors can easily monitor this component. Consequently, localising a noise source from very few neutron detectors is possible.

It can be pointed out that even if the point-kinetic component was large compared to the fluctuations of the shape function, this component could be removed from the detector signals by using Eq. (46), either in the frequency- or time-domain. Due to the limited number of detectors, the integrals in this Equation would be approximated by a sum over the number N of available detectors as follows:

$$\delta P(\omega) \approx \frac{\sum_{i=1}^{N} \left[\frac{1}{\nu_1} \phi_{1,0}^{+}(\boldsymbol{r}_i) \times \delta\phi_1(\boldsymbol{r}_i, \omega) + \frac{1}{\nu_2} \phi_{2,0}^{+}(\boldsymbol{r}_i) \times \delta\phi_2(\boldsymbol{r}_i, \omega) \right]}{\sum_{i=1}^{N} \left[\frac{1}{\nu_1} \phi_{1,0}^{+}(\boldsymbol{r}_i) \times \phi_{1,0}(\boldsymbol{r}_i) + \frac{1}{\nu_2} \phi_{2,0}^{+}(\boldsymbol{r}_i) \times \phi_{2,0}(\boldsymbol{r}_i) \right]} \tag{48}$$

The removal of the point-kinetic component, although feasible, would nevertheless present some limitations. The major one would be related to the fact that neutron detectors are usually sensitive to the thermal neutron flux, i.e. the fast static flux and neutron noise cannot be measured in practice. Another problem would surface with the limited number of detectors and how well Eq. (48) approximates the point-kinetic component of the neutron noise with so few detectors. It can also be seen that the calculation of the adjoint function of

the static flux would be required for evaluating the sums in Eq. (48). Finally, since the unfolding algorithms are based on the estimation of the reactor transfer function, this transfer function would need to be corrected in order to remove the point-kinetic term and ensure compatibility with the signals of the detectors that are used for performing the unfolding.

The results when considering a 2-D heterogeneous reactor are presented in Figs. 4 and 5 for a central noise source, and in Figs. 6 and 7 for a peripheral noise source. Although the extrapolation lengths associated to the local and global components cannot be formally estimated in a heterogeneous system, the local and global components are still clearly visible. As for the 2-D homogeneous case, the deviation from point-kinetics and the relaxation length of the global component are large enough to allow the localization of a noise source from very few distant neutron detectors. This is true irrespective of the location of the actual noise source.

Consequently, it was demonstrated that localising an absorber of variable strength by using a limited number of neutron detectors that might be located far away from the perturbation is possible. The next Section thus considers the different algorithms to be used for performing this unfolding.

1.4 Noise source unfolding

Since the purpose of this paper is to study the ability of different unfolding algorithms to identify and localise a noise source of the type absorber of variable strength, the neutron noise induced by such a noise source has first to be calculated. The neutron noise induced at the location of the in-core neutron detectors (see Fig. 1) is then used as input to the unfolding procedures. The result of this unfolding is compared to the actual known location of the noise source.

1.4.1 Identification of the noise source type

Before applying different unfolding algorithms, the type of noise source has to be identified, since these algorithms rely on the hypothesis that the noise source is of the absorber of variable strength type.

There are in principle two types of localised noise sources: a localised absorber of variable strength [as modelled by Eq. (12)], and a localised vibrating absorber [as modelled by Eq. (15)]. A core can also contain a combination of any of these noise sources. Nevertheless, spatially-distributed and multiple noise sources have to be disregarded in this study due to the limited number of available neutron detectors. There are actually many different spatially-distributed and/or multiple noise sources that can induce the same neutron noise recorded at only a few detector locations. In other words, the unfolding in such cases is impossible since there is no uniqueness of the noise source. The thermal neutron noise induced by a vibrating absorber is represented in Fig. 8, whereas the thermal neutron noise induced by a localised absorber of variable strength is given in Fig. 9. As can be seen in these Figures, the neutron noise exhibits a spatial signature that is typical of the type of noise source. Nevertheless, due to the limited number of detectors, it is not obvious that the magnitude of the neutron noise measured at the location of the detectors would give a clear distinction between a localised absorber of variable strength and a vibrating absorber. On the other hand, the phase of the induced neutron noise at the location of the detectors allows easily determining the type of noise source. In the case of a localised absorber of variable strength, all the detectors present an in-phase behaviour. In the case of

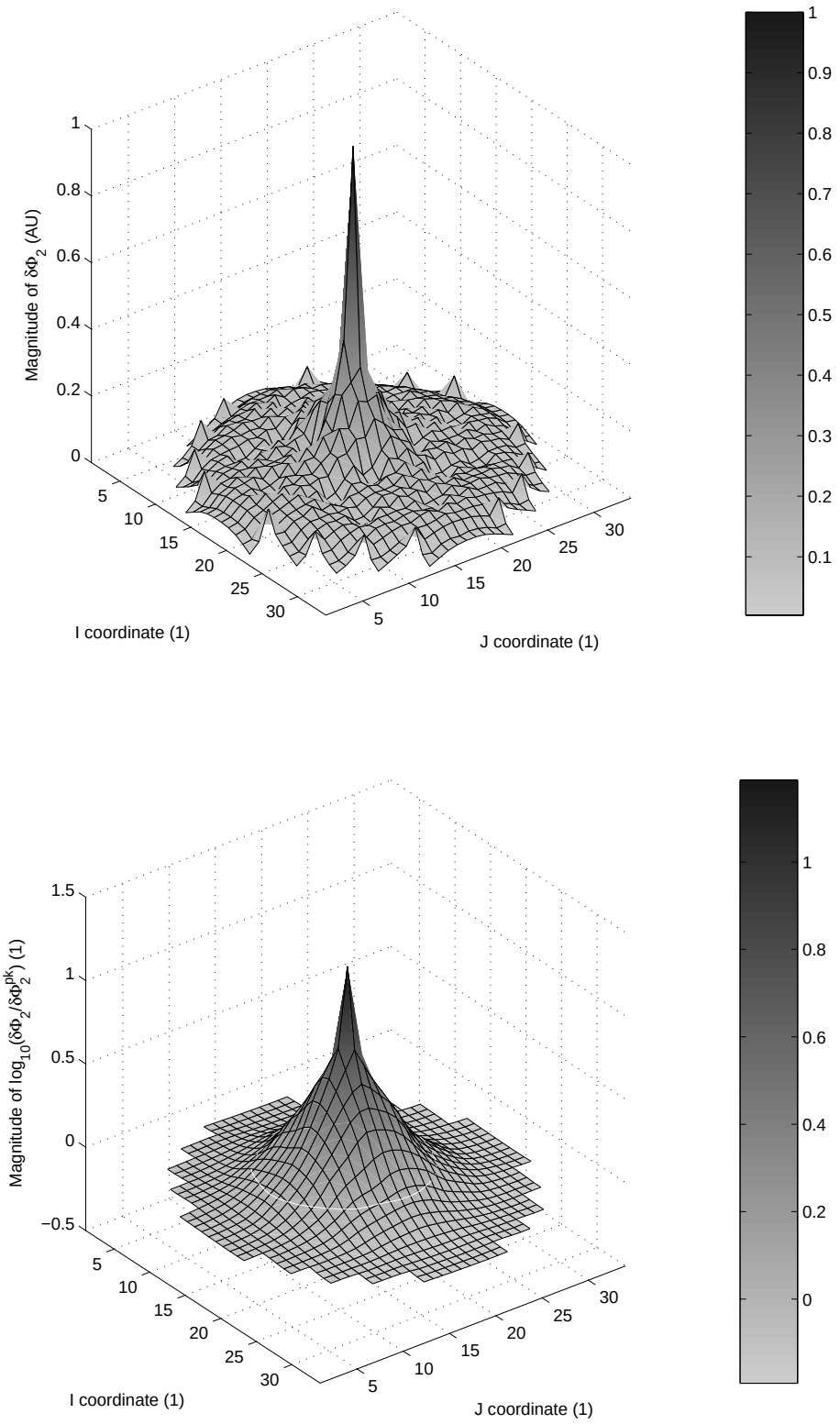

Fig. 4. *Thermal neutron noise induced by a central noise source in a 2-D heterogeneous reactor (in the upper Figure) and the corresponding deviation from point-kinetics (in the lower Figure, where the white line represents agreement with point-kinetics) at a frequency of 1 Hz*

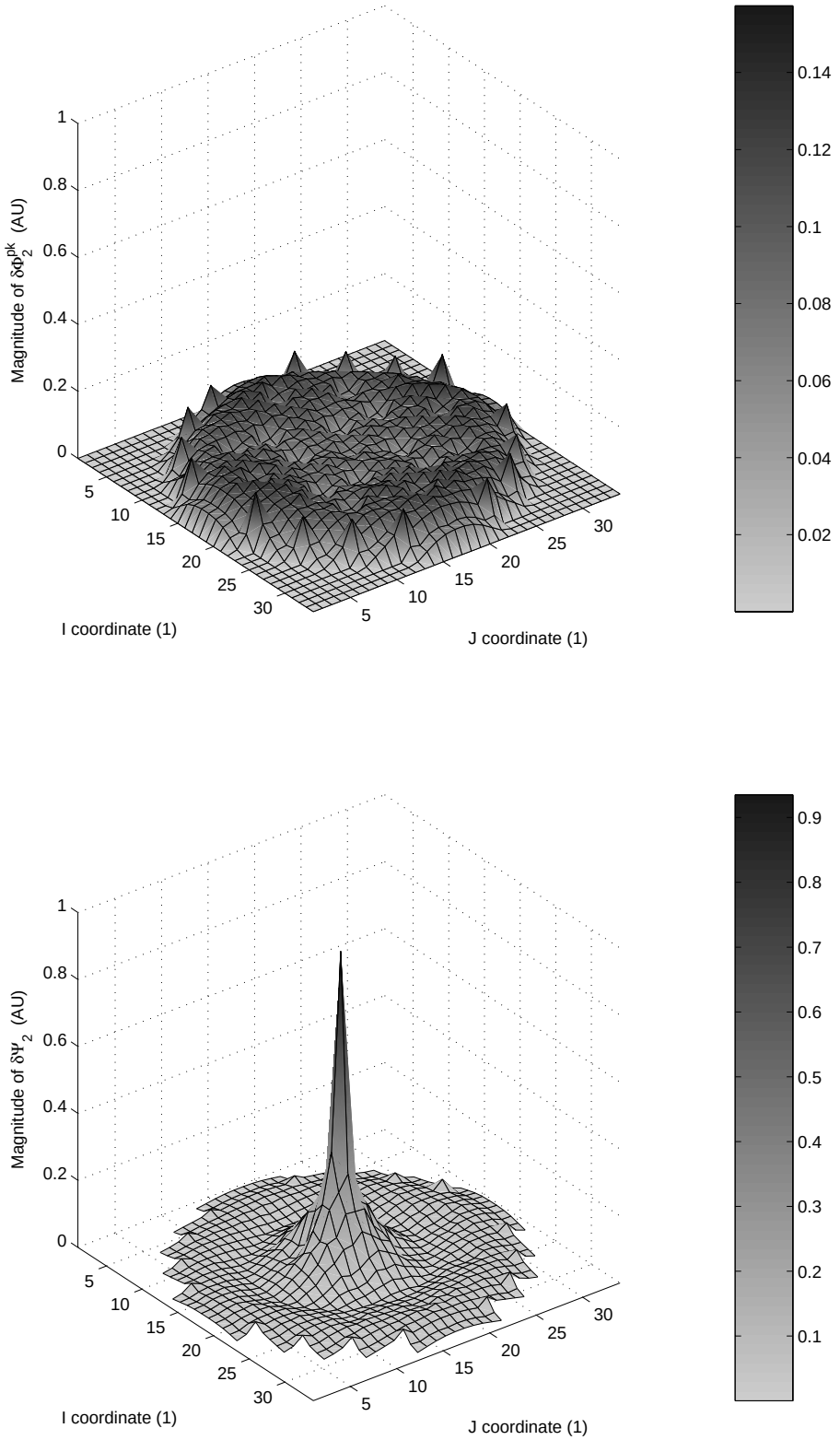

Fig. 5. *The different components of the thermal neutron noise induced by a central noise source in a 2-D heterogeneous reactor at a frequency of 1 Hz*

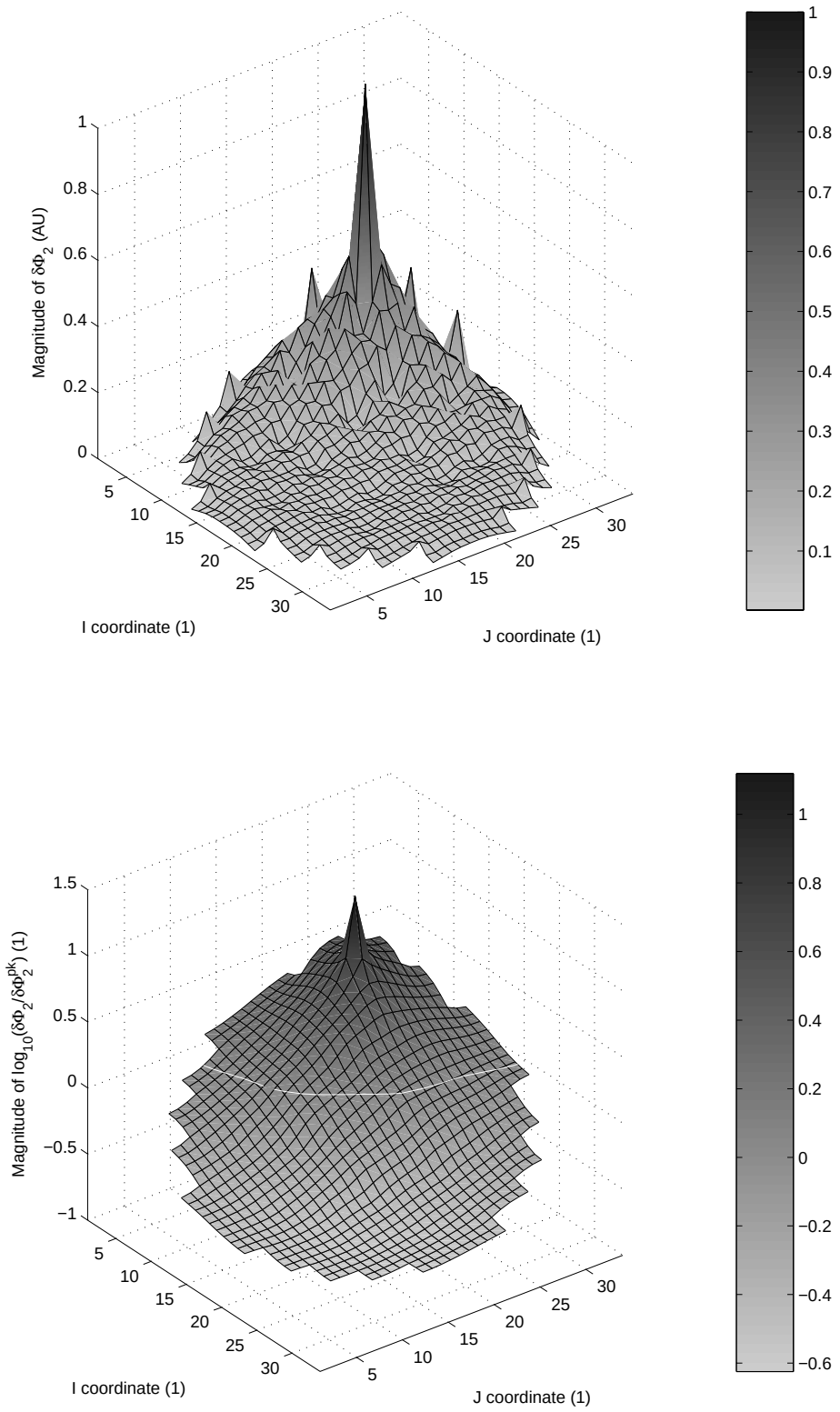

Fig. 6. *Thermal neutron noise induced by a peripheral noise source in a 2-D heterogeneous reactor (in the upper Figure) and the corresponding deviation from point-kinetics (in the lower Figure, where the white line represents agreement with point-kinetics) at a frequency of 1 Hz*

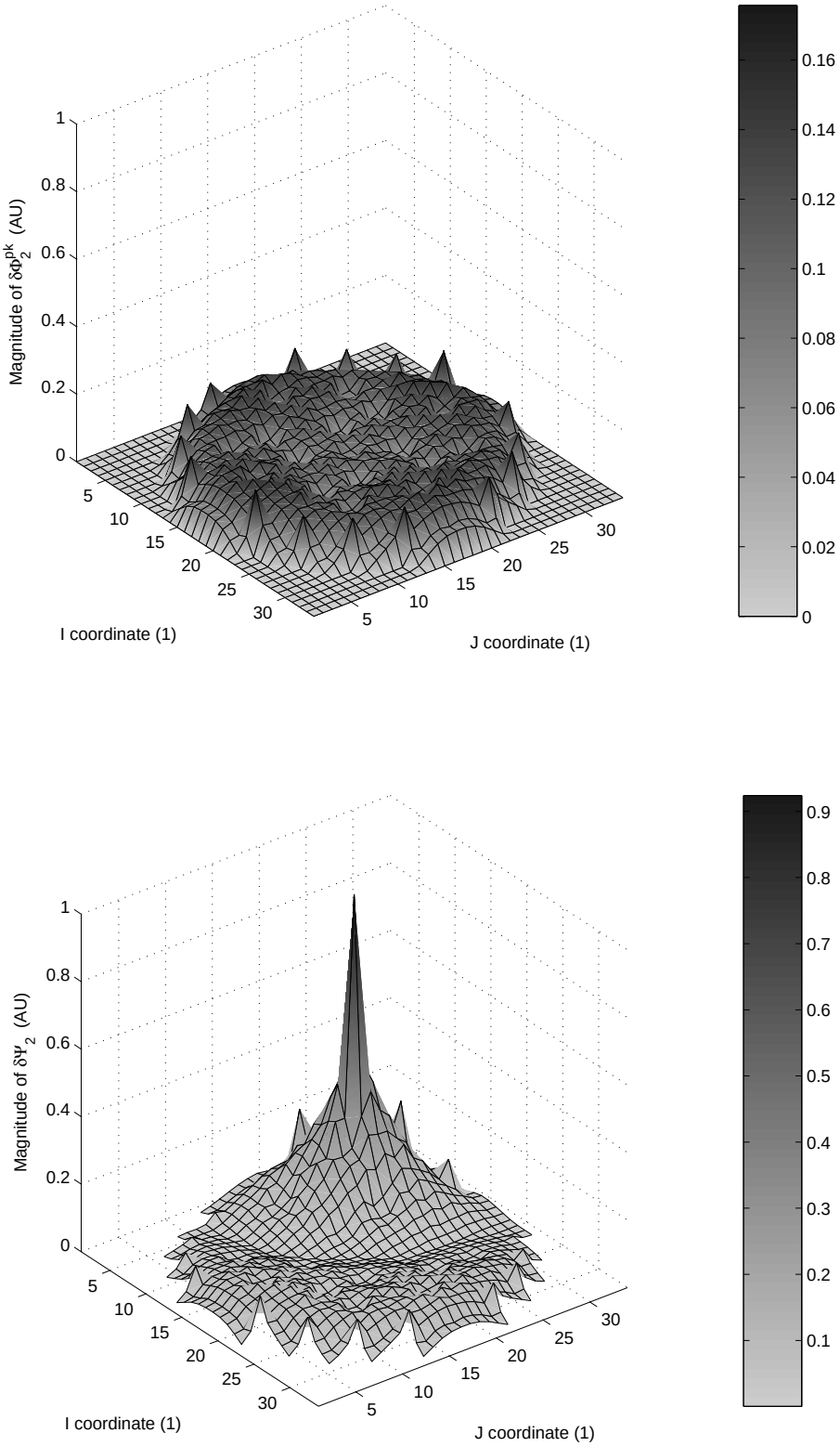

Fig. 7. *The different components of the thermal neutron noise induced by a peripheral noise source in a 2-D heterogeneous reactor at a frequency of 1 Hz*

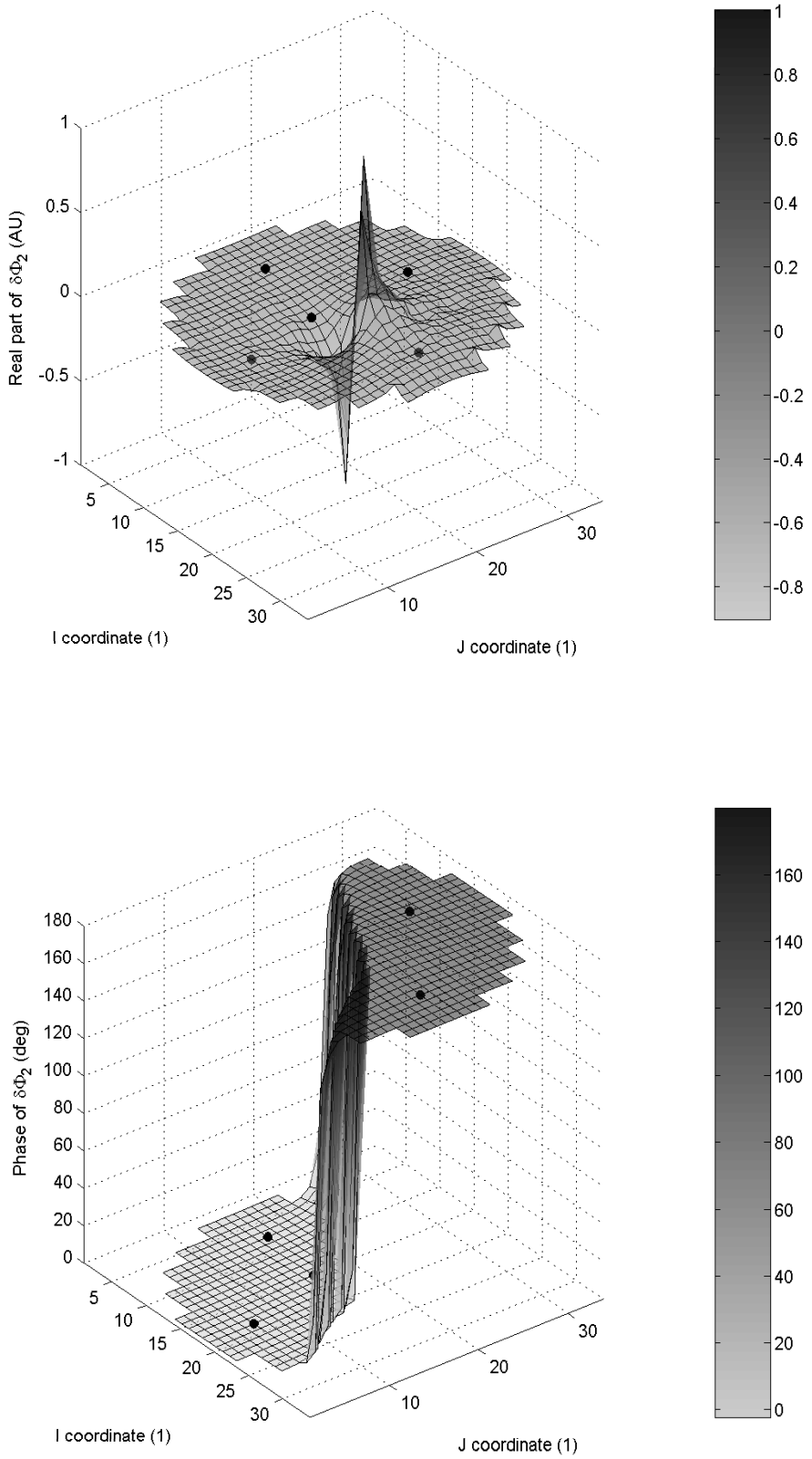

Fig. 8. *Typical thermal neutron noise induced by a vibrating absorber at a frequency of 1 Hz (the black dots represent the location of the neutron detectors)*

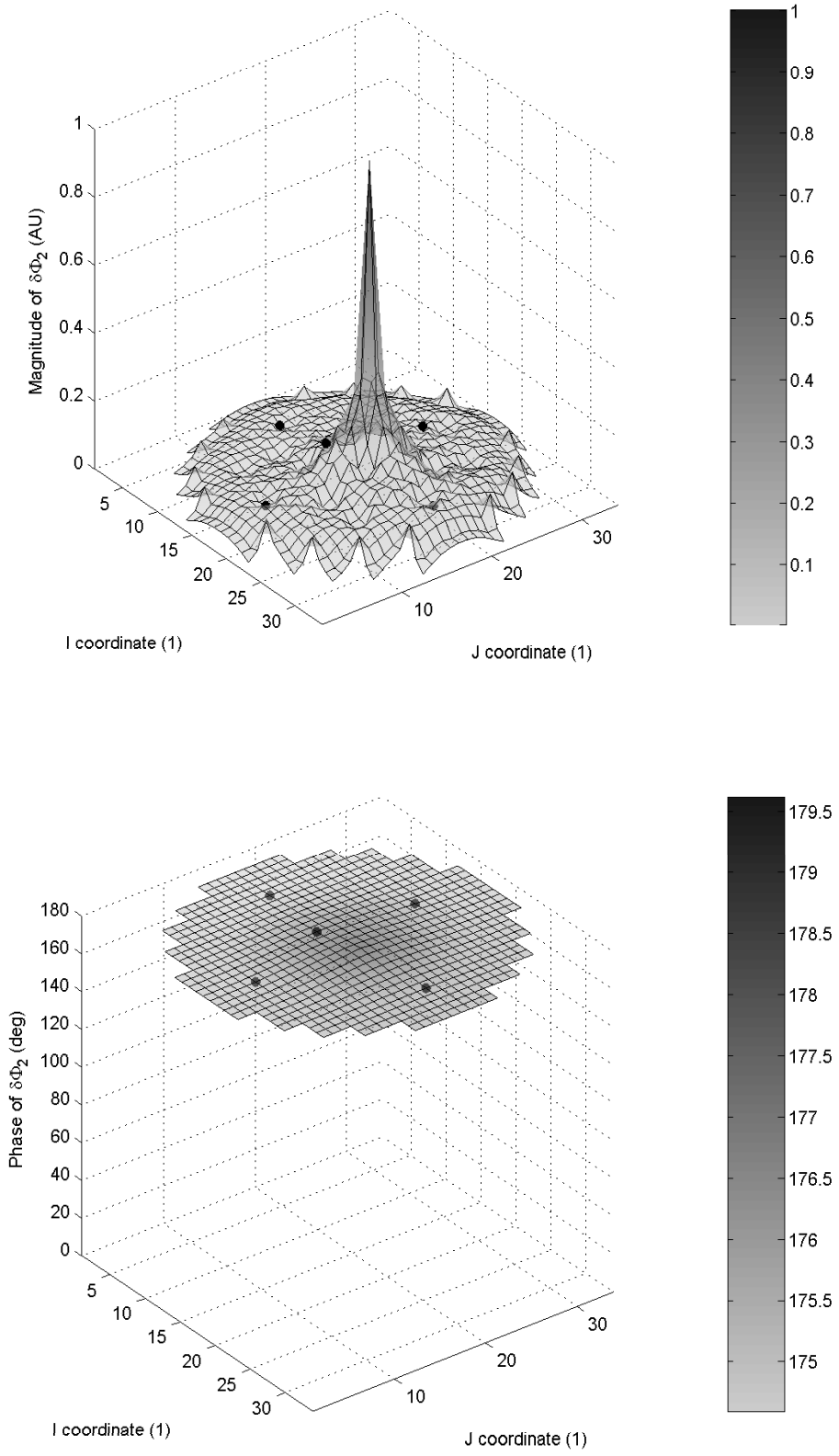

Fig. 9. *Typical thermal neutron noise induced by an absorber of variable strength at a frequency of 1 Hz (the black dots represent the location of the neutron detectors)*

a vibrating absorber, some of the detectors exhibits an in-phase behaviour, whereas some others exhibits an out-of-phase behaviour.

Consequently, the examination of the phase of the induced neutron noise measured at the position of the detectors allows determining the type of localised noise source present in the core. Nevertheless, such an identification is only possible if the actual noise source is located between the detectors. It is obvious that a vibrating absorber located close to the boundary of the core, i.e. on one side of all the detectors, will induce an out-of-phase behaviour that cannot be monitored by the detectors. This is why it is important to choose the detectors in such a way that they cover roughly the entire core.

1.4.2 Unfolding algorithms and results

In the following, different unfolding algorithms are presented and tested. These algorithms will be referred to as the inversion method, the zoning method, and the scanning method in order to facilitate the discussion and the comparisons of the performances of the different unfolding procedures. It is further assumed that a noise source cannot be located in a reflector node.

a) The inversion method

As presented previously, the dynamic simulator solves the discretised form of Eq. (11), so that the Green's function $\overline{G}_{XS}(\boldsymbol{r}, \boldsymbol{r}_P, \omega)$, i.e. the neutron noise at all positions $\boldsymbol{r}$ for a given locations $\boldsymbol{r}_P$ of the noise source, can be determined. The dynamic simulator actually estimates the Green's function for all possible locations $\boldsymbol{r}_P$ of the noise source, so that the neutron noise induced by a spatially-distributed noise source can be easily calculated as:

$$\overline{\delta\phi}(\boldsymbol{r}, \omega) = \int \overline{G}_{XS}(\boldsymbol{r}, \boldsymbol{r}_P, \omega)\delta XS(\boldsymbol{r}_P, \omega)d\boldsymbol{r}_P \tag{49}$$

If the core contains N nodes (for both the fuel and the reflector regions), and if the discretised induced neutron noise $\overline{\delta\phi}(\omega)$ and the discretised noise source $\overline{\delta S}(\omega)$ are both represented by column vectors of size $2N$ (since both vectors have N elements in the fast group and N elements in the thermal group), one can write the following matrix equation:

$$\overline{\delta\phi}(\omega) = \overline{\overline{G}}_{XS}(\omega) \times \overline{\delta XS}(\omega) \tag{50}$$

The matrix $\overline{\overline{G}}_{XS}(\omega)$ is thus of size $2N$x$2N$ and corresponds to what the dynamic simulator estimates. The structure of this matrix is as follows:

$$\overline{\overline{G}}_{XS}(\omega) = \begin{bmatrix} \overline{\overline{G}}_{XS,\,1\to1}(\omega) & \overline{\overline{G}}_{XS,\,2\to1}(\omega) \\ \overline{\overline{G}}_{XS,\,1\to2}(\omega) & \overline{\overline{G}}_{XS,\,2\to2}(\omega) \end{bmatrix} \tag{51}$$

where each submatrix $\overline{\overline{G}}_{XS,\,i\to j}(\omega)$ represents the discretised neutron noise in the energy group j induced by a discretised noise source in the energy group i. Each of these submatrices is of size NxN. Since it is assumed that the neutron detectors are sensitive to the thermal flux only and that the noise source corresponds to a perturbation of the thermal absorption macroscopic cross-section, only $\overline{\overline{G}}_{XS,\,2\to2}(\omega)$ is of interest in this study. In other words, one has:

$$\overline{\delta\phi}_2(\omega) = \overline{\overline{G}}_{XS,\,2\to2}(\omega) \times \overline{\delta XS}_2(\omega) \tag{52}$$

where the index 2 represents the thermal contribution.

It is obvious from this Equation that the discretised thermal noise source $\overline{\delta XS}_2$ can be reconstructed from the full space-dependence of the discretised thermal neutron noise $\overline{\delta\phi}_2(\omega)$ by simply inverting the matrix $\overline{\overline{G}}_{XS,\,2\to2}(\omega)$, i.e.

$$\overline{\delta XS}_2(\omega) \;=\; [\overline{\overline{G}}_{XS,\,2\to2}(\omega)]^{-1} \times \overline{\delta\phi}_2(\omega) \tag{53}$$

Nevertheless, since only a few detectors are available for measuring the induced thermal neutron noise in the reactor, only a few elements of the vector $\overline{\delta\phi}_2(\omega)$ can be determined, which prevents from using $[\overline{\overline{G}}_{XS,\,2\to2}(\omega)]^{-1}$ to reconstruct the noise source.

An alternative way is to interpolate the thermal neutron noise from the detector readings in order to preserve the size of the vector $\overline{\delta\phi}_2(\omega)$. Denoting the interpolated thermal neutron noise as $\overline{\delta\phi}_2^{\,interp}(\omega)$, it can be easily seen from Eq. (53) that only a biased noise source can be reconstructed, i.e.

$$\overline{\delta XS}_2^{\,biased}(\omega) = [\overline{\overline{G}}_{XS,\,2\to2}(\omega)]^{-1} \times \overline{\delta\phi}_2^{\,interp}(\omega) \neq \overline{\delta XS}_2(\omega) \tag{54}$$

The bias in the estimation of the noise source comes from the fact that $\overline{\overline{G}}_{XS,\,2\to2}(\omega)$ was determined for the actual thermal neutron noise $\overline{\delta\phi}_2(\omega)$, whereas Eq. (54) is based on the use of the interpolated thermal neutron noise $\overline{\delta\phi}_2^{\,interp}(\omega)$. In other words, some elements of $\overline{\delta XS}_2^{\,biased}(\omega)$ will be non-zero due to the presence of noise sources and due to the imbalance of $[\overline{\overline{G}}_{XS,\,2\to2}(\omega)]^{-1} \times \overline{\delta\phi}_2^{\,interp}(\omega)$ in some of the nodes, imbalance induced by the spatial interpolation. There is unfortunately no way to determine which of these two possibilities is responsible for a non-zero element of $\overline{\delta XS}_2^{\,biased}(\omega)$, i.e. to determine if the reconstructed noise source in a node is a true or a false one.

Formally, one could nevertheless write that:

$$\begin{aligned}\overline{\delta\phi}_2^{\,interp}(\omega) \;&=\; \overline{\overline{T}} \times \overline{\delta\phi}_2(\omega) \;=\; \overline{\overline{T}} \times \overline{\overline{G}}_{XS,\,2\to2}(\omega) \times \overline{\delta XS}_2(\omega) \\ &=\; \overline{\overline{G}}_{XS,\,2\to2}^{\,interp}(\omega) \times \overline{\delta XS}_2(\omega)\end{aligned} \tag{55}$$

where

$$\overline{\overline{G}}_{XS,\,2\to2}^{\,interp}(\omega) \;=\; \overline{\overline{T}} \times \overline{\overline{G}}_{XS,\,2\to2}(\omega) \tag{56}$$

and T represents the interpolation process. Although T is written here as a matrix, such a matrix does not exist and a modelling tool like MATLAB has to be used to perform the 2-D spatial interpolation. Consequently, on has:

$$\overline{\delta XS}_2(\omega) \;=\; [\overline{\overline{G}}_{XS,\,2\to2}^{\,interp}(\omega)]^{-1} \times \overline{\delta\phi}_2^{\,interp}(\omega) \tag{57}$$

In practice, this means that a new matrix $\overline{\overline{G}}_{XS,\,2\to2}^{\,interp}(\omega)$ has to be calculated. $\overline{\overline{G}}_{XS,\,2\to2}^{\,interp}(\omega)$ corresponds to the interpolated thermal neutron noise induced by discretised thermal noise sources, instead of the actual thermal neutron noise. Therefore, the estimation of such a transfer function has to be performed by a tool similar to the dynamic simulator presented previously. As an illustration of the difference between the $\overline{\overline{G}}_{XS,\,2\to2}(\omega)$ and $\overline{\overline{G}}_{XS,\,2\to2}^{\,interp}(\omega)$ transfer functions, the actual thermal neutron noise and the interpolated thermal neutron noise induced by a local absorber of variable strength are depicted in Fig. 10. The spatial interpolation used for the estimation of the transfer function $\overline{\overline{G}}_{XS,\,2\to2}^{\,interp}(\omega)$ was performed within MATLAB according to a method presented in [31]. This

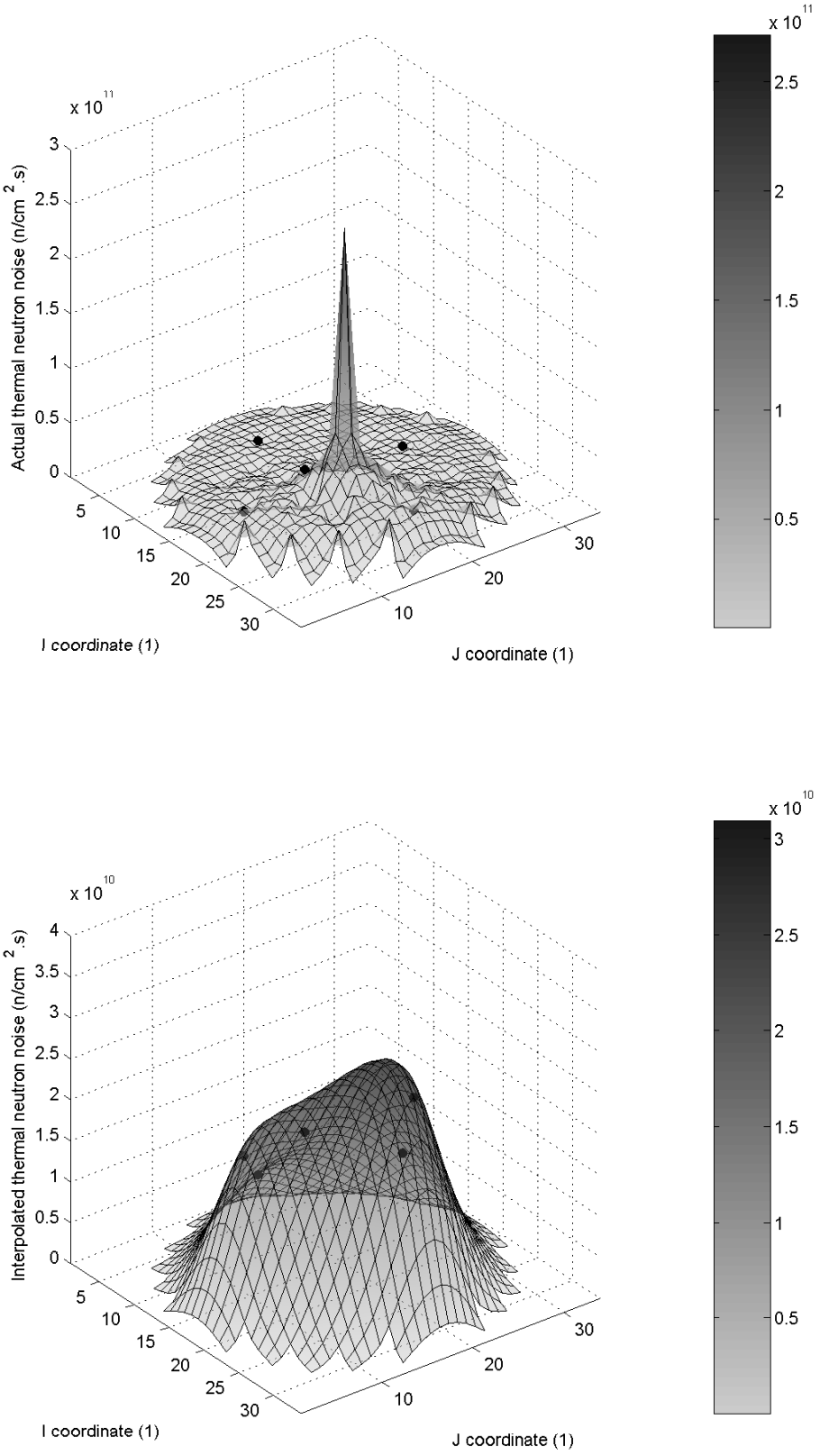

Fig. 10. *Actual and interpolated induced thermal neutron noise at a frequency of 1 Hz (in the upper and lower Figures, respectively); the black dots represent the location of the neutron detectors*

interpolation was furthermore carried out by forcing the interpolated thermal neutron noise to be equal to zero outside the reflector nodes in order to avoid any spatially-divergent neutron noise close to the reactor boundary. As can be seen in this Figure, the interpolation smooths out very much the actual shape of the thermal neutron noise. Thus, different noise sources might induce rather similar interpolated thermal neutron noise, if the noise source is not located close to a detector. It is thus expected that the matrix $\underline{\underline{G}}^{interp}_{XS,\,2\to 2}(\omega)$ is close to a singular matrix. This renders the inversion of this matrix in Eq. (57) very difficult. Several inversion techniques were tried within MATLAB, and it was found that the LU factorization computed by Gaussian elimination was the most efficient technique. By most efficient, it is meant that both Eqs. (55) and (57) are fulfilled with the reconstructed noise source. The results corresponding to the interpolated neutron noise depicted in Fig. 10 are presented in Fig. 11. As can be seen in this Figure, the location of the actual noise source (as well as its

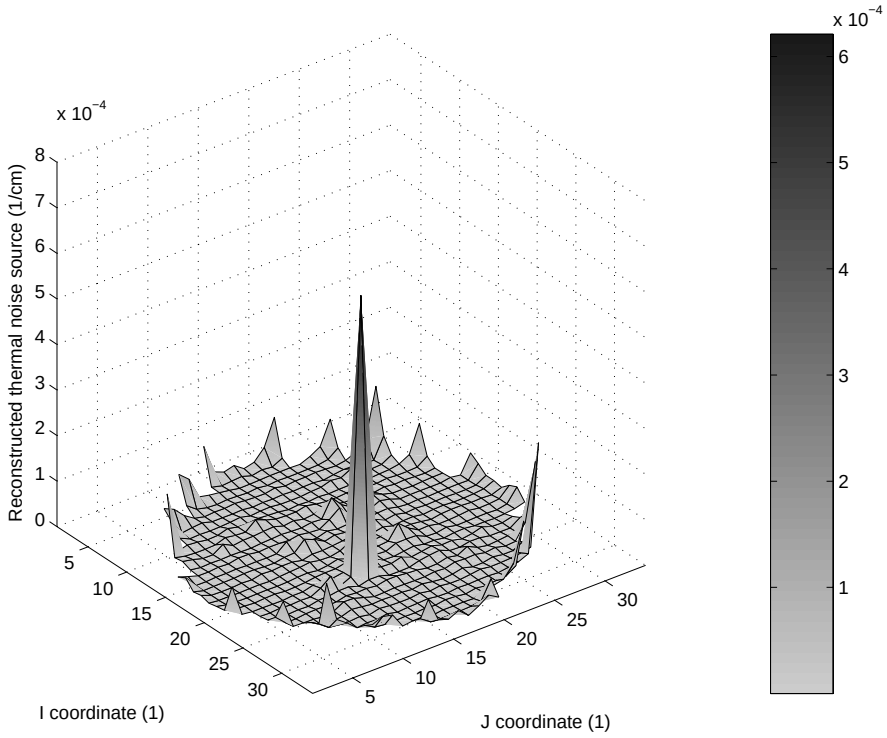

Fig. 11. *Noise source reconstruction based on the inversion method*

amplitude) is correctly reconstructed. It can also be noticed that the reconstructed noise source usually exhibits some peaks close to the reactor boundary. These peaks are in some occurrences bigger than the peak corresponding to the actual noise source and might lead to a misestimation of the location of the noise source. The fact that the reconstructed neutron noise has non negligible contributions close to the reactor boundary might be due to the fact that the interpolated thermal neutron noise is forced to be equal to zero outside the reflector. This induces some inaccuracy of the inversion algorithm for nodes located between the outermost detectors and the reactor boundary. As can be seen in Eq. (12), the perturbation of the macroscopic cross-section is given by the product between the static flux and a Dirac delta function. The inversion algorithm gives somehow a mapping through the core of the probability of having the Dirac delta function, i.e. the location of the perturbation. Therefore, multiplying the result of the inversion algorithm by the interpolated static flux was found to be much more effective in locating the actual noise source, since the peaks observed close to the core boundary are damped by the static flux vanishing at the system

boundary. The inversion method was then tested for all possible locations of the noise source through the core. Before determining the location of the noise source, the result of the inversion algorithm was multiplied by the spatial distribution of the interpolated thermal static flux through the reactor. The interpolation of the thermal static flux was done in the same manner as the one for the thermal neutron noise explained previously. The corresponding results are presented in Fig. 12. Due to the boundary effects, this inversion

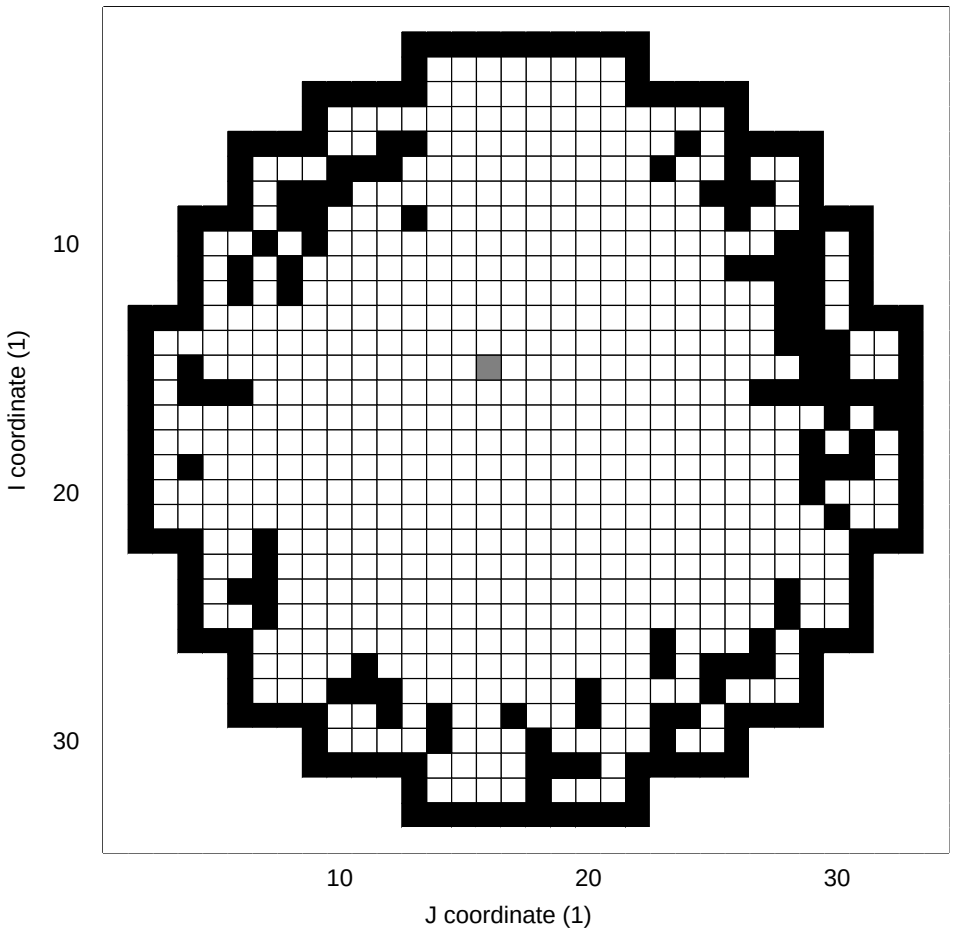

Fig. 12. *Reliability of the inversion method without background noise; the white nodes represent agreement between the reconstructed and the actual noise sources, the gray node a misestimation of less than 3 fuel assemblies, and the black ones a misestimation of more than 3 fuel assemblies (the reflector nodes are plotted in black since it was assumed that a noise source cannot be located in the reflector)*

technique misestimates the actual location of the noise source when positioned close to the reactor boundary. It is also seen that there is one position of the noise source close to the core centre where there is a slight misestimation of the actual location of the noise source. This is due to the spatial configuration chosen for the detectors, i.e. one detector in the neighbourhood of the centre of the core and four other peripheral detectors. When the noise source is located in the vicinity of the core centre, the four peripheral detectors have roughly the same response. This makes the matrix $\underline{\underline{G}}_{XS,\,2\rightarrow 2}^{interp}(\omega)$ badly-scaled and the inversion more difficult in this case. On the average, this technique gives nevertheless rather good results for central noise sources and without background noise. Nevertheless, this unfolding technique is extremely sensitive to numerical errors. Therefore, any background noise to the signals leads to strongly-biased results. As an illustration, the reliability of the inversion technique was determined when adding the same quantity to both the real and the imaginary

parts of all detector signals. More precisely, the background noise was chosen to be 10% of the smallest signal. In such a case, the unfolding technique always points out the same location of the assumed noise source whatever the actual location of the noise source is. It can thus be concluded that the inversion technique becomes rapidly of limited interest when the signals contain any background noise.

b) The zoning method

The inversion method gives sometimes erroneous results since the interpolated neutron noise induced by different noise sources can have rather similar shapes. This means that trying to reconstruct the actual neutron noise from the measured one does not allow recovering a sufficient enough level of detail throughout the core.

This is why another approach, which does not rely on any spatial interpolation, was developed and is presented in the following. If one assumes that the reactor is divided into different zones Z_k, each of these zones having a number of fuel assemblies (i.e. a number of possible locations of the noise source) identical to the number of detectors, one can formally write:

$$\overline{\delta\phi_2}^{meas}(\omega) = \sum_k \overline{\overline{G}}_{XS,\,2\to 2}^{Z_k\to meas}(\omega) \times \overline{\delta XS_2}^{Z_k}(\omega) \tag{58}$$

It can be noticed from this Equation that all the matrices $\overline{\overline{G}}_{XS,\,2\to 2}^{Z_k\to meas}(\omega)$ are square matrices, since the vectors $\overline{\delta\phi_2}^{meas}(\omega)$ and $\overline{\delta XS_2}^{Z_k}(\omega)$ have the same size. In other words, these matrices can be inverted, if there are not badly-scaled. If the fuel assemblies constituting the zone Z_k are chosen not close to each other but rather as far away as possible from each other, the neutron detectors are believed to respond very differently to noise sources located in each of these fuel assemblies respectively. This prevents the matrices $\overline{\overline{G}}_{XS,\,2\to 2}^{Z_k\to meas}(\omega)$ from being badly-scaled. Having the fuel assemblies belonging to a given zone Z_k evenly-distributed throughout the core is probably the easiest way to achieve such a goal. Inverting one of the matrices $\overline{\overline{G}}_{XS,\,2\to 2}^{Z_k\to meas}(\omega)$ for the zone Z_l then allows writing:

$$\left[\overline{\overline{G}}_{XS,\,2\to 2}^{Z_l\to meas}(\omega)\right]^{-1} \times \overline{\delta\phi_2}^{meas}(\omega) \tag{59}$$

$$= \sum_{k\neq l}\left[\overline{\overline{G}}_{XS,\,2\to 2}^{Z_l\to meas}(\omega)\right]^{-1} \times \overline{\overline{G}}_{XS,\,2\to 2}^{Z_k\to meas}(\omega) \times \overline{\delta XS_2}^{Z_k}(\omega) + \overline{\delta XS_2}^{Z_l}(\omega)$$

If the noise source is located in the zone Z_s, Eq. (59) allows writing:

$$\left[\overline{\overline{G}}_{XS,\,2\to 2}^{Z_s\to meas}(\omega)\right]^{-1} \times \overline{\delta\phi_2}^{meas}(\omega) = \overline{\delta XS_2}^{Z_s}(\omega) \tag{60}$$

The use of this Equation provides the vector $\overline{\delta XS_2}^{Z_s}(\omega)$, for which the element corresponding to the actual location of the noise source is much larger than the other elements. In principle, these other elements should be identically equal to zero, but the inversion of the matrix $\left[\overline{\overline{G}}_{XS,\,2\to 2}^{Z_s\to meas}(\omega)\right]$ prevents these elements from being rigorously equal to zero.

If the inversion is carried out with a matrix corresponding to a zone Z_l different from the zone Z_s containing the noise source, Eq. (59) then gives:

$$\left[\overline{\overline{G}}_{XS,\,2\to 2}^{Z_l\to meas}(\omega)\right]^{-1}\times\overline{\delta\phi_2}^{meas}(\omega)\;=\;\left[\overline{\overline{G}}_{XS,\,2\to 2}^{Z_l\to meas}(\omega)\right]^{-1}\times\overline{\overline{G}}_{XS,\,2\to 2}^{Z_s\to meas}(\omega)\times\overline{\delta XS_2}^{Z_s}(\omega) \quad (61)$$

Contrary to the case where the zone Z_l does actually contain the noise source, $\left[\overline{\overline{G}}_{XS,\,2\to 2}^{Z_l\to meas}(\omega)\right]^{-1}\times\overline{\delta\phi_2}^{meas}(\omega)$ does not provide $\overline{\delta XS_2}^{Z_s}(\omega)$, and therefore does not return a vector for which one of the elements is much larger than the others. Rather, Eq. (61) reconstructs a fictitious noise source $\overline{\delta XS_2}^{Z_l,\,fict}(\omega)$ that allows fulfilling Eq. (61) as:

$$\left[\overline{\overline{G}}_{XS,\,2\to 2}^{Z_l\to meas}(\omega)\right]^{-1}\times\overline{\delta\phi_2}^{meas}(\omega)\;=\;\overline{\delta XS_2}^{Z_l,\,fict}(\omega) \quad (62)$$

with

$$\overline{\delta XS_2}^{Z_l,\,fict}(\omega)\;=\;\left[\overline{\overline{G}}_{XS,\,2\to 2}^{Z_l\to meas}(\omega)\right]^{-1}\times\overline{\overline{G}}_{XS,\,2\to 2}^{Z_s\to meas}(\omega)\times\overline{\delta XS_2}^{Z_s}(\omega) \quad (63)$$

Although there is no mathematical proof for it, it is believed that the elements of the vector $\overline{\delta XS_2}^{Z_l,\,fict}(\omega)$ would not be as much different from each other as in the case of $\overline{\delta XS_2}^{Z_s}(\omega)$ since none of the elements of the $\overline{\delta XS_2}^{Z_l,\,fict}(\omega)$ allows reconstructing the actual measured thermal neutron noise.

In other words, each matrix $\overline{\overline{G}}_{XS,\,2\to 2}^{Z_k\to meas}(\omega)$ has to be multiplied by $\overline{\delta\phi_2}^{meas}(\omega)$. The result of this multiplication should provide one out of two typical vectors, depending on the fact that the zone Z_k contains a noise source or not. If this zone contains a noise source, one of the elements of this vector should be much larger than the others. If this zone does not contain a noise source, no element of this vector should be extremely different from the others. It is difficult to estimate how much the elements in such a case might be different from each other. Only numerical tests can determine the applicability of this method, and this is the object of the present investigation. It can be easily understood that it is the comparison of the elements of these vectors with each other that matters. One therefore constructs the different zones Z_k in such a way that they all contain a common node. For the sake of simplicity, this node is chosen in the reflector, where it is assumed that no noise source can exist. When comparing the elements of all these vectors, the element having the highest magnitude should in principle correspond to the actual location of the noise source. Since the reconstructed noise source contains fictitious noise sources, it needs to be rescaled to match the actual amplitude of the actual neutron noise. The results corresponding to the interpolated neutron noise depicted in Fig. 10 are presented in Fig. 13. It has to be emphasized that contrary to the inversion method, only the neutron noise measured at the detector location is used in the zoning method. It can be noticed that the amplitude of the noise source at the actual location of the noise source is so large compared to the other possible locations that it can be claimed that the noise source is correctly reconstructed. The inversion method was then tested for all possible locations of the noise source through the core. The corresponding results are presented in Fig. 14. It can be seen that this unfolding algorithm is particularly effective. As for the inversion algorithm, there is a couple of positions of the noise source close to the core centre where there is a slight misestimation of the actual location of the noise source. This is due to the spatial configuration chosen for the detectors, i.e. one detector in the neighbourhood of the centre of the core and four other peripheral detectors. When the noise source is located in the vicinity of the core centre, the four peripheral detectors have roughly the same response. This renders the situation more difficult for the unfolding. As for the inversion technique, the reliability of the zoning technique was also determined when adding the same quantity to both the real and the imaginary parts of all detector signals. This background noise was chosen to be 10% of the

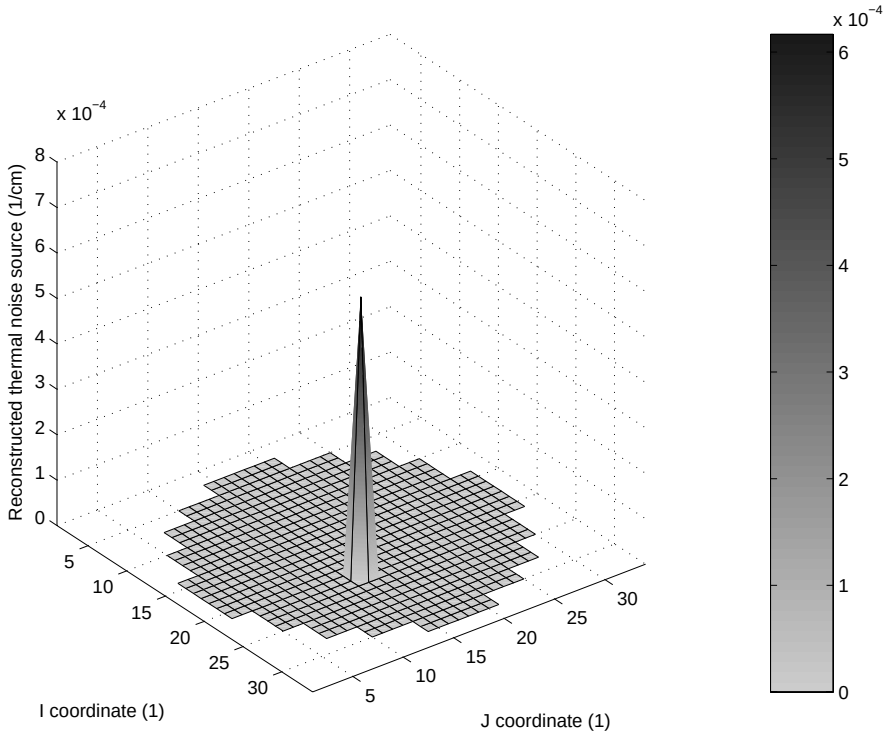

Fig. 13. *Noise source reconstruction based on the zoning method*

smallest signal. As for the inversion method, the chances of localising the actual noise source greatly improves when the noise source is multiplied by the interpolated thermal static flux. The corresponding results are presented in Fig. 15, where the legend is different from the one used in Fig. 14. It can be noticed that the zoning technique becomes much less reliable than without any background noise. Nevertheless, this unfolding technique is much more robust than the inversion technique to the contamination of the detector signals by background noise, and is able to point out a region of the reactor where the actual noise source is likely to be located.

c) The scanning method

A third method that can be used for localising absorbers of variable strength is based on the comparisons between the detector readings and their calculated response for all the possible locations of the noise source throughout the core. The noise source is correctly located when there is agreement between the calculated and the measured neutron noise. This method was originally developed by [32] where the authors assumed that the reactor was homogeneous in order to be able to calculate analytically the Green's function in the 1-group diffusion approximation. The same algorithm was later on extended to heterogeneous systems in the 2-group diffusion approximation [19], [33]. Both investigations were successful in determining the location of an unseated fuel assembly in the Swedish Forsmark-1 BWR. The purpose of the present investigation is to compare the performance of this unfolding technique to the previous algorithms, i.e. to the inversion and zoning algorithms.

The starting point is to write that the thermal flux noise in a given node (I, J) induced by a noise source located in (I_0, J_0) can be expressed from Eq. (52) as:

$$\delta\phi_2(I, J, \omega) = G_{XS,\,2\to 2}(I_0, J_0 \to I, J, \omega) \times \delta XS_2(I_0, J_0, \omega) \tag{64}$$

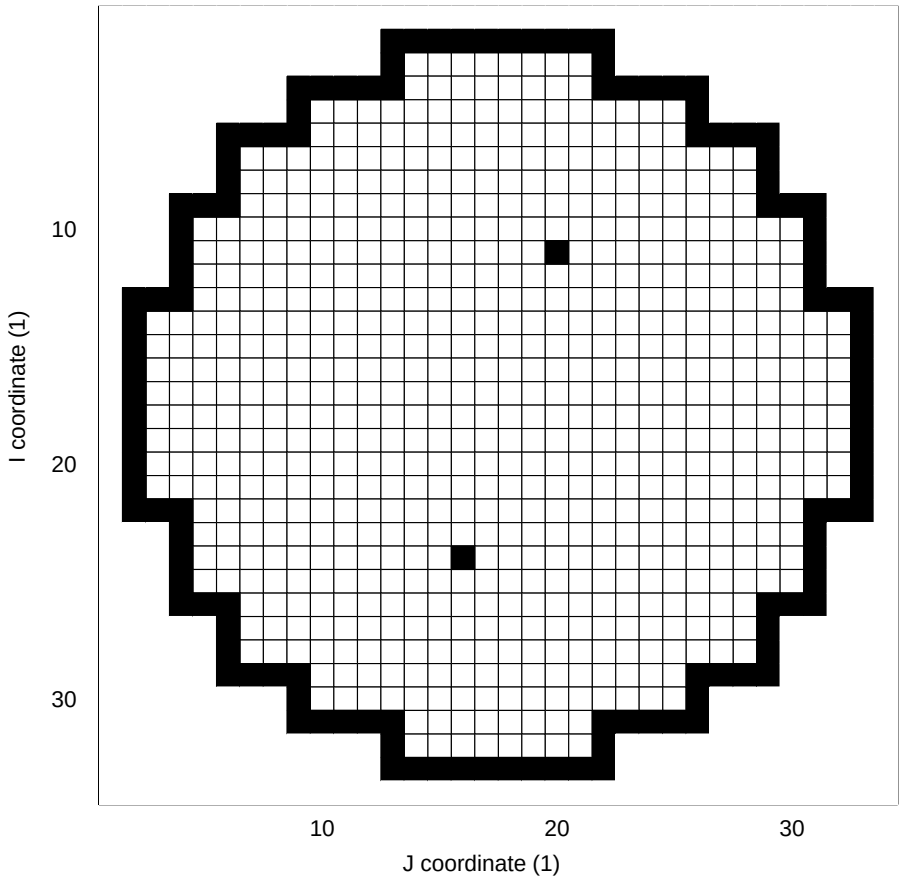

Fig. 14. *Reliability of the zoning method without background noise; the white nodes represent agreement between the reconstructed and the actual noise sources, and the black ones a misestimation of more than 3 fuel assemblies (the reflector nodes are plotted in black since it was assumed that a noise source cannot be located in the reflector)*

Trying to use this expression to match the detector readings is rather difficult since both the location of the noise source and its strength are unknown. If one has access to two detectors *A* and *B*, taking the ratio between the neutron noise at these two locations allows eliminating the noise source strength:

$$\frac{\delta\phi_2(I_A, J_A, \omega)}{\delta\phi_2(I_B, J_B, \omega)} = \frac{G_{XS,\,2\to 2}(I_0, J_0 \to I_A, J_A, \omega)}{G_{XS,\,2\to 2}(I_0, J_0 \to I_B, J_B, \omega)} \tag{65}$$

The scanning algorithm thus consists of trying to minimize the following function:

$$\Delta(I, J) = \sum_{A,\,B} \Delta_{A,\,B}(I, J) \tag{66}$$

with

$$\Delta_{A,\,B}(I, J) = \left| \frac{\delta\phi_2^{meas}(I_A, J_A, \omega)}{\delta\phi_2^{meas}(I_B, J_B, \omega)} - \frac{G_{XS,\,2\to 2}(I, J \to I_A, J_A, \omega)}{G_{XS,\,2\to 2}(I, J \to I_B, J_B, \omega)} \right| \tag{67}$$

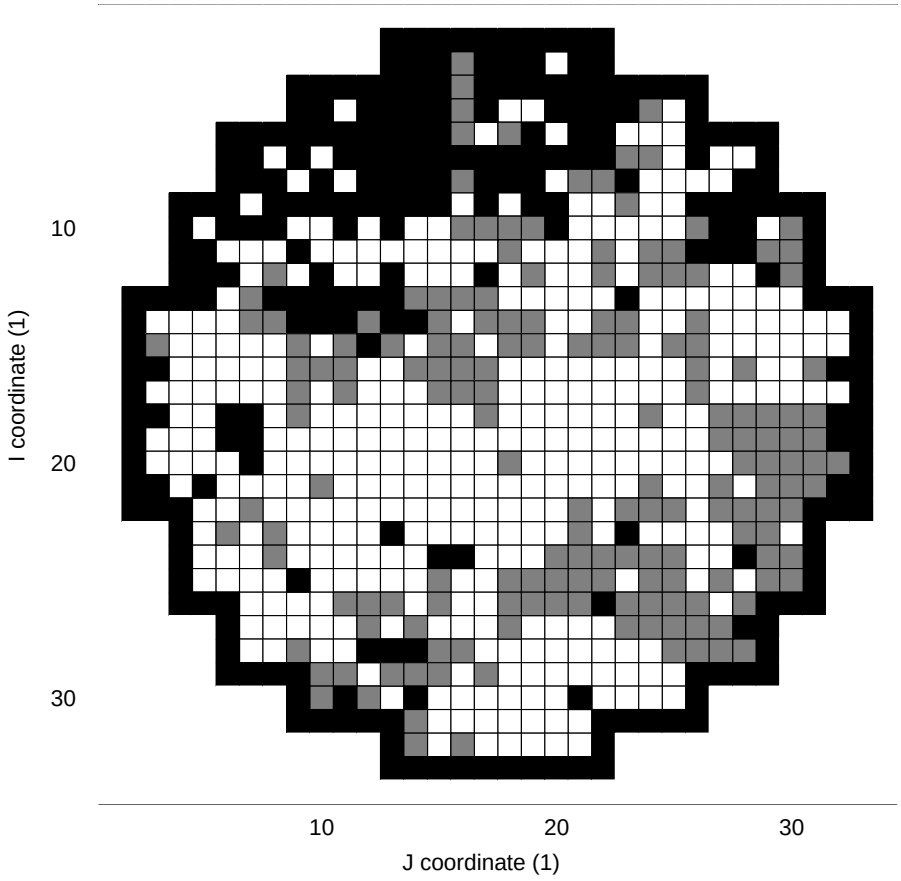

Fig. 15. *Reliability of the zoning method with background noise; the white nodes represent a misestimation of the reconstructed noise source of less than 5 fuel assemblies, the gray nodes a misestimation of more than 5 fuel assemblies but less than 10 fuel assemblies, and the black ones a misestimation of more than 10 fuel assemblies (the reflector nodes are represented in black since it was assumed that a noise source cannot be located in the reflector)*

taken for every combination of detectors (*A*, *B*). The first term on the r.h.s. of this Equation represent the ratio of the neutron noise measured at the location of the detectors, and the second term represent the ratio of the neutron noise calculated at the location of the detectors for a noise source located in (*I*, *J*). Although Eq. (67) has to be evaluated for every combination of detectors when analysing actual measurements, the same detector was used as *B* in Eq. (67) throughout this study, since using all the combinations of detectors for simulated signals would only provide redundant information. The location of the noise source is assumed to correspond to a global/local minimum of the function given by Eqs. (66) and (67). Since this algorithm only determines the location of the noise source, its amplitude has to be reconstructed by simply scaling the calculated induced neutron noise to the measured one. The results corresponding to the interpolated neutron noise depicted in Fig. 10 are presented in Fig. 16. As for the zoning method, only the neutron noise measured at the detector location is actually needed. As can be seen in this Figure, the noise source is correctly determined. The scanning method was then tested for all possible locations of the noise source through the core. It was noticed that this unfolding algorithm was able to locate correctly any noise source in the core, if there is no background noise. This algorithm is thus much more reliable and robust than the inversion (and to a lesser extent zoning)

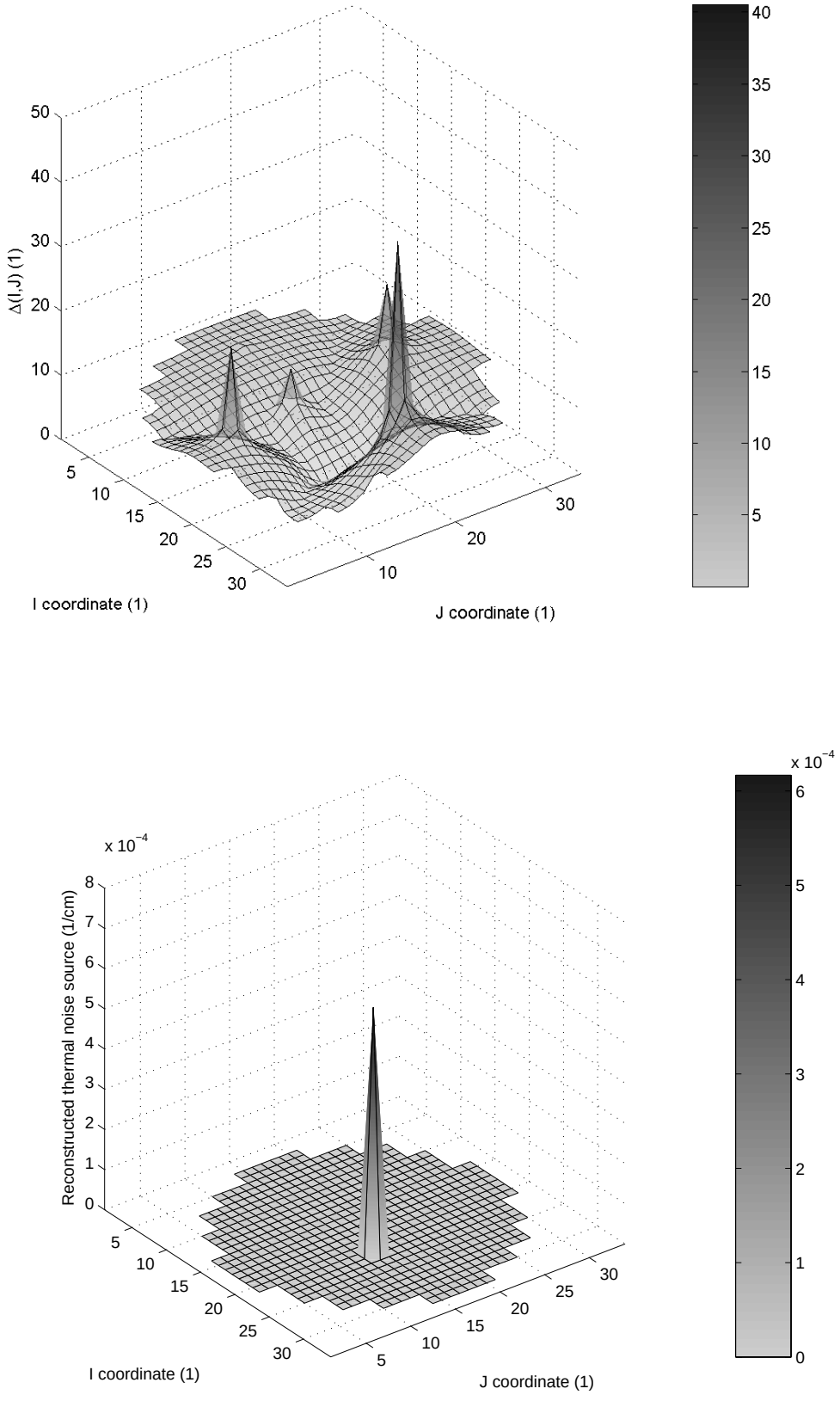

Fig. 16. *Noise source reconstruction based on the scanning method (with the Δ function given in the upper figure, and the reconstructed noise source in the lower figure)*

algorithm(s). This can be explained by the fact that no matrix inversion is needed for performing the unfolding, whereas the inversion (and to a lesser extent zoning) algorithm(s) rely on the inversion of a matrix that might be badly-scaled in some occurrences. A drawback of the scanning algorithm lies with the fact that every possible location of the noise source has to be tested, in order to be able to construct the function given by Eqs. (66) and (67). This requires much more CPU time than for the two other unfolding methods. Furthermore, when analysing an actual measurement, every combination of detectors has to be used for the evaluation of Eq. (67). This will further increase the calculational time necessary for applying this algorithm. As before, the reliability of the scanning technique was also determined when adding the same quantity to both the real and the imaginary parts of all detector signals. This background noise was chosen to be 10% of the smallest signal. The corresponding results are presented in Fig. 17. It can be noticed that the scanning

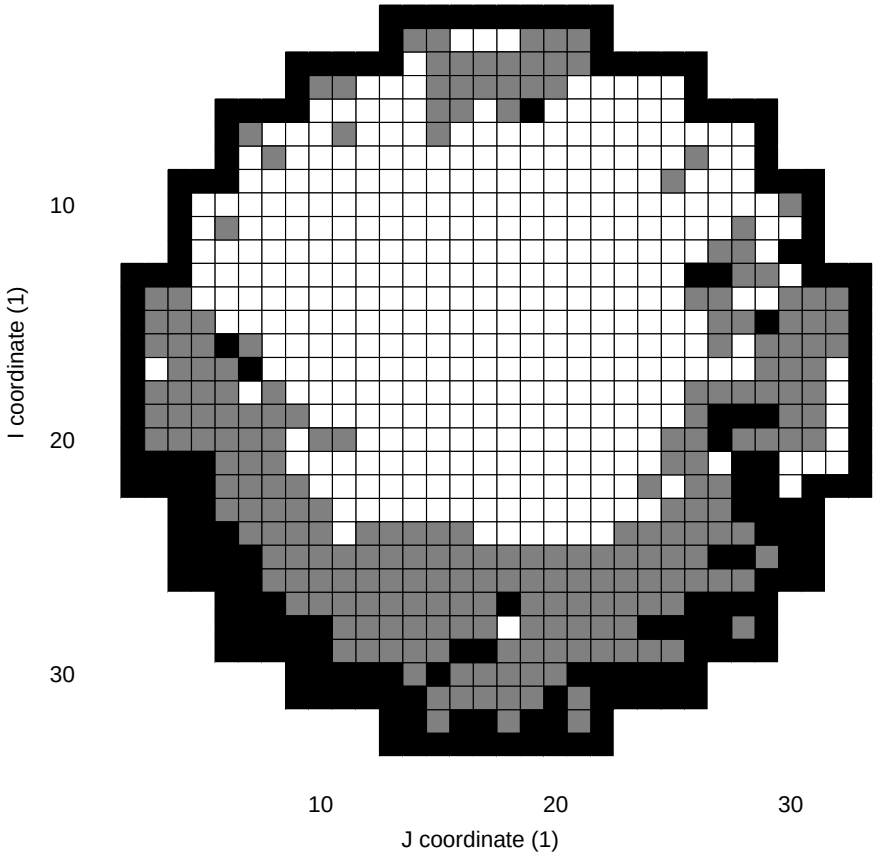

Fig. 17. *Reliability of the scanning method with background noise; the white nodes depict an agreement between the reconstructed and the actual noise sources, the gray nodes a misestimation of less than 3 fuel assemblies, and the black ones a misestimation of more than 3 fuel assemblies (the reflector nodes are represented in black since it was assumed that a noise source cannot be located in the reflector)*

technique remains reliable when the signals contain background noise. Compared to the zoning algorithm, this unfolding technique is much more robust to the contamination of the detector signals by background noise.

1.5 Conclusions and discussion

The three unfolding techniques, i.e. the inversion method, the zoning method, and the scanning method, all allow reconstructing, to some extent, a localised absorber of variable strength, after its proper identification in the reactor. The success of this reconstruction lies with the fact that the induced neutron noise deviates significantly enough from point-kinetics. The space-dependence of the induced neutron noise measured at as few as five evenly-distributed positions in the core is therefore representative of the location of the noise source.

When comparing these different techniques, it can be noticed that the technique relying on the direct inversion of the reactor transfer function, i.e. the inversion method, leads to biased results in some occurrences. This can be explained by the badly-scaled character of the matrix that has to be inverted in this technique, since different locations of the noise source might induce a rather similar neutron noise at the position of the detectors. This technique becomes completely unreliable when any level of background noise is present. A modified inversion technique, i.e. the zoning method, was thus developed in order to prevent the different matrices from being badly-scaled before inversion. This new technique was demonstrated to give reliable results in most cases without requiring much CPU time. When adding background noise, the reliability of this technique deteriorates significantly. Nevertheless, the zoning algorithm is still able to indicate regions of the core, where the actual noise source is likely to be located. On the contrary, the scanning method is very robust and quite insensitive to the contamination of the detector signals by background noise, since no matrix inversion is required. Rather, the location of the noise source is estimated from the comparison between the measured neutron noise and the calculated induced neutron noise for all possible pairs of detectors and for every possible location of the noise source. The required CPU time is consequently much larger than the one necessary for applying the inversion and zoning techniques. It can also be anticipated that the inversion and zoning algorithms would become more reliable when the number of available detectors increase, whereas the scanning algorithm would be too much CPU-demanding.

When analysing actual measurement data, the zoning and scanning techniques could therefore be used. Furthermore, this would bring some redundant information about the location of the noise source, and would appreciably improve the confidence in the obtained results. Further developments of these techniques are nevertheless required. For example, the algorithms presented in this paper all rely on the Fourier-transform of the time-signals. In practice, the use of the Auto-Power Spectral Densities (APSDs) and Cross-Power Spectral Densities (CPSDs) allows removing the uncorrelated noise from the detector signals. Although the Wiener-Khinchin theorem can be used to express APSDs and CPSDs from the Fourier-transform of the signals, the previous algorithms have to be further developed since many pairs of detectors can be used for evaluating the CPSDs. Finally, a similar investigation for vibrating absorbers would also be of interest.

Section 2

Development of the Feynman-alpha method for pulsed sources

2.1 Introduction

The theory of the Feynman-alpha method with pulsed sources became interesting recently in connection with the future accelerator-driven systems (ADS). Current on-going experimental pilot projects with the aim of studying ADS basics use pulsed neutron generators as a source [34]. Even the spallation sources, planned to be used in a future full-scale ADS facility, might be operated in a pulsed mode, for technical reasons. Although there are several competing methods to be used in pulsed source experiments to determine reactivity, most notably the area-ratio method, the Feynman- or Rossi-alpha methods have always been considered as interesting complements. Hence their applicability and performance has been a matter of current interest.

In line with the above, formulas for the Feynman-alpha method with pulsed sources have been elaborated in the past few years ([35]-[37]). In this respect it is customary to distinguish between deterministic and stochastic data evaluation techniques. These are also referred to as the "deterministic (stochastic) pulsing" or "deterministic (stochastic) Feynman method". They only differ in whether the counting gate opens in a synchronised manner with the pulsing, or randomly. Since the time-to-digital conversion is nowadays made with a high resolution, a measurement consists of the registration of the arrival time of each detector count, such that the neutron pulse trigger is also recorded. Hence a measurement can be evaluated by both the deterministic or the stochastic method.

First the deterministic Feynman-alpha formula was derived by solving the corresponding equations for each pulse in a piecewise manner [35]. This method was clumsy in the sense that its extension to more complicated (and hence realistic) pulse shapes was not feasible. The stochastic pulsing was then solved with a much more powerful method, using Laplace transform and complex function techniques [36]. This technique was then applied also to the deterministic case [37], but its potential was not fully utilized, and the first results were only restricted to the reconstruction of the previous quantitative results of Ref. [35].

In this report the solution based on the Laplace transform technique is developed fully by evaluating some integrals explicitly in an effective way. This way, we were able to give compact and robust solutions. One particular advantage is the ease with which various pulse shapes can be treated with very little extra effort. Hence, in addition to the square pulses treated earlier, we have also considered Gaussian pulse shapes, which correspond better to the pulse shape of neutron generators [34]. A quantitative analysis of the Feynman-alpha curves, as functions of the pulse width, frequency and shape is performed, and the possibility of unfolding the prompt neutron time constant from a simulated measurement with the use of the formulas is investigated. More details can be found in some already published reports [39] and in some coming publications.

2.2 General theory

The Feynman-alpha method is based on the measurement of the detector counts $\tilde{Z}(T)$ during a measurement time period T in a stationary system driven with a source *S*. Both the source emission, the diffusion and multiplication of the neutrons in the medium, as well as

the detection process, are subject to random fluctuations. The probability of emission of a source neutron during time t is given as Sdt. The condition of stationarity requires that the measurement is made a long time after that the source was switched on, such that all transients after the switch-on have decayed. With a repeated measurement of the random variable $\tilde{Z}$, its mean $\langle \tilde{Z} \rangle \equiv \tilde{Z}$ and variance $\sigma_Z^2(T)$ can be determined. With a repetition of the measurement for various measurement time lengths, the dependence of the relative variance, or the variance-to-mean $\sigma_Z^2(T)/\tilde{Z}$ (Feynman-alpha function) can be determined. In practice, it is more customary to use the deviation of the relative variance from unity, which is called the Feynman Y-function:

$$Y(T) \equiv \frac{\sigma_{\tilde{Z}}^2(T)}{\tilde{Z}(T)} - 1 = \frac{\tilde{\mu}_Z(T)}{\tilde{Z}(T)} \tag{68}$$

where

$$\tilde{\mu}_Z(T) \equiv \sigma_{\tilde{Z}}^2(T) - \tilde{Z}(T) \tag{69}$$

is called the modified variance. The advantage of introducing the modified variance is the convenience that one can derive equations for it directly.

The mean and the variance of the detector counts can be calculated from a master equation, i.e. from a probability balance equation. Usually, it is more advantageous to use the so-called backward master equation, and we shall use this method here. The quantities that will appear in the derivation are thus as follows.

$$P(N, Z, t) \tag{70}$$

is the probability of finding N neutrons at t and Z counts in the time interval $(t - T, t)$, due to one neutron starting the process at $t = 0$. One also introduces the probability generating function of P as

$$G(x, z, t) \equiv \sum_N \sum_Z x^N z^Z P(N, Z, t) \tag{71}$$

If a master equation for the generating function G is obtained, equations for the various moments can be obtained by differentiating G w.r.t. x or z. Such a master equation was derived a long time back in the theory of neutron fluctuations in nuclear reactors. For later reference, we only quote the two first-moment quantities that will be used in later parts of the paper in the calculations. The expected number of neutrons at time *t* is given by

$$N(t) = e^{-\alpha t} \tag{72}$$

where α is the prompt neutron time constant, given by $\alpha = -\rho/\Lambda$. Here ρ is the subcritical reactivity (to be determined in the measurement) and Λ the prompt neutron generation time. Both ρ and Λ can be expressed by nuclear physics parameters such as cross sections and neutron speed, and are known in a calculation.

The second quantity we shall need is the expected number of counts, which is given as

$$Z(t, T) = \lambda_d \int_0^t N(t - t')\Delta(t', T)dt' \tag{73}$$

where

$$\Delta(t, T) = \begin{cases} 1; & 0 \le t \le T \\ 0; & t > T. \end{cases} \tag{74}$$

From Eqs. (72)-(74) it readily follows that

$$Z(t, T) = \lambda_d \int_0^t \Delta(t', T) N(t - t') dt' = \begin{cases} \frac{\lambda_d}{\alpha}(1 - e^{-\alpha t}); & 0 \le t \le T \\ \frac{\lambda_d}{\alpha} e^{-\alpha t}(e^{\alpha T} - 1); & t > T. \end{cases} \tag{75}$$

In a similar manner,

$$\tilde{P}(N, Z, t|t_0) \tag{76}$$

denotes the probability of finding N neutrons at t and Z counts in the time interval $(0, t)$, due to a source being switched on at $t = t_0$. As it is usual in the literature, all distributions and moments, corresponding to the source-induced case, will be denoted by a tilde. The generating function of $\tilde{P}$ is defined as

$$\tilde{G}(x, z, t|t_0) = \sum_N \sum_Z x^N z^Z \tilde{P}(N, Z, t|t_0) \tag{77}$$

As it will be seen in the next subsection, one can derive a direct relationship between G and $\tilde{G}$ such that the latter is given as an exponential integral over the former. Calculation of the moments of the source-induced distribution requires in general the calculation of multiple nested integrals over certain functions of the various moments of the single-particle induced distribution.

2.3 Calculation of the variance-to-mean for deterministically pulsed sources

As mentioned earlier, the novelty of the Feynman-alpha method with a pulsed source consists of the time dependence of the source. Some characteristic properties follow directly from the fact that the source consists of a train of pulses, independently of the form of the pulses. These will be first investigated here. For the sake of concreteness, whenever explicit formulae are necessary, square pulses will be assumed. The case of Gaussian pulses will be treated in Subsection (2.3.5).

2.3.1 The source and its Laplace transform for square pulses

The time-dependent neutron source is represented by a sequence of square functions:

$$S(t) = S_0 \sum_0^\infty [H(t - nT_0) - H(t - nT_0 - W)] \tag{78}$$

where H is Heaviside's step function, T_0 the pulse period, and W the pulse width. In Fig. 18 the function is plotted.

The Laplace transform of the source is given by:

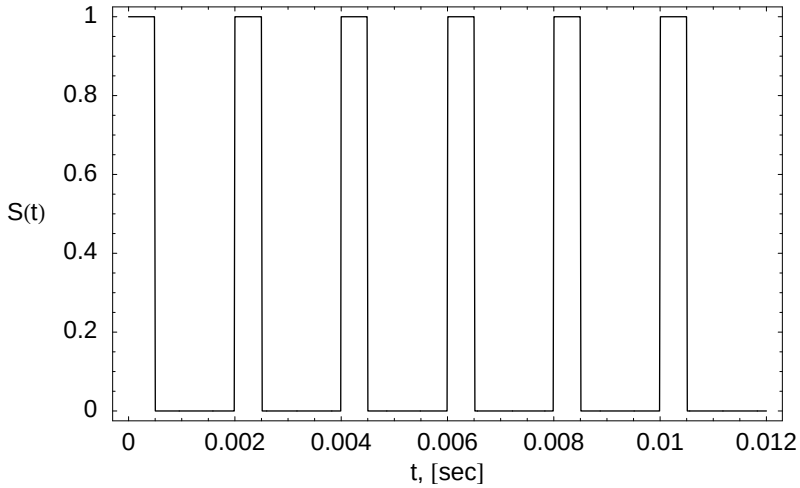

Fig. 18. *The source function S(t), numerical values are found in Table II on page 54.*

$$S(s) = \int_0^\infty e^{-st}S(t)dt = \sum_0^\infty (e^{-sT_0})^n S_0 \int_0^W e^{-st}dt = \frac{S_0(1-e^{-sW})}{s(1-e^{-sT_0})}; \quad Re\{s\} > 0. \tag{79}$$

Eq. (79) shows that the singularities of $S(s)$ are determined by the zeros of the denominator, which arise from the periodicity of the pulse train.

2.3.2 Calculation of the source induced neutron number (square pulses)

We know from earlier calculations that the Bartlett-formula, i.e the relationship between the generating functions of the source induced and single-particle induced distributions, for the case of a time-dependent source reads as

$$\tilde{G}(x, z, t) = \exp\left\{ \int_0^t S(t')G[(x, z, t-t') - 1]dt' \right\}. \tag{80}$$

From Eq. (80) we obtain that the source induced neutron number, $\tilde{N}(t)$ is given by

$$\tilde{N}(t) = \left. \frac{\partial \tilde{G}(x, z, t)}{\partial x} \right|_{x = z = 1} = \int_0^t S(t')N(t-t')dt' \tag{81}$$

and the source induced detector count, $\tilde{Z}(t, T)$ reads as

$$\tilde{Z}(t, T) = \left. \frac{\partial \tilde{G}(x, z, t)}{\partial z} \right|_{x = z = 1} = \int_0^t S(t')Z(t-t', T)dt'. \tag{82}$$

Further, the source induced modified variance, defined in Eq. (69), derives from the above as

$$\tilde{\mu}_Z(t, T) = \int_0^t S(t')M_Z(t-t', T)dt' \tag{83}$$

Here

$$M_Z(t, T) = \int_0^t Q_Z(t', T)N(t-t')dt' \tag{84}$$

with

$$Q_Z(t, T) = \lambda_f\langle\nu(\nu-1)\rangle Z^2(t, T) \ . \tag{85}$$

and where $Z(t, T)$ is the single-particle induced detector count, given in Eq. (75). Hence, using Eqs. (81) and (82) we can write Eq. (83) as

$$\tilde{\mu}_Z(t, T) = \int_0^t Q_Z(t', T)\tilde{N}(t-t')dt' \, . \tag{86}$$

The Laplace transform of Eq. (81) is

$$\tilde{N}(s) = S(s)N(s) \tag{87}$$

where

$$N(s) = \frac{1}{s+\alpha} \tag{88}$$

since

$$N(t) = e^{-\alpha t} \tag{89}$$

where $\alpha = -\frac{\rho}{\Lambda}$ and $\rho = \frac{k-1}{k}$ as usual.

Hence

$$\tilde{N}(s) = \frac{(1-e^{-sW})}{s(1-e^{-sT_0})}\frac{1}{(s+\alpha)} \, . \tag{90}$$

From Eq. (90) we can obtain $\tilde{N}(t)$ with inverse Laplace transform. Let

$$\tilde{N}(s) = (1-e^{-sW})f(s) \tag{91}$$

where

$$f(s) = \frac{1}{s(1-e^{-sT_0})(s+\alpha)} \tag{92}$$

then

$$\tilde{N}(t) = f(t) - H(t-W)f(t-W) = \begin{cases} f(t) & t \le W \\ f(t) - f(t-W) & t > W. \end{cases} \tag{93}$$

For the inversion of Eq. (90), we note that its singularities are defined by three different types of poles, each corresponding to a different type of behaviour in the time domain after inversion.

1. A pole at $s = 0$; the corresponding residue gives the asymptotic mean value of the oscillating function $\tilde{N}(t)$;
2. A pole at $s = -\alpha$, which describes the transient after switching on the source at $t = 0$;
3. An infinite number of complex conjugate roots on the imaginary axis, yielding harmonic functions in the time domain, representing a Fourier series expansion of the oscillating part of $\tilde{N}(t)$.

As mentioned earlier, the positions of these poles are independent of the form of the pulse shape, because they are given by the zeros of the function $(1 - e^{-sT_0})$, which later was given rise by the summation of the geometric series in Eq. (79) expressing the periodicity of the pulse. It is only the value of the residues which is affected by the pulse shape. In other words, the result for the asymptotic value of $\tilde{N}_a(t)$ can always be written in the form of Eq. (102) below, only the values of the a_n and b_n will be different.

Let us write now the inverse Laplace transform of Eq. (90) in terms of the inverse of the function $f(s)$, introduced in Eq. (92), in a sum corresponding to the three types of poles above. That is, let us write $f(t) = c(t) + e(t) + g(t)$ and calculate each term separately. Then the theorem of residues gives:

$$c(t) \equiv \underset{s = 0}{Res} \frac{e^{st}}{s(1 - e^{-sT_0})(s + \alpha)} = \frac{2(t\alpha - 1) + \alpha T_0}{2\alpha^2 T_0} \tag{94}$$

$$e(t) \equiv \underset{s = -\alpha}{Res} \frac{-e^{st}}{s(1 - e^{-sT_0})(s + \alpha)} = -\frac{e^{-\alpha t}}{\alpha(1 - e^{-\alpha T_0})} \tag{95}$$

and

$$g(t) \equiv \sum_n \underset{s = s_n}{Res} \frac{e^{st}}{s(1 - e^{-sT_0})(s + \alpha)} = \frac{T_0}{\pi} \sum_{n = 1}^{\infty} \frac{\sin\left(\frac{2n\pi t}{T_0}\right)\alpha T_0 - \cos\left(\frac{2n\pi t}{T_0}\right)2n\pi}{n[(2n\pi)^2 + (\alpha T_0)^2]} \; . \tag{96}$$

Hence, also in view of Eq. (93), one has

$$\tilde{N}(t) = c(t) + e(t) + g(t) - (c(t - W) + e(t - W) + g(t - W))H(t - W) \; . \tag{97}$$

A plot of $\tilde{N}(t)$ is shown in Fig. 19. It is obvious that after a number of pulses the initial transient decays and the system converges to an asymptotic state.

When $t \to \infty$, $\tilde{N}(t)$ simplifies into:

$$\tilde{N}_a(t) = \frac{W}{T_0 \alpha} + g(t) - g(t - W) \; . \tag{98}$$

Using trigonometric identities and introducing $\omega_n \equiv \frac{2\pi n}{T_0}$, we get:

$$ggw(t) \equiv g(t) - g(t - W) = \frac{1}{\pi} \sum_{n = 1}^{\infty} a_n \sin(\omega_n t) + b_n \cos(\omega_n t) \tag{99}$$

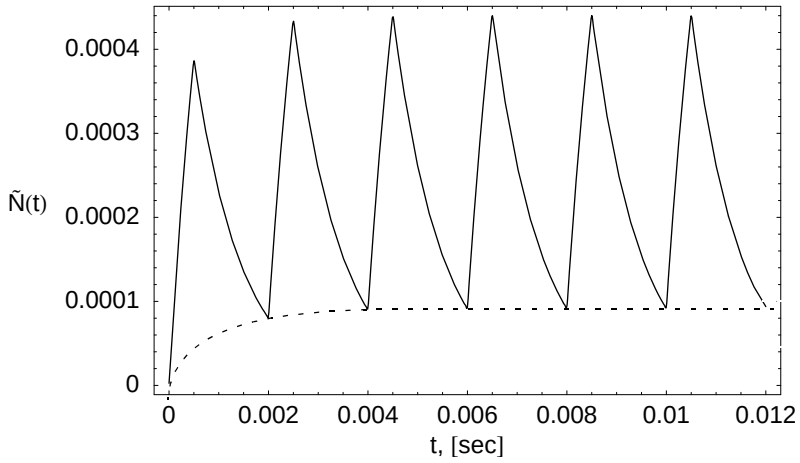

Fig. 19. *$\tilde{N}(t)$ with its asymptotic behaviour indicated as a dotted line. Numerical values are found in Table II on page 54.*

where

$$a_n = \frac{[1-\cos(\omega_n W)]\alpha + \omega_n \sin(\omega_n W)}{n(\omega_n^2 + \alpha^2)} \tag{100}$$

and

$$b_n = \frac{\alpha \sin(\omega_n W) - \omega_n [1-\cos(\omega_n W)]}{n(\omega_n^2 + \alpha^2)} \, . \tag{101}$$

Thus, the asymptotic source induced neutron number, $\tilde{N}_a(t)$, is:

$$\tilde{N}_a(t) = \frac{W}{T_0 \alpha} + \frac{1}{\pi} \sum_{n=1}^{\infty} a_n \sin(\omega_n t) + b_n \cos(\omega_n t) \, . \tag{102}$$

This function is shown in Fig. 20.

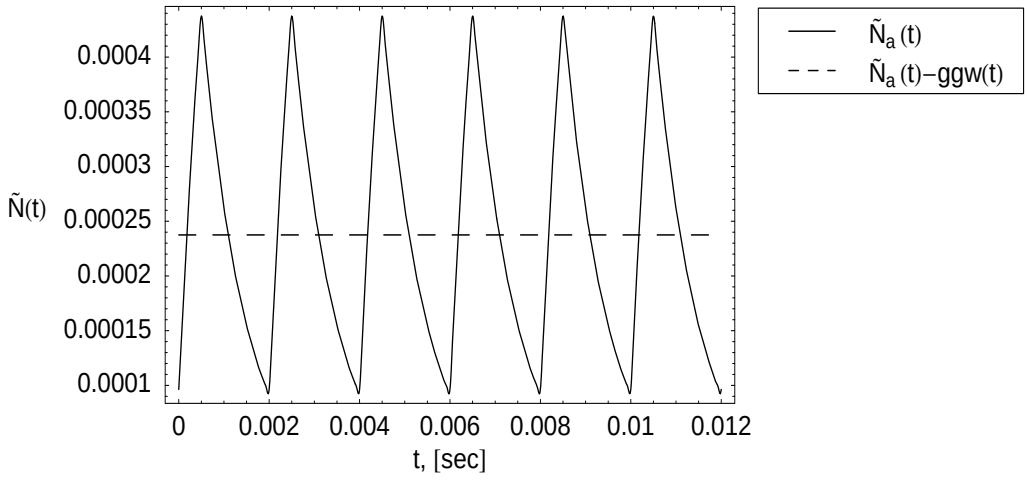

Fig. 20. *$\tilde{N}_a(t)$ and the constant term in $\tilde{N}_a(t)$ i.e. $\tilde{N}_a(t) - ggw(t)$. Numerical values are found in Table II on page 54.*

As will be seen in the next two subsections, in all subsequent calculations of the source-induced asymptotic detector count $\tilde{Z}_a(t)$ and the Feynman $Y(t)$-function, the solution given for $\tilde{N}_a(t)$ above is used in various nested integrals in combination with functions that do not depend on source properties. The functional dependence of $\tilde{N}_a(t)$ is given by the trigonometric functions that do not depend on the pulse shape. Hence in the resulting expressions using a different pulse shape means just changing the parameters a_n, b_n and the first term on the r.h.s. of Eq. (102).

2.3.3 Calculation of the source-induced detector count for arbitrary pulses

The single-particle induced detector count, $Z(t, T)$ is given, as usual (c.f. Eq. (75)):

$$Z(t, T) = \lambda_d \int_0^t \Delta(t', T) N(t - t') dt' = \begin{cases} \frac{\lambda_d}{\alpha}(1 - e^{-\alpha t}); & 0 \le t \le T \\ \frac{\lambda_d}{\alpha} e^{-\alpha t}(e^{\alpha T} - 1); & t > T. \end{cases} \tag{103}$$

where $\Delta(t, T)$ was defined in Eq. (74).

From Eq. (82) the source-induced detector count, $\tilde{Z}(t, T)$, is given by:

$$\tilde{Z}(t, T) = \lambda_d \int_0^t \Delta(t', T) \tilde{N}(t - t') dt' . \tag{104}$$

The easiest way to calculate the integral is not with the same method as was used for $\tilde{N}(t)$, i.e. writing the Laplace transform of $\tilde{Z}(t, T)$ as:

$$\tilde{Z}(s, T) = \lambda_d \Delta(s, T) \tilde{N}(s) = \lambda_d \frac{(1 - e^{-sT})}{s} \frac{(1 - e^{-sW})}{s(1 - e^{-sT_0})} \frac{1}{s + \alpha} . \tag{105}$$

The reason is, that for Eq. (105) it is rather complicated to use the same trick as for Eq. (91)

due to the factor $(1-e^{-sT})(1-e^{-sW})$. Further, it is easier to let $t \to \infty$ in Eq. (104) than in Eq. (105). But, since we have a simple expression for $\tilde{N}_a(t)$, i.e. Eq. (102), we are able to obtain the asymptotic source-induced detector count by calculating the integral in Eq. (104) when $t \to \infty$. Thus,

$$\tilde{Z}_a(T) = \lim_{t\to\infty} \lambda_d \int_0^t \Delta(t', T)\tilde{N}_a(t-t')dt' \quad . \tag{106}$$

As a result of deterministic pulsing we have $t = KT_0 + T$ and it is obvious that letting $t \to \infty$ equals to letting $K \to \infty$. With that, we have:

$$\tilde{Z}_a(T) = \lambda_d \int_0^{KT_0+T} \Delta(t', T)\tilde{N}_a(t-t')dt' = \lambda_d \int_{KT_0}^{KT_0+T} \tilde{N}_a(t)dt = \lambda_d \int_0^T \tilde{N}_a(t)dt \quad . \tag{107}$$

The last step above results from the periodic character of $\tilde{N}_a(t)$. The above gives, with Eq. (102):

$$\tilde{Z}_a(T) = \lambda_d \Bigg\{ \underbrace{\frac{WT}{T_0\alpha}}_{\tilde{Z}_l} + \underbrace{\frac{1}{\pi}\sum_{n=1}^{\infty}\frac{1}{\omega_n}\{a_n(1-\cos(\omega_n T)) + b_n \sin(\omega_n T)\}}_{\tilde{Z}_{osc}} \Bigg\} \quad . \tag{108}$$

Plots of the linear and oscillating terms can be found in [39].

2.3.4 Calculation of the modified variance for arbitrary sources

The asymptotic modified variance is obtained from Eq. (86) using the asymptotic source induced neutron number, $\tilde{N}_a(t)$:

$$\tilde{\mu}_Z(t, T) = \int_0^t Q_Z(t', T)\tilde{N}_a(t-t')dt' \tag{109}$$

where $Q_Z(t, T)$ is defined in Eq. (85) with $Z(t, T)$ given by Eq. (103).

Let $C \equiv \lambda_d \langle \nu(\nu-1) \rangle$, and for $t < T$ we define with Eq. (103):

$$Q_1(t) = C\left(\frac{\lambda_d}{\alpha}\right)^2 (1-e^{-\alpha t})^2 \tag{110}$$

and for $t > T$:

$$Q_2(t) = C\left(\frac{\lambda_d}{\alpha}\right)^2 e^{-2\alpha T}(e^{\alpha T}-1)^2 \, . \tag{111}$$

Correspondingly, the expression for the modified variance, eq. (109) will be broken up into two parts, i.e. $\mu_Z(t, T) = \mu_1(T) + \mu_2(T)$, with $\mu_1(T)$ and $\mu_2(T)$ corresponding to the integrals over $Q_1(t)$ and $Q_2(t)$, respectively. If we also let $t = KT_0 + T$, we obtain:

$$\tilde{\mu}_Z(KT_0 + T, T) = \int_0^T Q_1(t)\tilde{N}_a(T-t)dt + \int_T^{KT_0+T} Q_2(t, T)\tilde{N}_a(T-t)dt \quad . \tag{112}$$

When $t \to \infty$:

$$\tilde{\mu}_Z(KT_0 + T, T) = \underbrace{\int_0^T Q_1(t)\tilde{N}_a(T-t)dt}_{\mu_1(T)} + \underbrace{\int_0^\infty Q_2(T+t, T)\tilde{N}_a(-t)dt}_{\mu_2(T)} \quad . \tag{113}$$

Using Eqs. (98) and (99) the $\mu_1(t)$-integral becomes:

$$\mu_1(T) = \int_0^T Q_1(t)\left\{\frac{W}{T_0\alpha} + ggw(T-t)\right\}dt = \frac{W}{T_0\alpha}\int_0^T Q_1(t)dt + \int_0^T Q_1(T-t)ggw(t)dt \quad . \tag{114}$$

Using Eq. (110), the result of the first integral is:

$$\frac{W}{T_0\alpha}\int_0^T Q_1(t)dt = C\left(\frac{\lambda_d}{\alpha}\right)^2 \frac{W}{T_0\alpha}\frac{2T\alpha + 4e^{-\alpha T} - e^{-2\alpha T} - 3}{2\alpha} \quad . \tag{115}$$

The second integral in Eq. (114) is somewhat more difficult to evaluate. We notice that, according to Eq. (110), we have:

$$Q_1(T-t) = C\left(\frac{\lambda_d}{\alpha}\right)^2 (1 - e^{-\alpha(T-t)})^2 = 1 - 2e^{-\alpha T}e^{\alpha t} + e^{-2\alpha T}e^{2\alpha t} \quad . \tag{116}$$

The function $ggw(t)$ is given by Eq. (99). It is suitable to evaluate the integral in two parts. First, the one with the sine and second, the one with the cosine functions. Now, let

$$p_n(\alpha, T) \equiv e^{-\alpha T}\int_0^T e^{\alpha t}\sin(\omega_n t)dt = \frac{\alpha\sin(\omega_n T) + \omega_n(e^{-\alpha T} - \cos(\omega_n T))}{\alpha^2 + \omega_n^2} \quad . \tag{117}$$

Then,

$$A_n(T) \equiv \int_0^T Q_1(T-t)\sin(\omega_n t)dt = C\left(\frac{\lambda_d}{\alpha}\right)^2 (p_n(0, T) - 2p_n(\alpha, T) + p_n(2\alpha, T)) \quad . \tag{118}$$

Analogously, let

$$q_n(\alpha, T) \equiv e^{-\alpha T}\int_0^T e^{\alpha t}\cos(\omega_n t)dt = \frac{\alpha\sin(\omega_n T) + \omega_n(e^{-\alpha T} - \sin(\omega_n T))}{\alpha^2 + \omega_n^2} \quad . \tag{119}$$

Then,

$$B_n(T) \equiv \int_0^T Q_1(T-t)\cos(\omega_n t)dt \;=\; C\left(\frac{\lambda_d}{\alpha}\right)^2 (q_n(0,T) - 2q_n(\alpha,T) + q_n(2\alpha,T)) \qquad (120)$$

and

$$\int_0^T Q_1(T-t)ggw(t)dt \;=\; C\left(\frac{\lambda_d}{\alpha}\right)^2 \frac{1}{\pi}\sum_{n=1}^{\infty}\{a_n A_n(T) + b_n B_n(T)\}\;. \qquad (121)$$

Finally, we have from Eqs. (115) and (121):

$$\mu_1(T) \;=\; C\left(\frac{\lambda_d}{\alpha}\right)^2 \left(\frac{W}{T_0\alpha}\frac{2T\alpha + 4e^{-\alpha T} - e^{-2\alpha T} - 3}{2\alpha} + \frac{1}{\pi}\sum_{n=1}^{\infty}\{a_n A_n(T) + b_n B_n(T)\} \right)\;. \qquad (122)$$

Using Eqs. (98) and (99) the $\mu_2(t)$-integral in Eq. (113) becomes:

$$\mu_2(T) \;=\; \int_0^1 Q_2(T+t,T)\left\{\frac{W}{T_0\alpha} + ggw(-t)\right\}dt \;= \qquad . \qquad (123)$$

$$C\left(\frac{\lambda_d}{\alpha}\right)^2 (1-e^{-\alpha T})^2 \int_0^T e^{-2\alpha t}\left[\frac{W}{T_0\alpha} + ggw(-t)\right]dt$$

The first term in the integral above results in:

$$\frac{W}{T_0\alpha}\int_0^{\infty} e^{-2\alpha t}dt \;=\; \frac{W}{2T_0\alpha^2}\,. \qquad (124)$$

The first part of the $ggw(t)$-integral gives:

$$\int_0^{\infty} e^{-2\alpha t}\sin(-\omega_n t)dt \;=\; \frac{-\omega_n}{\omega_n^2 + (2\alpha)^2}, \qquad (125)$$

and the second:

$$\int_0^{\infty} e^{-2\alpha t}\cos(-\omega_n t)dt \;=\; \frac{2\alpha}{\omega_n^2 + (2\alpha)^2}\,. \qquad (126)$$

Then the result to Eq. (123) is:

$$\mu_2(T) \;=\; C\left(\frac{\lambda_d}{\alpha}\right)^2 (1-e^{-\alpha T})^2 \left\{ \frac{W}{2T_0\alpha^2} + \frac{1}{\pi}\sum_{n=1}^{\infty}\frac{-a_n\omega_n + 2\alpha b_n}{\omega_n^2 + (2\alpha)^2} \right\}. \qquad (127)$$

The sum of Eqs. (122) and (127) is the result to Eq. (113):

$$\tilde{\mu}_z(T) = C\left(\frac{\lambda_d}{\alpha}\right)^2\left\{\frac{WT}{T_0\alpha}\left(1-\frac{1-e^{-\alpha T}}{\alpha T}\right)+\frac{1}{\pi}\sum_{n=1}^{\infty}\{a_nA_n(T)+b_nB_n(T)\}\right.$$
$$\left.+(1-e^{-\alpha T})^2\frac{1}{\pi}\sum_{}^{\infty}\frac{-a_n\omega_n+2b_n\alpha}{\omega^2+(2\alpha)^2}\right\}. \qquad (128)$$

Finally, the Feynman Y-function is given by Eqs. (108) and (128), as usual as:

$$Y(T) = \frac{\tilde{\mu}_z(T)}{\tilde{Z}_a(T)}. \qquad (129)$$

Fig. 21 shows the resulting Feynman Y-function for the case with square pulses. The function is multiplied with a factor $\alpha^2/(\lambda_d\lambda_f\langle\nu(\nu-1)\rangle)$. The source pulses and the case with no pulsing are included in the figure as well.

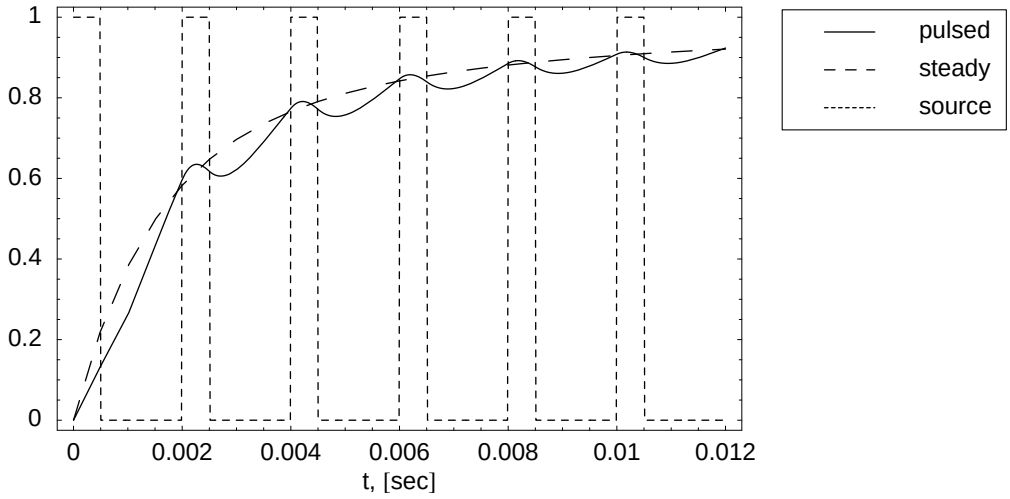

Fig. 21. *Feynman Y-curve for square pulses.The numerical values used are found in Table II on page 54.*

2.3.5 The case with Gaussian pulses

It is possible to use Gaussian pulses instead of the square pulses in Eq. (78). Then the time-dependent neutron source is represented by:

$$S(t) = \sum_n S_n(t) = \sum_{n=0}^{\infty}\frac{\tilde{s}}{\sqrt{2\pi}\sigma}\exp\left[\frac{-\left(t-\frac{W}{2}-nT_0\right)^2}{2\sigma^2}\right] \qquad (130)$$

where $\sigma = W/4$ and $\tilde{s} = \sqrt{2\pi}\sigma$. The parameter $\tilde{s}$ here plays the role of the source intensity, i.e. the same as S_0 for the square pulses in Eq. (78). Its numerical value does not play a role in the derivation of the formulae, since it drops out from the Feynman-alpha function, which is one of the advantages of the variance-to-mean method. Hence its value was chosen such that the maximum value of the pulse function is unity. This choice has no other motivation than easy comparison of the source forms in the plots. Likewise, the choice of $\sigma = W/4$ is also arbitrary, and again was made so that the square and Gaussian pulses are comparable. One representation of such a Gaussian train, with its square pulse companion with the same repetition frequency and corresponding width W, is shown in

Fig. 22.

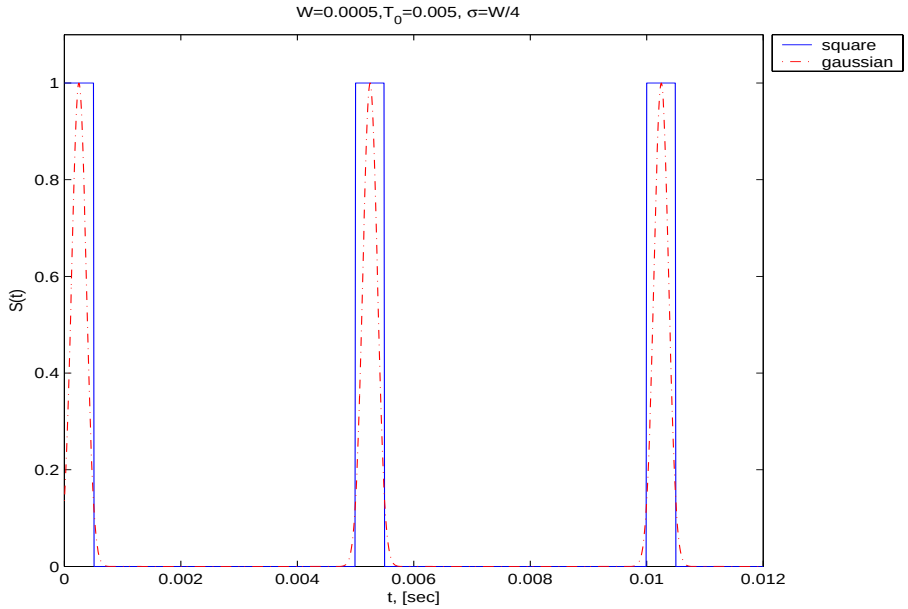

Fig. 22. *The Gaussian pulse and the square pulse,*
$W = 0.0005, T_0 = 0.005, \sigma = W/4, \tilde{s} = \sigma\sqrt{2\pi}$

The Laplace transform of $S_n(t)$ is then

$$S_n(s) = \int_0^\infty e^{-st} S_n(t)dt = e^{-nsT_0}\int_0^\infty S_0(t)e^{-st}dt; \quad Re\{s\} > 0\,. \tag{131}$$

The task is hence to calculate the integral for the term $n = 0$. This can be simplified as follows:

$$\int_0^\infty S_0(t)e^{-st}dt = \frac{\tilde{s}}{\sqrt{2\pi}\sigma}\int_0^\infty e^{-st}\exp\left[\frac{-\left(t-\frac{W}{2}\right)^2}{2\sigma^2}\right]dt \approx$$
$$\approx \frac{\tilde{s}}{\sqrt{2\pi}\sigma}\int_{-\infty}^\infty e^{-st}\exp\left[\frac{-\left(t-\frac{W}{2}\right)^2}{2\sigma^2}\right]dt = \tilde{s}e^{\frac{-sW+(\sigma s)^2}{2}} \tag{132}$$

As is seen, the lower limit of the integral was extended to minus infinity. The error committed by this step is rather small, given the fast decay of the Gauss function. This may not be so obvious when it is expressed in terms of the very first pulse, which starts close to the origin. However, for the later pulses it becomes a better and better approximation. Since the Feynman-alpha measurement relates to the stationary case, i.e. times long after the switching on the source, the error committed by this approximation is indeed negligible. In return, it leads to a compact analytic form.

Thus, the Laplace transform of the sum in Eq. (132) is equal to

$$S(s) = \frac{\tilde{s}e^{\frac{-sW+(\sigma s)^2}{2}}}{1-e^{sT_0}}. \tag{133}$$

According to Eqs. (87) and (88) we have:

$$\tilde{N}(s) = \frac{\tilde{s}e^{\frac{-sW+(\sigma s)^2}{2}}}{1-e^{sT_0}}\frac{1}{s+\alpha}. \tag{134}$$

For the inversion of Eq. (134) we note that the singularities are of the same three types as in Eq. (90). We write the inverse Laplace transform, in a similar manner as for the square pulse, as $f(t) = c(t) + e(t) + g(t)$ and calculate each term separately. Then the theorem of residues gives:

$$c(t) \equiv \underset{s=0}{Res}\ \frac{\tilde{s}e^{st}}{(1-e^{-sT_0})(s+\alpha)}e^{\frac{-sW+(\sigma s)^2}{2}} = \frac{\tilde{s}}{T_0\alpha} \tag{135}$$

$$e(t) \equiv \underset{s=-\alpha}{Res}\ \frac{\tilde{s}e^{st}}{(1-e^{-sT_0})(s+\alpha)}e^{\frac{-sW+(\sigma s)^2}{2}} = \frac{\tilde{s}e^{-\alpha t}}{(1-e^{-\alpha T_0})}e^{\frac{-\alpha W+(\sigma\alpha)^2}{2}} \tag{136}$$

and

$$g(t) \equiv \sum_n \underset{s=s_n}{Res}\ \frac{\tilde{s}e^{st}}{(1-e^{-sT_0})(s+\alpha)}e^{\frac{-sW+(\sigma s)^2}{2}} = \frac{1}{\pi}\sum_{n=1}^{\infty}(a_n\sin(\omega_n t) + b_n\cos(\omega_n t)) \tag{137}$$

where

$$a_n = \frac{2\pi\tilde{s}e^{-\frac{(\omega_n\sigma)^2}{2}}}{(\alpha T_0)^2+(2\pi n)^2}\left\{\alpha T_0\sin\left(\omega_n\frac{W}{2}\right) + 2\pi n\cos\left(\omega_n\frac{W}{2}\right)\right\} \tag{138}$$

$$b_n = \frac{2\pi\tilde{s}e^{-\frac{(\omega_n\sigma)^2}{2}}}{(\alpha T_0)^2+(2\pi n)^2}\left\{\alpha T_0\cos\left(\omega_n\frac{W}{2}\right) - 2\pi n\sin\left(\omega_n\frac{W}{2}\right)\right\}. \tag{139}$$

It is obvious that when $t\to\infty$, $e(t)\to 0$ and the asymptotic source-induced neutron number is:

$$\tilde{N}_a(t) = \frac{\tilde{s}}{T_0\alpha} + \frac{1}{\pi}\sum_{n=1}^{\infty}(a_n\sin(\omega_n t) + b_n\cos(\omega_n t)) \tag{140}$$

where a_n and b_n are as in Eqs. (138) and (139), respectively.

Above, $\tilde{N}_a(t)$ is written in a similar way as in the case with the square pulse, i.e.

$$\tilde{N}_a(t) = C_s + \frac{1}{\pi}\sum_{n=1}^{\infty}(a_n\sin(\omega_n t) + b_n\cos(\omega_n t)), \tag{141}$$

where C_s is a constant that depends on the pulse form. Thus, we are able to use the same formulas for the source induced detector count, Eq. (108), and modified variance, Eq. (128)

as for the square pulse with minor modifications. So, we have:

$$\tilde{Z}_a(T) = \lambda_d \left\{ \underbrace{\frac{\tilde{s}T}{T_0\alpha}}_{\tilde{Z}_l} + \underbrace{\frac{1}{\pi}\sum_{n=1}^{\infty}\frac{1}{\omega_n}\{a_n(1-\cos(\omega_n T)) + b_n \sin(\omega_n T)\}}_{\tilde{Z}_{osc}} \right\} \tag{142}$$

and

$$\tilde{\mu}_z(T) = C\left(\frac{\lambda_d}{\alpha}\right)^2 \left(\frac{\tilde{s}T}{T_0\alpha}\left(1 - \frac{1-e^{-\alpha T}}{\alpha T}\right) + \frac{1}{\pi}\sum_{n=1}^{\infty}\{a_n A_n(T) + b_n B_n(T)\} + (1-e^{-\alpha T})^2 \frac{1}{\pi}\sum_{n=1}^{\infty}\frac{-a_n\omega_n + 2b_n\alpha}{\omega_n^2 + (2\alpha)^2} \right) \tag{143}$$

where A_n and B_n are as in Eqs. (118) and (120), respectively. The resulting Feynman Y-function is given by Eq. (129), as usual.

Fig. 23 shows the resulting Y-curve for both the Gaussian and the square pulses. In the Figure, the function is multiplied with a factor $\alpha^2/(\lambda_d\lambda_f\langle\nu(\nu-1)\rangle)$. The source pulses and the case with no pulsing are included in the Figure as well. The Figure shows that the

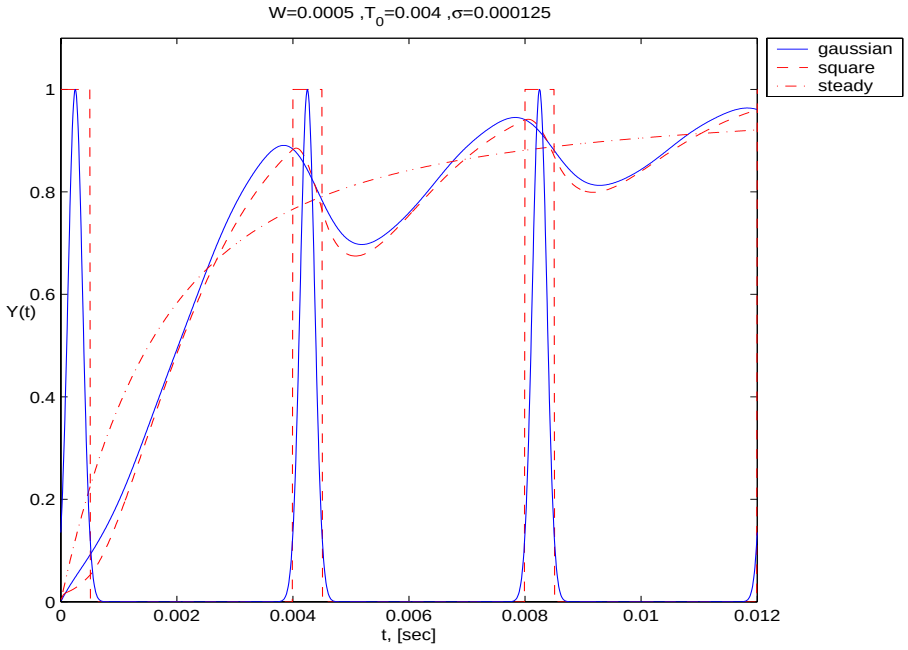

Fig. 23. *Feynman Y-curve for Gaussian and square pulse. The numerical values included are* $W = 0.0005, T_0 = 0.004, \sigma = W/4, \tilde{s} = \sigma\sqrt{2\pi}$

Y-curve due to the Gaussian source shape is smoother than the one due to the square counterpart. This is because a Gaussian pulse does not contain sharp edges (discontinuous derivatives) as the square function does.

2.4 Analysis of the behaviour

In this section a number of plots of Feynman Y-function for a number of W- and T_0-values are presented. All curves are normalized with a factor $\alpha^2/(\lambda_d\lambda_f\langle\nu(\nu-1)\rangle)$. In the numerical work that follows, in this and the following Section, the following numerical values will be used:

Table II. : Numerical parameters

Parameter	Value
T_0	$2 \cdot 10^{-3}$ s
W	$5 \cdot 10^{-4}$ s
S_0	1 n/s
k	0.95
Λ	$5 \cdot 10^{-5}$ s

With the above data, one obtains $\alpha = -\rho/\Lambda = 1052.(6)\ \ s^{-1}$

The effect of the pulse width is illustrated in Figs. 24 and 25 for square pulses. It is seen that the wider the pulse is, the smoother the curves become. This is not surprising, since the continuous source corresponds to the case when the pulse is as wide as the pulsing period, which gives a completely smooth curve. Fig. 25 corresponds to the pulsing with a very narrow pulse. Such results were obtained by other groups e.g. in Japan, and are in agreement with our results.

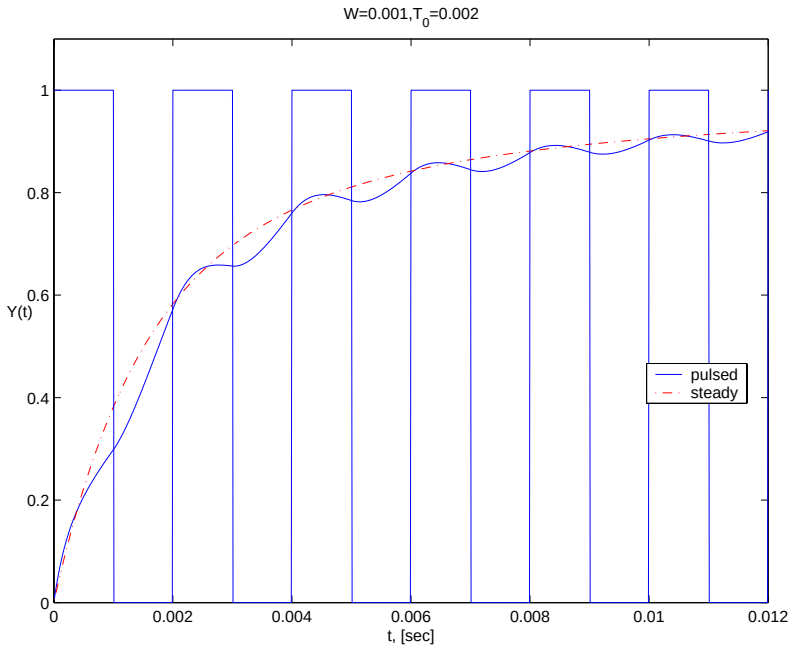

Fig. 24. *Feynman Y-curve for W=0.001 and T_0=0.002*

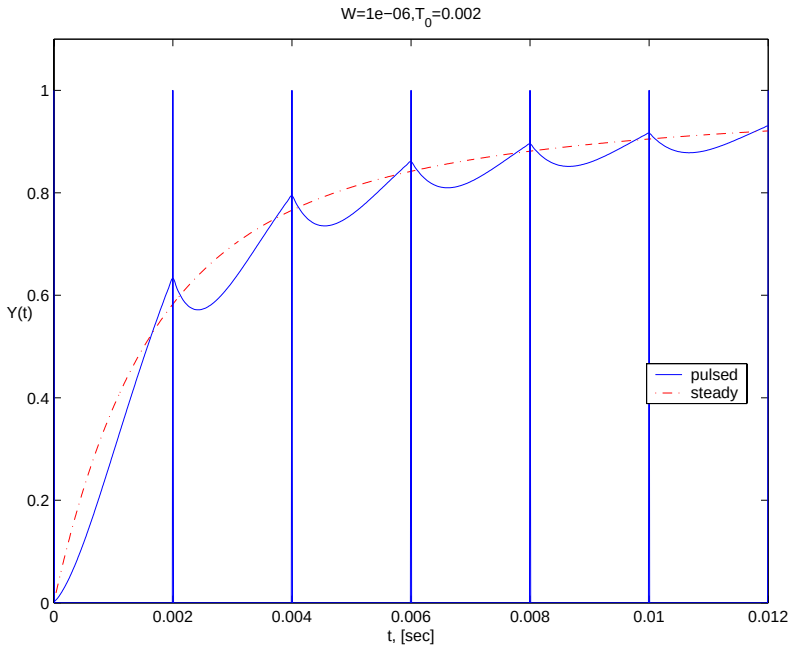

Fig. 25. *Feynman Y-curve for $W=1e^{-6}$ and $T_0=0.002$*

For the sake of comparisons, a Feynman Y-curve with Gaussian pulses, with the same repetition frequency as with the square pulses above, is shown in Fig. 26. Although it

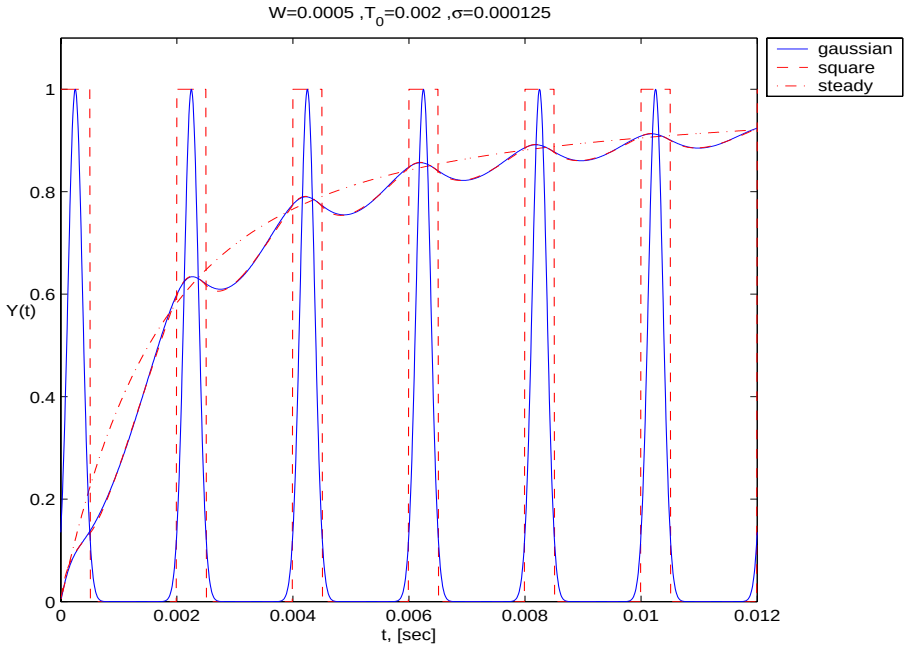

Fig. 26. *The resulting Feynman Y-curve for Gaussian and square pulse, included numerical values are* $W = 0.0005, T_0 = 0.002, \sigma = W/4, \tilde{s} = \sigma\sqrt{2\pi}$

corresponds to much narrower pulses than the case in Fig. 24 for the square pulses, the Y-curve is just as smooth as for a wider square pulse. This is because of the smoother character of the Gaussian pulse shape.

The effect of the repetition frequency, with a given prompt neutron time constant, is shown in Figs. 27-30. The Figures show that for a sufficiently high repetition frequency

(Figs. 27 and 28), the pulsed curve remains smooth and close to the continuous curve even for narrow pulses. However, for a repetition frequency which is low compared to the reactor prompt time constant, the deviations between the pulsed and the continuous case are rather large (Figs. 29 and 30). This is the case with the majority of the MUSE experiments. The only way of compensating for this would be to use pulses as wide as possible.

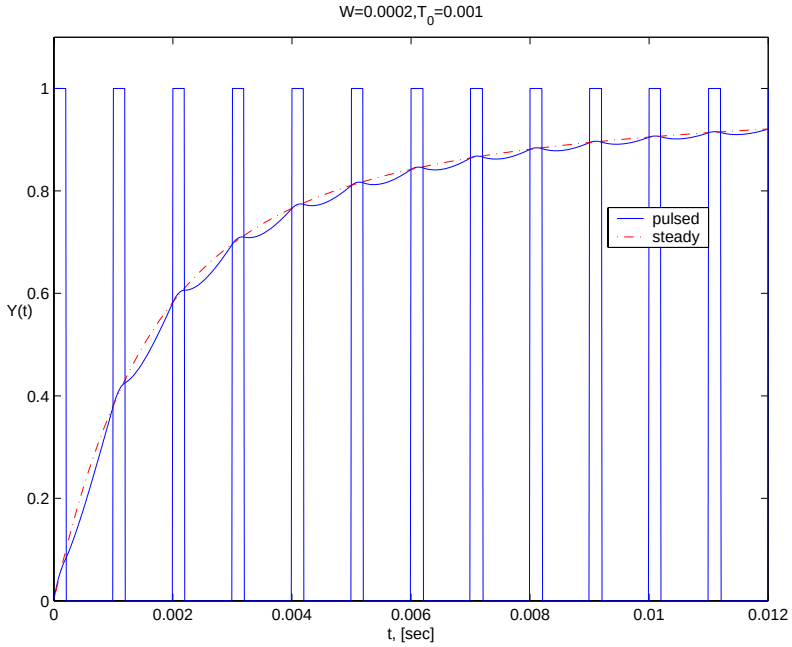

Fig. 27. *Feynman Y-curve for W=0.0002 and T_0=0.001*

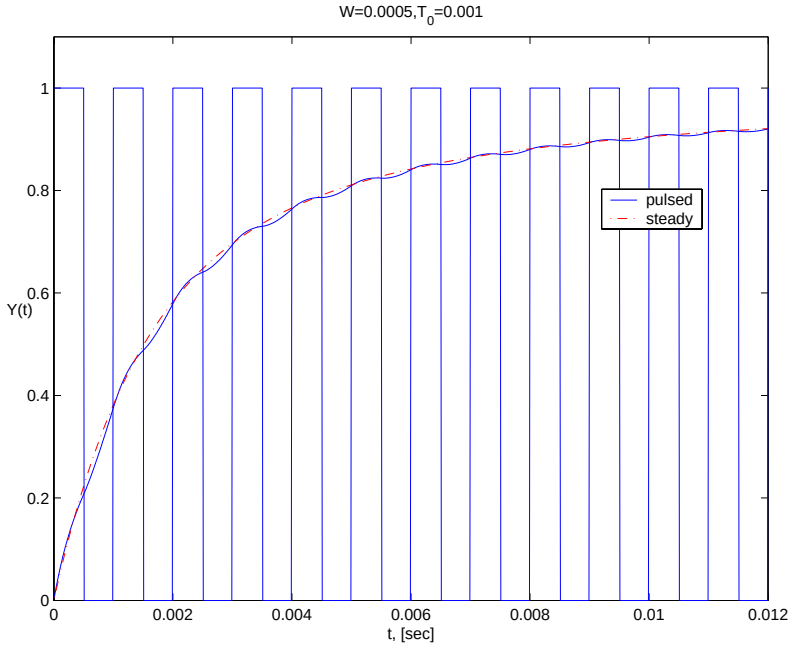

Fig. 28. *Feynman Y-curve for W=0.0005 and T_0=0.001*

A similar figure, showing the Y-curve for both Gaussian and square pulses is shown in Fig. 31 below. It illustrates the already mentioned fact that the Y-curve corresponding to Gauss pulse shapes is smoother than its counterpart which is due to square pulses.

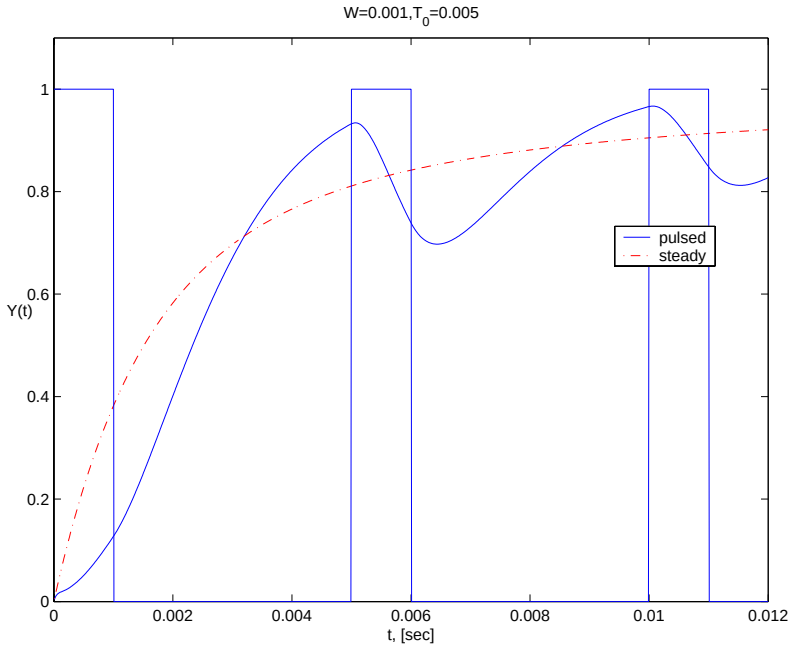

Fig. 29. *Feynman Y-curve for W=0.001 and T_0=0.005*

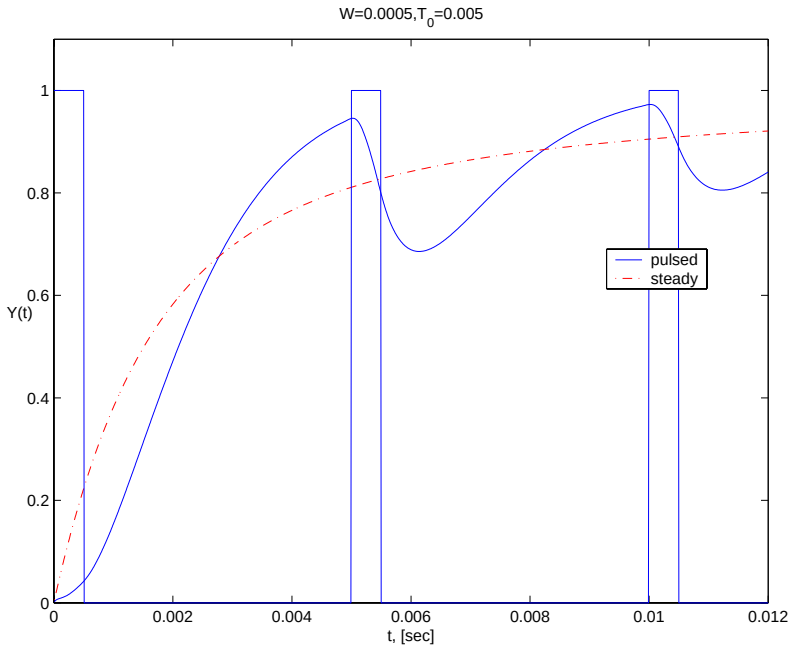

Fig. 30. *Feynman Y-curve for W=0.0005 and T_0=0.005*

2.5 Determination of the parameter α from a simulated measurement

It is possible to simulate a measurement using the formulas in Section 2.3 and adding a random noise to it, to simulate the imperfect character of an experiment. Using a MATLAB routine, *lsqcurvefit*, which solves curve-fitting problems in the least-squares sense, it is possible to estimate the value of α. Figs. 32 and 33 show Feynman Y-curves with simulated measurements for two different noise levels. In this study only square pulses are assumed, and the pulse repetition frequency and the pulse width are assumed to be known

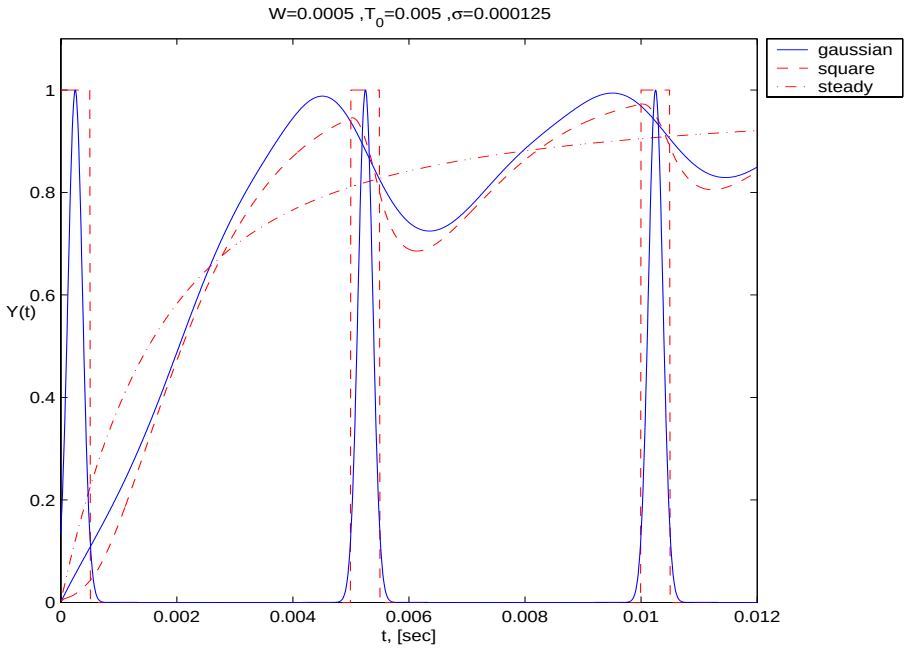

Fig. 31. *The resulting Feynman Y-curve for Gaussian and square pulse, included numerical values are* $W = 0.0005, T_0 = 0.005, \sigma = W/4, \tilde{s} = \sigma\sqrt{2\pi}$

exactly. In reality this is not true, and a sensitivity analysis of the unfolding method to inaccuracies in those parameters should also be performed, which will be made at a later stage.

The resulting curve for the estimated α is included in the Figures below as well. The true Y-curve and the one obtained by the parameter α from the fitting procedure cannot be distinguished in the Figures. In all Figures, α_0 denotes the original value and α_n denotes the estimated value. In Figs. 32 and 33 the noise level is 4 and 8 percent of the asymptotic value of the original Feynman-Y curve, respectively.

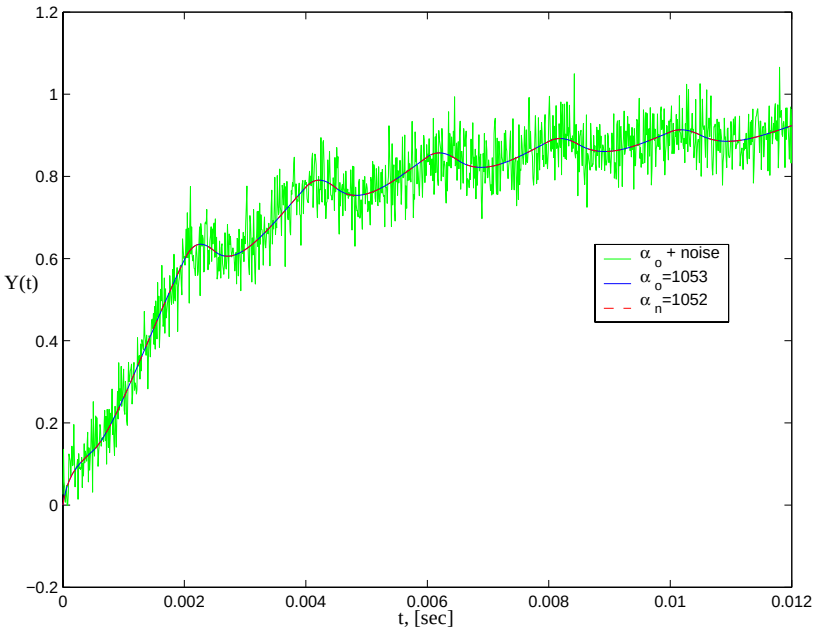

Fig. 32. *Feynman-Y curve for a simulated measurement, the noise level is 4%*

In both cases, the true value α_0 was 1053. In the case with lower noise level, the α_n

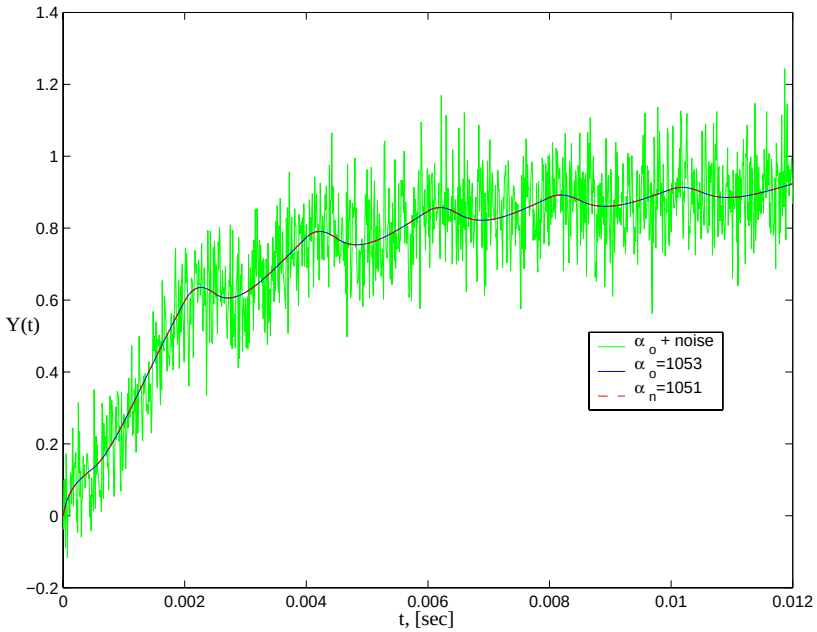

Fig. 33. *Feynman-Y curve with simulated noise, the noise level is 8%*

determined from the curve fitting was 1052, while in the second case α_n was 1051. However, the precision of the method depends on the level of the added noise and even for the same noise strength, the particular realisation of the random noise. This is illustrated with the case shown in Fig. 34. The noise level is the same as in Fig. 33, i.e. 8 percent, but the estimated α is 1062.

The few cases shown here support the statement that with the formula for the deterministically pulsed Feynman-alpha measurements, the prompt neutron time constant can be estimated with curve fitting similarly to the traditional case of constant source. Test of the method with real measurement data will be reported in a forthcoming publication.

2.6 Conclusions

Calculation of the deterministically pulsed Feynman-alpha formula with the method introduced in this report leads to a compact solution which is easy to use in numerical work. One particular advantage, demonstrated in this report, is the ease with which various forms of the pulse shape can be handled. All that is needed is a Fourier-series expansion of the asymptotic form of the source-induced neutron number. Once the coefficients of this quantity are obtained, they can be substituted into a general formula for the relative variance, which was derived in the report.

The Feynman formula obtained was investigated quantitatively for various pulse parameters and even shapes. The possibility of using the formula for determining the prompt neutron time constant, and through that the reactivity, was investigated in simulations. It was found that despite the much more complicated structure of the Feynman Y-curve as compared to that with constant (time-independent) sources, the prompt alpha parameter can be extracted from a simulated experiment with methods of parameter fitting.

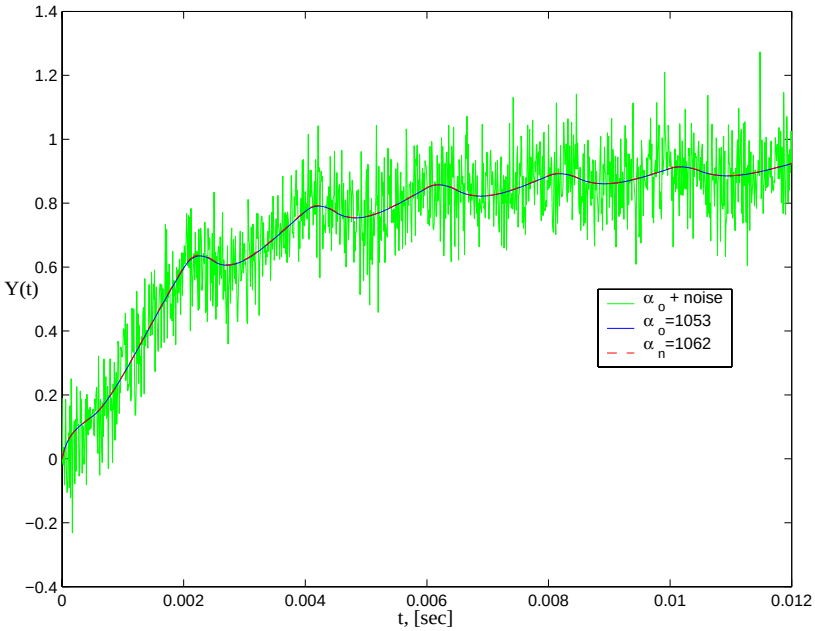

Fig. 34. *Feynman-Y curve with simulated noise, the noise level is 8%*

Section 3

Classification of two-phase flow regimes via images analysis and a neuro-wavelet approach

3.1 Introduction

Determination of the type of flow regime from measurements can be performed by several methods, but none of them is fully reliable. Therefore, there is a need to study an alternative method. It is very important to classify the different flow regimes since they have quite different flow properties. Hence, before using a flow equation, the regime must be determined so that the right expression can be chosen for i.e. the interfacial shear coefficient or some other coefficients like the heat transfer coefficient. The applied method of flow regime identification is based on intelligent computing methods and in particular the use of wavelets for feature extracting from images of the different flows, and Artificial Neural Network (ANN) algorithms, for the classification.

The focus in this report is on the following four vertical flow regimes: bubbly flow,

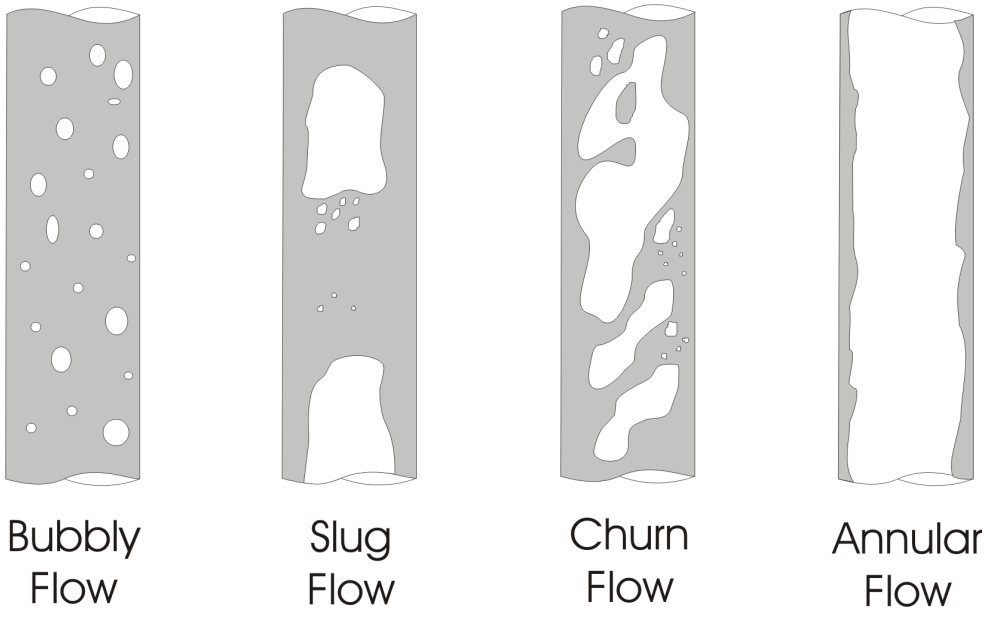

Fig. 35. *Schematic drawings of the different phases of vertical two-phase flow.*

slug flow, churn flow and finally annular flow (Fig. 35). White parts represent bubbles or steam and the darker areas are the liquid water. Bubble flow is the flow of dispersed gas in continuous liquid, small bubbles of gas in the liquid. In slug flow the bubbles of gas have formed larger regions, with a size of approximately the size of the pipe diameter. If even more gas is introduced into the pipe the bubbles break and there is an unstable regime of liquid mix with gas, churn flow. In the last type, annular flow, the pipe is almost filled with gas and just a small part, close to the wall, contains liquid.

3.2 The flow images

Two different types of images were used. The first one was obtained with neutron radiography, and it comprises all four flow regimes (Fig. 36). The second one was obtained with visible light of only bubbly and slug flow (Fig. 37).

The neutron radiographic images were made by sending a collimated neutron beam through a metallic pipe filled with water. After penetrating the pipe and the flow, the beam hits a neutron converter, which converts the neutron beam into visible light. This light, after reflection on a mirror (in order to filter out gamma-rays coming from the neutron source, usually a reactor), are recorded with a video camera. By heating up the vertical pipe, in which the water flows upwards, the different flow regimes are created. The images were recorded by the Division of Nuclear Engineering, Kyoto University Reactor Research Institute (KURRI). A drawback of this setup is the poor quality of the images, a lot of noise is present, as Fig. 36 shows.

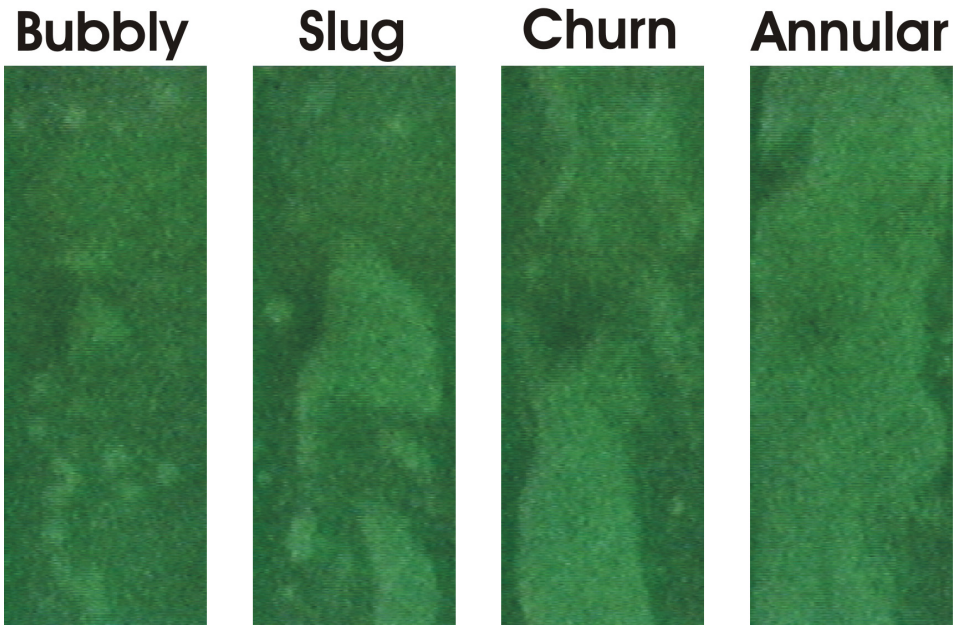

Fig. 36. *Images of two-phase flow using neutron radiography.*

To improve the quality of the images, a simpler experimental setup was used at our Department. In this case a thin transparent plastic pipe, filled with coloured water, was used to generate the images. The images were recorded with a digital video camera. The two-phase flow was simulated by injecting air in the bottom of the pipe. By this way only two-component flow could be created, with only bubbly and slug flow regimes.

From the neutron radiographic images a total of 200 frames from each of the four regimes were used for the identification and classification process, whereas from the visible light experiment 75 frames from each of the two regimes were used.

3.3 Wavelet introduction

In order to improve the classification process of the flows, it is advisable to pre-process the images using wavelet techniques [41]-[44] before extracting the input data for the Artificial Neural Networks (ANNs). The advantages using wavelet transform include some noise reduction and feature extracting at different scales and directions of the images. First a

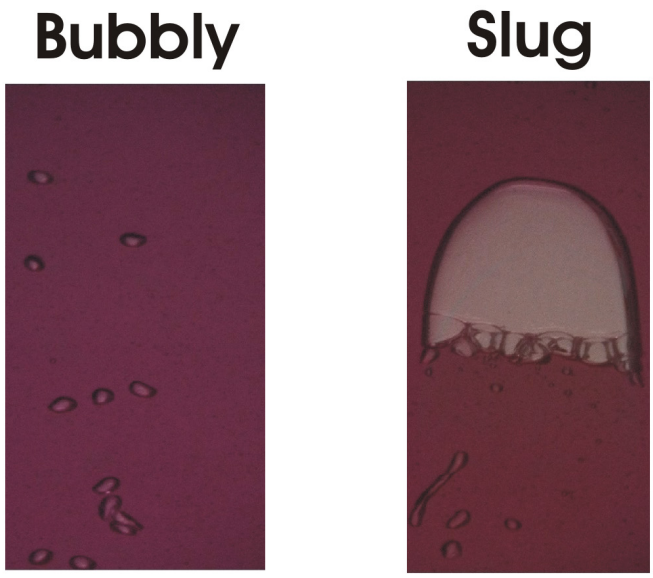

Fig. 37. *Images of two-phase flow using visible light and coloured water.*

short introduction to the wavelet transform is given followed by a description of the algorithms applied in this report.

The one-dimensional wavelet transform maps a time signal into a time and frequency signal at different frequency levels, *N*, [45]-[47]. At each level the signal is decomposed into an approximation and a detail. It is possible to do both a discrete (with discrete frequency levels), and a continuous (with continuous frequency levels), transform. In the case with an image one uses the two-dimensional wavelet transform, which maps a two-dimensional signal (image), in spatial rather than time coordinates, into the two coordinates at different frequency (wave number) levels. The two-dimensional transform can also be both discrete and continuous in the frequency coordinate or level.

At the first level of a 2-D discrete wavelet transform, the coarsest level of approximation coefficients, A_1 contains 25% of the information of the original image, S_0. The approximation coefficients, A_1, at level 1, can be used to make a reconstruction of an approximation, S_1, of the original image. In the same way the detail coefficients, T_1^h, T_1^v, and T_1^d (Fig. 38) containing the high frequency information of the image, at level 1 can be used to reconstruct horizontal, D_1^h, vertical, D_1^v, and diagonal, D_1^d, details of the original image. Adding the details to the approximation one can reconstruct the original image completely without any loss of information.

$$S_0(x,y) = S_1(x,y) + D_1^h(x,y) + D_1^v(x,y) + D_1^d(x,y) \tag{144}$$

It is possible to do the transformation into lower levels were the details at each level contain the information of the signal corresponding to the frequency of that level. But in this report only the first level of transformation is used. The coefficients and the corresponding reconstructed images contain the same information, hence it is possible to use the coefficients when extracting input data for the ANNs. The reconstructed images are useful when displaying the transform.

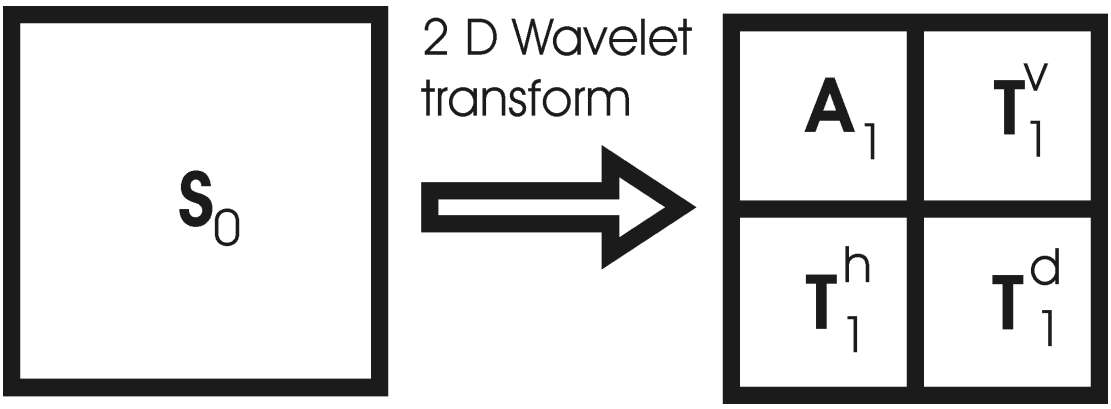

Fig. 38. *First level of the 2 D wavelet transform. S_0 is original image or data, A_1 is the set of the first level approximation coefficients and T_1 are the first level detail coefficients in each of the three directions, vertical, horizontal and diagonal.*

3.4 Wavelet pre-processing

As mentioned above, it is possible to improve the classification if the input data are pre-processed with wavelets before using them in the ANN. With the wavelets it is possible to extract features which are not visible in the original data. One set of features, mentioned in [41], is the mean and variance of the first level approximation coefficients. Another possibility would be to use the energy of the different wavelet details. The energy of each detail is defined as the sum of the square of the absolute value of the detail coefficients, [45].

$$E_1^d = \sum \left| T_{1,i}^d \right|^2 \tag{145}$$

In the first run, the neutron radiography images were analysed. Input data from the raw images were extracted and compared with the wavelet pre-processed input data. In this case the mean and variance from both the raw images and the first level approximation coefficients were used first, as reference input data. It turned out that, due to the poor image quality, no other features could be successfully used in the classification procedure.

In the second case the images produced with visible light, that had much better quality, were used. Again the mean and variance of the raw data were used as reference. Here, however, wavelet transform preprocessing did lead to improvement. With the wavelet preprocessing, the energy of the first level of detail coefficients and their variances were used, giving a total of 6 inputs for the ANN (see Fig. 40).

As usual with wavelet analysis, the choice of the right wavelet for the task at hand is not obvious. A guideline for choosing a suitable wavelet is to select one that has the same features as the data analysed. For this classification task the following wavelets were tested: Daubechies of order 8 (db8), Symmlet of order 6 (sym6), Coiflet of order 4 (coif4), Daubechies of order 1 (Haar) and biorthonormal (bior3.1). These are all available in the Wavelet Toolbox in MatLab [48].

3.5 Classification using artificial neural networks

ANNs are capable to tackle very complicated tasks, including non-linear classification problems. The backpropagation (BP) algorithm is the most frequently used algorithm for

the training of such networks. We have used the multi-layered perceptron (or simply the feed-forward network) consisting of an input layer, an output layer and one hidden layer. The network receives input through the nodes in the input layer, from which the signals propagate forward to the nodes of the consecutive layer and output signals are produced in the output layer. In the backward phase, error signals are propagated backward through the network and some parameters are adjusted in reference to the error signals.

The performance of ANNs depends strongly on input parameters. We have investigated ANNs performance for various input parameter sets. The number of the input and output nodes is defined by the problem itself. For the radiographic images, the number of input nodes was 2 and for the visible light images it was 6, as mentioned before. All the input feature vectors were normalized so that they fall in the range [-1, 1]. For each type of flow, a corresponding output class is associated. The ANN has 4 output nodes for the radiographic case and 2 output nodes for the visible light case, corresponding to the 4 or 2 different flow types (Fig. 39). The target value, during training, for each class contains the value of 0.9 for the correct category and three or one dummy variables with value of 0.1.

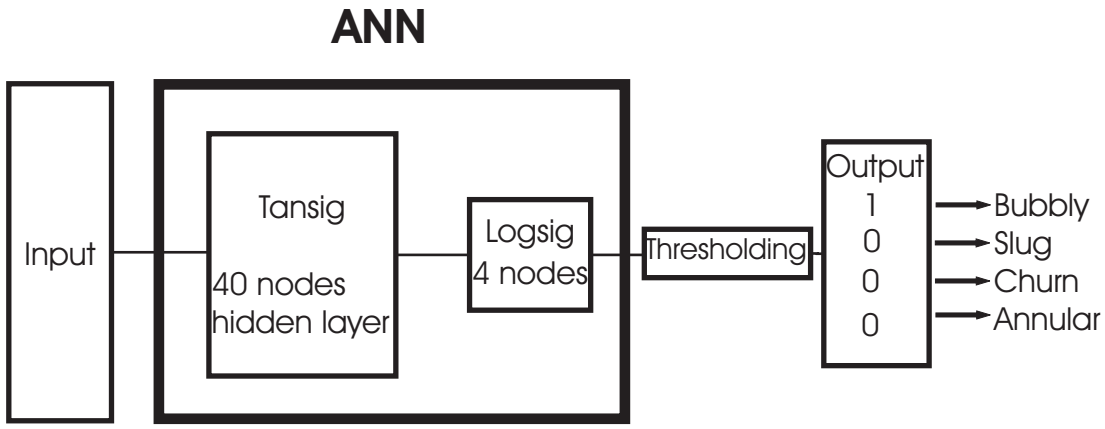

Fig. 39. *The Artificial Neural Network used in the classification process of the neutron radiographic images. The thresholding is only used during testing.*

Since the output layer chosen for this classification task has a *log-sigmoid* transfer function, the output values range from 0 to 1, and thresholding has to be preformed on the output data, to get 0 or 1, when classifying. Two different threshold levels were used, 0.5 and 0.7. All output values larger than the threshold are set to unity and all other to zero. If the output data, after the thresholding, are all four zeros, the corresponding image is classified as unknown or unclassified flow regime. The same applies for the case of more than one non-zero value. Lower threshold makes the classification less certain but a too high threshold will classify many images as unknown.

The optimal number of nodes in the hidden layer, the training algorithm and the activation functions were determined by trial and error. *Tan-sigmoid* function was used for the hidden layer and *log-sigmoid* for the output layer. A few of the modified backpropagation (BP) algorithms such as adaptive learning rate, resilient BP, scaled conjugate gradient and gradient descent algorithm with momentum were examined for training the ANN. Cross-validation was used to estimate which learning ANN model will perform the best on the problem at hand. For each of the models a 5-fold cross-validation over the training set was used, which means that 1/5th of the training data was used as a validation set and the process was repeated with non-overlapping rotations. In the case of

the neutron radiographic images, each learning model was trained with 640 samples for the four various types of flow, and then they were tested on one subset of 160 samples which was not used during training. For the visible light images, the training set consisted of 120 samples and the test subset of 30 samples (Fig. 40). The resilient backpropagation (RP) algorithm was found to have the highest average test set score. Namely, the classification efficiency with RP algorithm was 100% (the percentage of the flows that were correctly classified) when the recall test was performed on the training set, and 95% when the recall test was made on the subset not used during training. The best performance was obtained for the training and validation test set with an ANN structure consisting of one hidden layer having 40 nodes. The default performance function for feedforward networks was the mean square error, i.e. the average squared error between the network outputs and the target outputs. The ANN training was performed until the maximum number of epochs, set to 30000, was reached or the mean square error, MSE, target value of 10^{-3} was achieved. All calculations were carried out by using the toolboxes available with the technical computing software MATLAB [48].

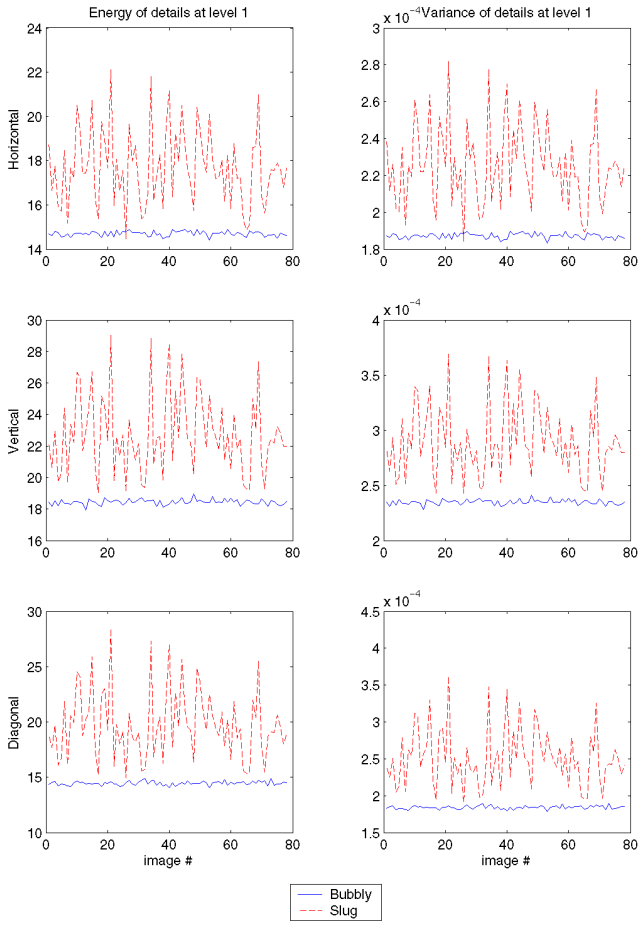

Fig. 40. *Input data of the images made with visible light after wavelet pre-processing.*

3.6 Results & Conclusions

3.6.1 Neutron Radiographic images

The effect of different wavelets, db8, sym6, coif4, haar and bior3.1, on the classification efficiency has been investigated. The classification efficiency is defined as the percentage ratio of the number of flow pictures correctly classified to the total number of pictures corresponding to one type of flow. The average efficiency of the flow classification for each type of the chosen wavelets by using ANN with mean values and variance as input and for threshold levels of 0.5 and of 0.7, is depicted in Fig. 41. The average efficiency is shown with error bars (standard deviations). Almost the same result is achieved independently of which wavelet type that is used. Though, coif4 has a slightly lower percentage of correct classified regimes and haar has the best classification efficiency.

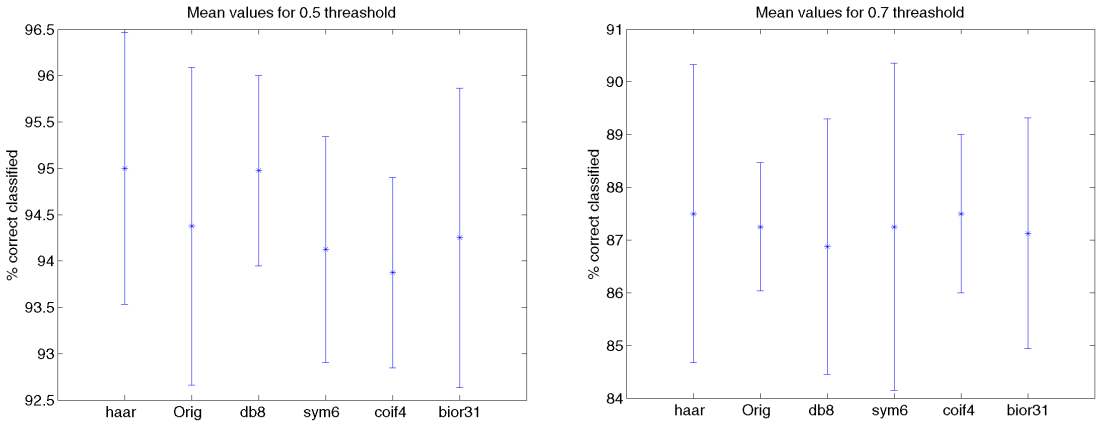

Fig. 41. *Classification efficiency for the different wavelets and the original data, threshold 0.5 to the left and 0.7 to the right.*

Clearly a threshold of 0.5, with accuracy of about 95%, is better than a threshold of 0.7, which only has about 87% correctly classified images. But even by using the mean and variance of the original image values, the efficiency is the same. There is consequently not much improvement, in classification, using the wavelet transform in this case.

All of the different wavelets classified the annular flow with 100% efficiency, which is also the case for the original data. In Fig. 42 each bar represents the 200 images from each flow and the different colours show which regime the images are classified as. White is for unknown or unclassified images. As it is seen, not that many images turn out to be unclassified for a threshold of 0.5. The most difficult regimes to classify for both the wavelet and the original data are the slug and churn flow. This is of course due to the fact that these flows have similar features.

The maximum number of epochs, 30 000, were used in the training process, meaning that the *MSE* target value of 10^{-3} was not reached.

3.6.2 Visible light images

The same five wavelets as above were used also in the case with visible light images. The results are partly similar to the radiographic images. Namely, there is not much increase of the classification efficiency when using wavelets compared to the features of the raw images. However, in this case there is a large improvement in the number of epochs

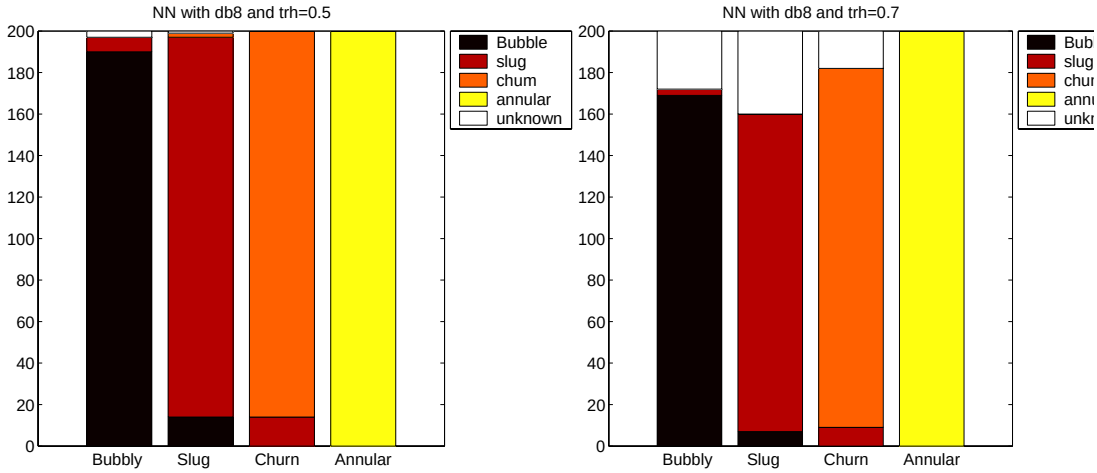

Fig. 42. *Result of the classification of the neutron radiographic two-phase flow images using input data pre-processed with the db8 wavelet, with a threshold of 0.5 to the left and 0.7 to the right.*

(iterations) used when training the ANN. When using the wavelet pre-processed data, the number of epochs is reduced by a factor of 100, compared to the raw data input (Fig. 43). With the raw data, the number of epochs always exceeds the maximum number of 30 000, before reaching the *MSE* target values of 10^{-3}. The classification efficiency is also slightly better in this case, compared to the neutron radiographic case. This is presumably also attributed to the better quality of the images. For the wavelet pre-processed data one slug flow image was classified as bubbly and the rest was correctly classified. That is, 149/ 150=99.33% for wavelet pre-processing, whereas the success ratio of classification with the raw image inputs was 146/150=97.33%. The result was the same for all wavelets with a threshold of 0.7.

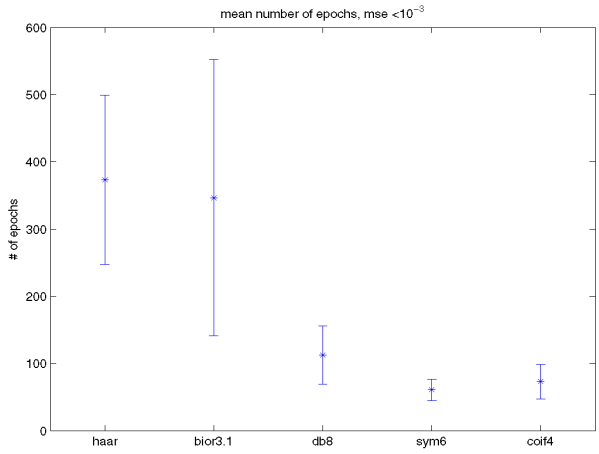

Fig. 43. *Depicted is the number of epochs used when training the network. The input data are wavelet pre-processed visible light images.*

Plans for the continuation

In stage 11 we plan to include the following parts in the current R&D program:

- A preliminary study for the development of core calculational methods for calculating higher eigenvalues and eigenfunctions;
- Development of the theory of neutron fluctuations in a system varying randomly in time with the master equation approach;
- A pilot experiment in a moderator with a Cf-252 source in order to test the Feynman- or the Rossi-alpha method.

Acknowledgement

This project was supported by the Swedish Nuclear Power Inspectorate, contract No. 14.5-030917-200305001.

REFERENCES

[1] Pázsit, I., Garis, N. S., 1995. Forskningsprogram angående härddiagnostik med neutronbrusmetoder. Etapp 1. Slutrapport, SKI Rapport 95:14.

[2] Pázsit, I., Garis, N. S., Thomson, O., 1996. Forskningsprogram angående härddiagnostik med neutronbrusmetoder. Etapp 2. Slutrapport, SKI Rapport 96:50.

[3] Pázsit, I., Garis, N. S., Karlsson, J., Rácz, A., 1997. Forskningsprogram angående härddiagnostik med neutronbrusmetoder. Etapp 3. Slutrapport, SKI Rapport 97:31.

[4] Pázsit, I., Karlsson, J. K-H., 1998. Research and Development Program in Reactor Diagnostics and Monitoring with Neutron Noise Methods. Stage 4. Final Report, SKI Report 98:25.

[5] Pázsit, I., Karlsson, J. K-H., Lindén, P., Arjanov, V., 1999. Research and Development Program in Reactor Diagnostics and Monitoring with Neutron Noise Methods. Stage 5. Final Report, SKI Report 99:33.

[6] Pázsit, I., Demazière, C., Avdic, S., Dahl, B., 2000. Research and Development Program in Reactor Diagnostics and Monitoring with Neutron Noise Methods. Stage 6. Final Report, SKI Report 00:28.

[7] Pázsit, I., Demazière, C., Arzhanov, V., Garis, N. S., 2001. Research and Development Program in Reactor Diagnostics and Monitoring with Neutron Noise Methods. Stage 7. Final Report, SKI Report 01:27.

[8] Pázsit, I., Demazière, C., Arzhanov, V., 2003. Research and Development Program in Reactor Diagnostics and Monitoring with Neutron Noise Methods. Stage 8. Final Report, SKI Report 2003:08.

[9] Pázsit, I., Arzhanov, V., Nordlund, A., Olsson, D., 2004. Research and Development Program in Reactor Diagnostics and Monitoring with Neutron Noise Methods. Stage 9. Final Report, SKI Report 2003:30.

[10] Thie, J.A., 1963. Reactor noise. Rowman and Littlefield, Inc., New York.

[11] Thie, J.A., 1981. Power reactor noise. American Nuclear Society, La Grange Park, Ill.

[12] Uhrig, R.E., 1970. Random noise techniques in nuclear reactor systems. The Ronald

Press Company, New York.

[13] Williams, M.M.R., 1974. Random processes in nuclear reactors. Pergamon Press, Oxford.

[14] Analytis, G. Th., Hennig, D., Karlsson, J. K. -H., 2001. The physical mechanism of core-wide and local instabilities at the Forsmark-1 BWR, Nuclear Engineering and Design 205, (1-2), 91-105.

[15] Lansåker, P., 1997. Forsmark internal report FT-Rapport 97/485 (in Swedish).

[16] Andersson, T., 2004. Personal communication, Ringhals AB.

[17] Glöckler, O., Pázsit, I., 1987. Spatial noise-source reconstruction. Annals of Nuclear Energy 14 (2), 63-75.

[18] Demazière, C., 2004. Development of a 2-D 2-group neutron noise simulator. Annals of Nuclear Energy 31 (6), 647-680.

[19] Demazière, C., Pázsit, I., 2001. 2-D 2-group neutron noise simulator and its application to anomaly localisation. Proceedings of the International Meeting on Mathematical Methods for Nuclear Applications (M&C2001), Salt Lake City, Utah, USA, September 9-13, 2001, American Nuclear Society.

[20] Demazière, C., Pázsit, I., 2003. A phenomenological model for the explanation of a strongly space-dependent decay ratio. Proceedings of the International Meeting on Nuclear Mathematical and Computational Sciences (M&C2003), Gatlinburg, Tennessee, USA, April 6-11, 2003, American Nuclear Society.

[21] Covington, L.J., 1995. SIMULATE-3: Advanced three-dimensional two-group reactor analysis code – user's manual. Studsvik/SOA-95/15.

[22] Nakamura, S., 1977. Computational methods in engineering and science with applications to fluid dynamics and nuclear systems. Wiley Interscience, New York.

[23] Bell, G.I., Glasstone, S., 1970. Nuclear reactor theory. Van Nostrand Reinhold Company, New York.

[24] Pázsit, I., Glöckler, O., 1983. On the neutron noise diagnostics of pressurized water reactor control rod vibrations. I. Periodic vibrations. Nuclear Science and Engineering 85 (2), 167-177.

[25] Pázsit, I., 1992. Dynamic transfer function calculations for core diagnostics. Annals of Nuclear Energy 19 (5), 303-312.

[26] Bussac, J., Reuss, P., 1985. Traité de neutronique. Hermann, Paris (in French).

[27] Wach, D., Kosály, G., 1974. Investigation of the joint effect of local and global driving sources in incore-neutron noise measurements. Atomkernenergie 23 (4), 244-250.

[28] Behringer, K., Kosály, G., Kostic, Lj., 1977. Theoretical investigation of the local and global components of the neutron-noise field in a boiling water reactor. Nuclear Science and Engineering 63 (3), 306-318.

[29] Antonopoulos-Domis, M., Skarpeta, K., 1986. Decomposition of neutron noise in a heterogeneous reactor model into a local and a global component. Atomkernenergie Kerntechnik 48 (4), 221-223.

[30] Sweeney, F.J., Robinson, J.C., 1980. Relative importance of attenuation and reactivity effects in explaining local and global BWR neutron noise. Transactions of the American Nuclear Society 34, 802.

[31] Sandwell, D.T., 1987. Biharmonic spline interpolation of GEOS-3 and SEASAT altimeter data, Geophysical Research Letters 2, 139-142.

[32] Karlsson, J. K-H., Pázsit, I., 1999. Localisation of a channel instability in the Forsmark-1 boiling water reactor. Annals of Nuclear Energy 26 (13), 1183-1204.

[33] Demazière, C., 2002. Development of a noise-based method for the determination of the Moderator Temperature Coefficient of reactivity (MTC) in Pressurized Water Reactors (PWRs). PhD thesis, CTH-RF-166, ISBN 91-7291-224-3, Chalmers University of Technology.

[34] Billebaud, A., Brissot, R., Heuer, D., Kerveno, M., Lebrun, C., Liatard, E., Loiseaux, J.M., Méplan, B.O., Merle, E., Perdu, F., Vollaire, J., 2002. The Muse-4 experiment - Prompt reactivity and neutron spectrum measurements. Proceedings of PHYSOR 2002 - International Conference on the New Frontiers of Nuclear Technology: Reactor Physics, Safety and High-Performance Computing. Seoul, Korea, October 7 - 10, 2002.

[35] Pázsit, I., Kuang, Z.F., 2001. Reactivity Monitoring in ADS with Neutron Fluctuation Analysis. Proceedings Embedded technical meeting AccApp at the Winter meeting of the American Nuclear Society, Reno, Nevada, 10 - 15 November 2001.

[36] Pázsit, I., 2001. Neutron fluctuations in traditional and accelerator driven reactors. Fluctuation and Noise Letters, 1, R101-R118.

[37] Ceder, M., Pázsit, I., 2003. Analytical solution for the Feynman-alpha formula for ADS with pulsed neutron sources. Progress of Nuclear Energy 43, 429 - 436.

[38] Pázsit, I., Ceder, M., Kuang, Z., 2004. Theory and analysis of the Feynman-alpha method for deterministically and randomly pulsed neutron sources. Nuclear Science and Engineering 148, 67-78.

[39] Wright, J., Pázsit, I., 2004. Derivation and analysis of the Feynman-alpha formula for deterministically pulsed sources. CTH-RF-179, Chalmers University of Technology.

[40] Pazsit, I., Kitamura, M., 1997. The Role of Nuclear Networks in Reactor Diagnostics and Control. Advances in Nuclear Science and Technology 24, 95-130.

[41] Hazarika, N., Chen, J.Z., Tsoi, A.C., Sergejew, A, 1997. Classification of EEG signals using the wavelet transform. Signal Processing 59, 61-72.

[42] Fadhel, E.A., Bhattacharyya, P., 1999. Application of a Steerable Wavelet Transform using Neural Network for Signature Verification. Pattern Analysis & Applications 2, 184-195.

[43] Verma, M.S., Pratt, L., Ganesh, C., Medina, C, 2002. Hair-MAP: a prototype automated system for forensic hair comparison and analysis. Forensic Science International 129, 168-186.

[44] Kandaswamy, A., Sathish Kumar, C., Ramanathan, R.P., Jayaraman, S., Malmurugan, N., 2003. Neural Classification of Lung Sounds using wavelet coefficients. Computers in Biology and Medicine, In Press, Corrected Proof, (Available online 4 September 2003).

[45] Addison, P.S., 2002. The Illustrated Wavelet Transform Handbook. Institute of Physics Publishing, Bristol and Philadelphia, ISBN 0-7503-0692-0.

[46] Bergh, J., Ekstedt, F., Lindberg, M., 1999. Wavelets. Studentlitteratur, Lund, Sweden, ISBN 91-44-00938-0.

[47] Mallat, S., 1999. A wavelet tour of signal processing. Academic Press, USA, ISBN 0-12-466606-X.

[48] The Math Works Inc., 2000. Users manual MatLab.

www.ski.se

STATENS KÄRNKRAFTINSPEKTION
Swedish Nuclear Power Inspectorate

POST/POSTAL ADDRESS SE-106 58 Stockholm
BESÖK/OFFICE Klarabergsviadukten 90
TELEFON/TELEPHONE +46 (0)8 698 84 00
TELEFAX +46 (0)8 661 90 86
E-POST/E-MAIL ski@ski.se
WEBBPLATS/WEB SITE www.ski.se